MODELING AND ANALYSIS OF LONGITUDINAL MULTIMODAL MAGNETIC RESONANCE IMAGING: APPLICATION TO EARLY BRAIN DEVELOPMENT

by

Neda Sadeghi

A dissertation submitted to the faculty of
The University of Utah
in partial fulfillment of the requirements for the degree of

Doctor of Philosophy

Department of Bioengineering

The University of Utah

December 2013

The University of Utah Graduate School

STATEMENT OF DISSERTATION APPROVAL

The dissertation of **Neda Sadeghi**

has been approved by the following supervisory committee members:

Guido Gerig	, Chair	**08/22/2013** Date Approved
P. Thomas Fletcher	, Member	**08/22/2013** Date Approved
Edward Hsu	, Member	**08/22/2013** Date Approved
Rob S. MacLeod	, Member	**08/22/2013** Date Approved
Sarang Joshi	, Member	**08/22/2013** Date Approved

and by **Patrick A. Tresco**, Chair/Dean of

the Department/College/School of **Bioengineering**

and by David B. Kieda, Dean of The Graduate School.

ABSTRACT

Many mental illnesses are thought to have their origins in early stages of development, encouraging increased research efforts related to early neurodevelopment. Magnetic resonance imaging (MRI) has provided us with an unprecedented view of the brain in vivo. More recently, diffusion tensor imaging (DTI/DT-MRI), a magnetic resonance imaging technique, has enabled the characterization of the microstrucutral organization of tissue in vivo. As the brain develops, the water content in the brain decreases while protein and fat content increases due to processes such as myelination and axonal organization. Changes of signal intensity in structural MRI and diffusion parameters of DTI reflect these underlying biological changes.

Longitudinal neuroimaging studies provide a unique opportunity for understanding brain maturation by taking repeated scans over a time course within individuals. Despite the availability of detailed images of the brain, there has been little progress in accurate modeling of brain development or creating predictive models of structure that could help identify early signs of illness. We have developed methodologies for the nonlinear parametric modeling of longitudinal structural MRI and DTI changes over the neurodevelopmental period to address this gap. This research provides a normative model of early brain growth trajectory as is represented in structural MRI and DTI data, which will be crucial to understanding the timing and potential mechanisms of atypical development. Growth trajectories are described via intuitive parameters related to delay, rate of growth, and expected asymptotic values, all descriptive measures that can answer clinical questions related to quantitative analysis of growth patterns. We demonstrate the potential of the framework on two clinical studies: healthy controls (singletons and twins) and children at risk of autism. Our framework is designed not only to provide qualitative comparisons, but also to give researchers and clinicians quantitative parameters and a statistical testing scheme. Moreover, the method includes modeling of growth trajectories of individuals, resulting in personalized profiles. The statistical framework also allows for prediction and prediction intervals for subject-specific growth trajectories, which will be crucial for efforts to improve diagnosis for individuals and personalized treatment.

To my dear parents Nahid and Ali, my loveling husband Ron, and my wonderful brothers Hossein and Hamed.

CONTENTS

LIST OF TABLES

ACKNOWLEDGMENTS

First and foremost I would like to thank my adviser, Guido Gerig, for his encouragement and support throughout my graduate studies. He has taught me to look at what works and be positive when I felt nothing was working. He gave me the freedom to pick my research topic but was there to guide me. I would also like to thank the other members of my committee: Sarang Joshi, P. Thomas Fletcher, Edward Hsu, and Rob MacLeod. Special thanks to P. Thomas Fletcher, who helped me with many statistical questions, and Rob MacLeod for reminding me of the importance of communication and good scientific presentation and writing. Edward Hsu encouraged me to do more rigorous validation, and Sarang Joshi provided the mathematical foundation of imaging. I especially thank Marcel Prastawa for his continued support during my research and his expertise, which contributed greatly to the development of ideas presented in this dissertation.

I would also like to thank the Department of Bioengineering and the Scientific Computing and Imaging Institute for providing an enjoyable working environment. A special thanks to Sylvain Gouttard and Clement Vachet, who helped enormously with many projects and helpful discussions. I thank Nathan Galli for many last-minute poster preparations and interesting conversations. I would also like to thank students in the third and fourth floor lab for making work enjoyable; somehow solutions to problems seemed easier after a foosball or a ping-pong game. I will surely miss that.

I thank my parents, Ali and Nahid, and my brothers, Hamed and Hossein, for their love and support throughout my life, for always believing in me, and encouraging me to pursue my dream.

Finally, I thank my husband, Ron, for his patience, love, and support, especially during deadlines when the task at hand seemed impossible.

I have had a wonderful journey as a graduate student, and I am looking forward to the next chapter of my life.

CHAPTER 1

INTRODUCTION

1.1 Motivation

Mental illnesses such as depression, schizophrenia, and autism are widespread and often require life-long health care support. Many of these illnesses are thought to have their origins in early stages of development, encouraging increased research efforts related to early neurodevelopment. Both structural (sMRI) and diffusion tensor magnetic resonance imaging (DT-MRI/DTI) have provided an unprecedented and noninvasive view of the brain in vivo.

Magnetic resonance imaging (MRI) is well suited for pediatric studies since it does not use ionizing radiation and enables safe longitudinal scans of children noninvasively. The brain undergoes significant changes during the first 2 years of life, with continued growth into adulthood. Previous cross-sectional neuroimaging studies have indicated an overall brain size increase during this period, reaching 80–90% of adult volume by age 2 [1]. More recently, Knickmeyer *et al.* found that total brain volume increases by 101% in the first year, followed by 15% in the second year [2]. In addition to morphometric measures such as volume [2, 3, 4] and shape (i.e., cortical folding) [5], signal characteristics of brain tissue also change, reflecting the maturation of the underlying tissue. During the first 6 months after birth, the signal intensities of gray and white matter in T1-weighted (T1W) and T2-weighted (T2W) images are the reverse of those seen in adults. This is mainly due to myelination, as white matter is mostly unmyelinated at birth. As white matter myelinates, signal intensity changes from hypointense to hyperintense relative to gray matter in T1W images. The reverse pattern is seen in T2W (from hyperintense to hypointense), as shown in Fig. 1.1.

Myelination follows a spatiotemporal sequence as described by histological studies [6] and qualitatively by radiologists [7]. However, quantitative assessment of the maturation pattern of white matter is still lacking. Development of cognitive functions is associated with white matter maturation, and hence abnormalities in integrity of white matter can cause

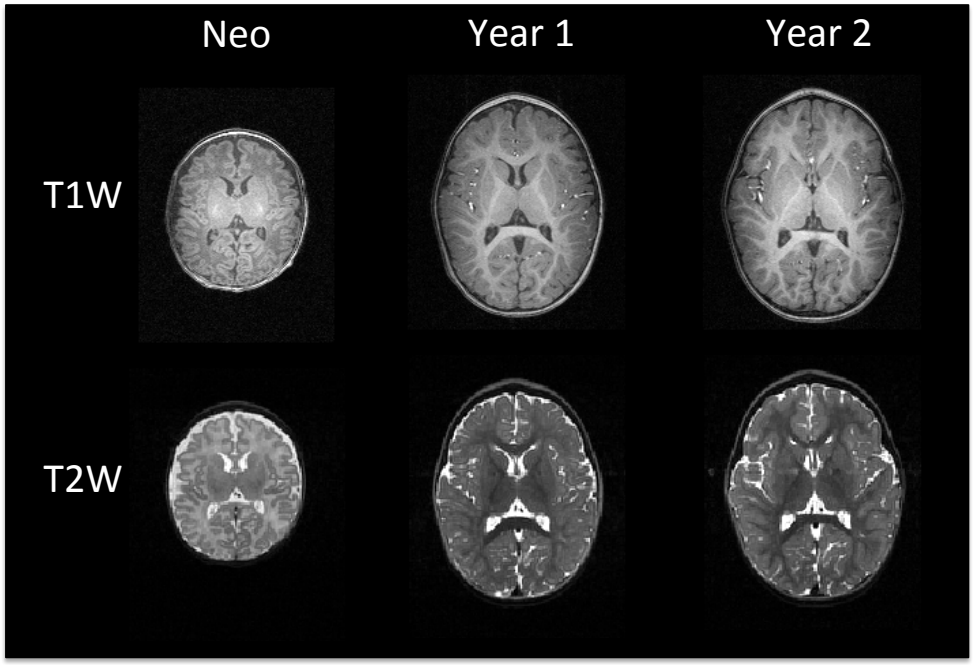

Figure 1.1: T1W and T2W images of an individual scanned at about 2 weeks, 1 year, and 2 years. The pattern of contrast at birth is the reverse of what is seen at 2 years.

cognitive deficits. In many neurodevelopment disorders such as autism spectrum disorders, there are reported abnormalities in white matter fiber tract integrity [8]. However, the extent and the developmental differences remain unclear.

Diffusion tensor imaging (DTI) provides additional information about the microstructure of the brain. This method measures the average displacement of water molecules within tissue during a fixed time. There is more diffusion where molecules can travel freely and less diffusion where movement is impeded by obstacles such as cell membranes, myelin, and macromolecules. Because the diffusion of water molecules is shaped by the underlying tissue structure, it is possible to gain an understanding of the underlying tissue structure by measuring diffusion. Fiber bundle organization can be depicted in DTI as water diffuses more parallel to the fiber direction. This anisotropic diffusion provides detailed information about brain axonal organization. As the white matter matures, the diffusion of water in the brain becomes more restricted. Monitoring changes of diffusion parameters provides information about the maturation pattern of white matter.

In diffusion tensor imaging, 3D motion of water molecules is modeled via a second order tensor at each voxel [9]. A tensor is represented as a diffusion matrix and can be visualized as an ellipsoid where the length of each primary axis represents the average diffusion in each spatial direction [10]. The tensor information can be summarized into simpler invariant

quantitative measures (independent of the orientation of the reference frame) related to the size or shape of the tensor. For example, one of the most common measurements, fractional anisotropy (FA), is an index from 0 (isotropic) to 1 (anisotropic), indicating the shape of the tensor ranging from a sphere to a thin stick [11]. Another measurement is mean diffusivity, which can be explained as the average length of axes of the ellipsoid indicating the size of the tensor. This measure has proved useful for assessing the diffusion drop in brain ischemia [12]. More recently, axial diffusivity (AD) and radial diffusivity (RD) have been used to help to better understand the changes of the diffusion tensor [13, 14]. AD is the length of the longest axes of ellipsoid, and RD is the average of the two shorter axes. Analysis of DTI data of pediatric subjects has illustrated changes of these indices due to development [15]. Casicio *et al.* found overall increases in fractional anisotropy during development and reduced overall diffusion due to development [16].

FA values can also be color-coded by using the direction of the main axes of the ellipsoid. Red is used to indicate the left-right direction, blue for superior-inferior, and green for anterior-posterior directions [17]. Using colored FA images, most of the projection, association, and commissural fibers can be identified in these images. Projection fibers connect the cortex to the interior parts of the brain and to the spinal cord (blue color), association fibers connect different parts of the same cerebral hemisphere (green color), and commissural fibers connect the left and right hemispheres (red color). Fig. 1.2 shows colored FA images of one subject at 2 weeks, 1 year, and 2 years. The brightness is weighted by the fractional anisotropy [17].

Studying early brain development (the age group of neonates up to 2 years) via structural and diffusion MRI involves two major challenges: successful MRI scanning of nonsedated infants and an image analysis methodology designed to cope with rapidly changing contrast, size, and shape of anatomical structures and spatiotemporal variations to describe the trajectory of early growth.

This dissertation focuses on the second challenge by systematically mapping a population of images onto a common template, extracting intensity values of MRI data and diffusion parameters of DTI for regions of interest, and performing statistical analysis on these sets of measurements. The longitudinal nature of the data presents unique challenges for the statistical analysis that we address in this work. Previous approaches to modeling of early brain development have mainly relied on cross-sectional data or have used linear models to describe changes in these measurements. Growth is highly nonlinear at this stage and linear models are suboptimal for describing early brain development. In addition to analysis of

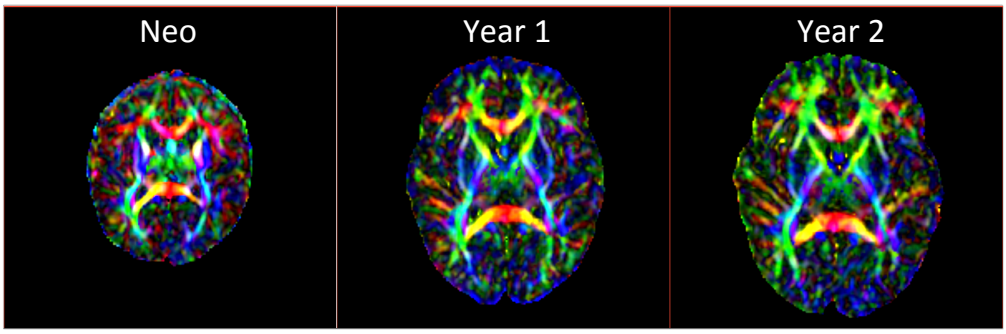

Figure 1.2: Colored FA images of an individual. Left to right: scans at 2 weeks, 1 year, and 2 years.

population studies and drawing inferences based on the average growth trajectories, we also focus on modeling individual trajectories to enable personalized treatment. Understanding how an individual's growth trajectory differs from the normative model could help clinicians to develop an individualized treatment plan, taking into account not only the normative model, but also an individual's trajectory.

We will address challenges that are unique to a longitudinal study design by appropriately modeling the growth at this stage and taking into account the correlation among individual scans. It is important to note that for a true longitudinal modeling, we need both longitudinal data and longitudinal analysis.

1.2 Longitudinal Studies

1.2.1 Objective of Longitudinal Studies

The defining feature of longitudinal studies is that subjects are measured repeatedly over the course of the study. This is in contrast to cross-sectional studies in which an individual is measured at only a single time point. Longitudinal studies enable assessment of within-individual changes in the response variable, and thereby have the capacity to separate between cohort and age effects. This is displayed in Fig. 1.3, where the plot on the left shows the response variable decreases with age. However, if considering that the data are longitudinal (the right plot of Fig. 1.3), it is evident that all responses increase with time. This example illustrates that the longitudinal studies can separate between age effects (all of an individual's responses increasing with time) versus cohort effect (differences at baseline). Nowhere is this more important than in health sciences, where heterogeneity of individuals due to genetic and environmental factors plays an important role in the progression of the disease or the response of individuals to treatment. The aim of the longitudinal study is to characterize within-individual changes over time and to determine

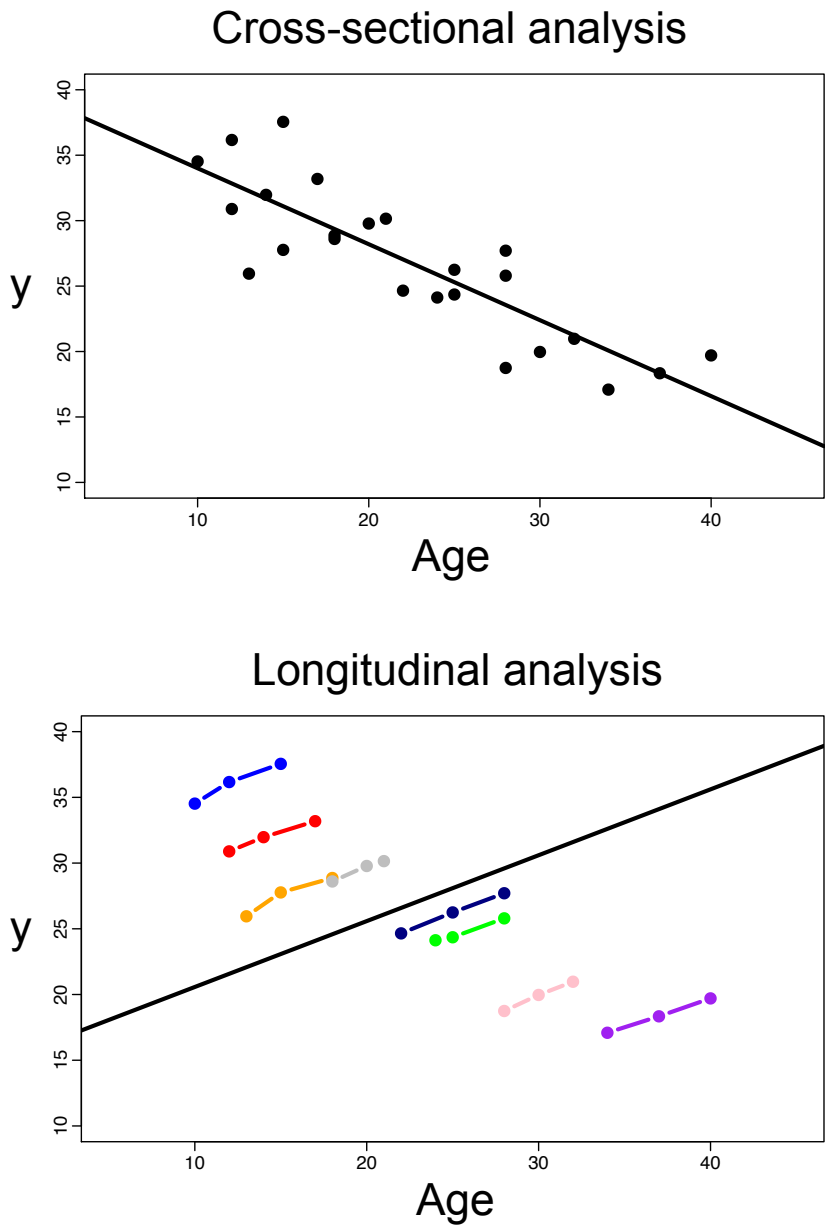

Figure 1.3: The relationship of response variable y with age as a function of time. Top: Cross-sectional analysis shows a decreasing trend between response variable y and age. Bottom: A different pattern emerges when considering the within-individual trend.

whether within-individual changes in the response are associated with some covariates such as treatment plan, clinical group, or biological factors.

1.2.2 Properties of Longitudinal Studies

1.2.2.1 Correlated Data

The hallmark characteristic of longitudinal data is the correlation among repeated measurements. As these measurements are obtained on the same individual, there is a correlation among the measurements, with measurements obtained closer in time being more correlated than the ones further apart. This correlation among repeated measurements breaks down the fundamental independence assumption of most statistical regression techniques [18].

1.2.2.2 Unbalanced Data: Uneven Spacing, Missing Time Points

Most longitudinal studies plan to obtain the same number of measurements for each individual at the same time; however, in practice this is rarely the case. With studies that span over some period of time, it is inevitable that some individuals will drop out of the studies and some might miss their appointments and reschedule for a later time. In longitudinal neuroimaging of infants, this is even more significant, as some images might have to be excluded from study due to motion of the subject or insufficient quality. Fig. 1.4 illustrates an example of longitudinal data.

1.2.2.3 Multivariate Features

In longitudinal studies, as in cross-sectional studies, multiple measurements on an individual can be obtained at any given time. The correlation among these features should be taken into account. In neuroimaing studies, multiple MRI scans can be obtained on an individual during a session. As the underlying biology is the same, there is a correlation among the scans of the individual that should be considered.

1.2.3 Clinical Applications

Longitudinal neuroimaging studies have gained popularity in recent years due to advances in medical imaging. These studies allow us to track developmental changes or progression of a disease in vivo longitudinally with more accuracy compared to cross-sectional studies. In this work, we have concentrated on the diffusion and apparent signal intensity changes of MRI. However, the methodologies developed here have also been successfully

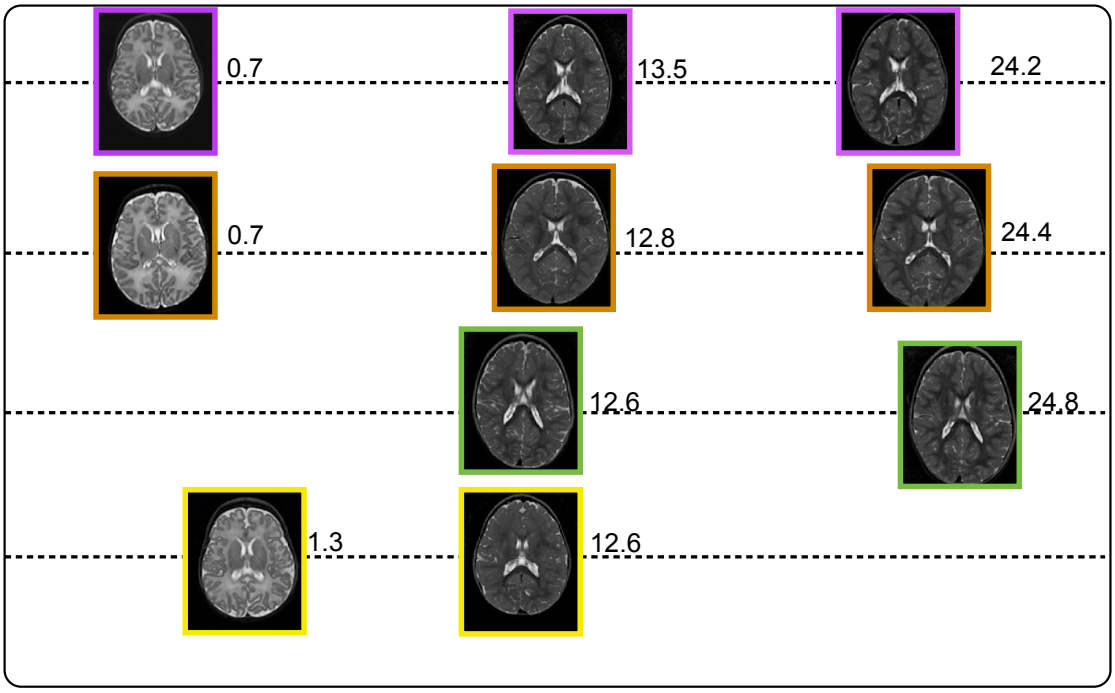

Figure 1.4: T1W longitudinal data of multiple subjects. Each subject is represented by a different color. The number next to each scan indicates the age (in months) of the infant at the time of the scan. Uneven spacing, missing time points, and correlation among repeated scans are common properties of longitudinal data.

applied to volume changes of white and gray matter over time for subjects at risk of autism, and also DTI and volume changes of adolescent subjects with Down syndrome.

1.2.3.1 Population Analysis

Understanding early brain development has great scientific and clinical importance. The human brain undergoes rapid organization and structuring early in life, and also there is great heterogeneity among different individuals. Longitudinal modeling of longitudinal data yields a more accurate average trajectory over time without the confounding cohort effects [18, 19]. This is of great importance when the development itself is in question. Recently, longitudinal data have become available for this critical period. However, normative models are still not available to describe a normal pattern of development as is shown in structural and diffusion MRI.

By undertaking appropriate longitudinal statistical analysis, we can model the average trajectory via a parametric function, where we can summarize growth with a few parameters. This analysis also enables comparison of a normative population model to other groups. For example, we can model population changes of subjects who have been diagnosed

with a specific disease and compare this growth curve to the normative model to gain a better understanding of the pathology and when deviation occurs. We can also gain a better understanding of the spatiotemporal sequence of maturation of white matter in the developing brain.

Once average trajectories are obtained for different groups, we can make inferences about parameters of the regression. In this dissertation, we consider studying longitudinal changes of intensity of T1W and T2W MRI and diffusion parameters of DTI for a group of subjects from 2 weeks to 2 years old to establish a normative pattern of development along with its variability. The Gompertz function is utilized to characterize these changes over time as it uses intuitive parameters describing growth: asymptote, delay, and speed. White matter regions that are known to mature at different rates are analyzed and quantified. The second application is studying infants at high risk of autism, by virtue of having a sibling who has been diagnosed with autism. In this study, the average trajectories of high risk individuals who eventually did get diagnosed with autism are compared to those who were spared by the disease, shedding light on how developmental trajectories differ between the two groups. Last, but not least, we applied the methodology to estimate developmental trajectories for twins and singletons and compare these trajectories between the two groups. We hypothesized that there might be group differences between developmental trajectories of twins and singletons due to suboptimal pre- and postnatal environments.

1.2.3.2 Subject Analysis

One of the important aspects of longitudinal analysis is the direct measurement of intraindividual changes over time. Even if all the observations for all the time points are not available for a subject, by pooling the data from other subjects in the study along with the available observations for the individual, prediction of an individual trajectory is possible. The estimation of personalized growth profiles is of great clinical interest as individuals respond differently to treatment and show different growth trajectories. Also, in cases when only a single scan is available, the intensity or diffusion parameters of the subject can be compared to the normative model to indicate whether an individual is within the normative range of variability. Additionally, subject-specific growth trajectory and predictive intervals can be predicted based on only one scan. Such predictions might improve early detection and outcome.

1.2.4 Traditional Approaches

There are two commonly used approaches for longitudinal data analysis: repeated measures analysis of variance (repeated ANOVA) and methods based on summary measures. Repeated ANOVA analysis focuses on the change of the mean response, with limited information about individual changes over time. Individuals are assumed to have additional individual effect (random effect) that is constant over time. This effect is assumed to be the same for all the measurements on an individual, resulting in the variances and covariances of all the individual's time points being the same. However, this is not appropriate for longitudinal data as correlations among repeated measures tend to decrease with increasing time [18].

ANOVA was developed for analysis of balanced data where the measurements for all the subjects are obtained at the same time; however, as we noted earlier, this is hardly the case for longitudinal data where missing time points and uneven spacing between measurements are common. Also, in repeated ANOVA, covariates are assumed to be discrete values, so we can obtain changes only between mean responses rather than a continuous trajectory of mean response.

Another common approach is to use summary measures, first by fitting some model at the individual level to obtain summary measures (i.e., slope of the regression lines, area under the curve) and then using standard parametric or nonparameteric methods to analyze the summary measures. This approach can raise issues when the data are unbalanced and there are missing time points. For example, if the measurements are taken at different time points, the resulting summary measure might have different variances. Also, different individuals might have the same summary measure, but the shape of their growth trajectory could be quite different. For example, if one considers the area under the curve as the summary measure, curves with different shapes can still result in the same summary measure. Also, subjects with only one time point would need to be excluded from the analysis [18].

We need a statistical method that can handle uneven spacing between measurements and missing time points, as this is the reality of longitudinal data. In Chapter 2, we discuss mixed effect models, a class of statistical methods that model the correlation of measurements of an individual along with modeling the mean response of a population over time. These methods are powerful; however, a review of the literature indicates they are not commonly used in the medical imaging community. This might be due to a lack of familiarity, the complexity of the method, and a lack of tools for these types of analysis.

In this dissertation, we provide the background of these models, show their utility applied to multiple ongoing longitudinal early brain development studies, and provide extensions to the modeling to include multivariate modeling of MRI data. Additionally, we provide subject-specific growth trajectories with predictive intervals based on a limited number of scans. The subject-specific prediction interval yields a more precise interval that is specific to an individual. The forecasting method proposed in this dissertation has the potential to improve early recognition of abnormalities.

1.3 Contributions

This dissertation describes the following contributions in image analysis and early brain development:

1. An analysis of quantitative regional characterization of intensity changes of structural MRI and diffusion parameters of DTI in healthy developing infants highlights the heterogenous spatiotemporal pattern of white matter maturation.

2. A nonlinear longitudinal modeling of early brain development via the Gompertz function is proposed. The Gompertz growth function uses intuitive parameters related to delay, rate of change, and expected asymptotic value. These parameters are descriptive measures that can answer clinical questions related to quantitative analysis and comparison of growth patterns.

3. Normative models for diffusion parameters are constructed. These models can serve as a normal standard of reference for evaluating pediatric neurological abnormalities.

4. Nonlinear longitudinal modeling is applied to longitudinal data of children at risk of autism to understand the different patterns of maturation that emerge between high risk children who do get diagnosed with autism versus those who do not.

5. The methodologies developed in this dissertation have been been applied to longitudinal data of singletons and twins to evaluate whether there is a difference in the developmental trajectories of these two groups.

6. Taking advantage of the mean response of changes over time along with the estimated variance and covariance structure between and within subjects, individual longitudinal trajectories are estimated.

7. Extension to nonlinear mixed effect modeling enables multimodal analysis of MRI data (T1W, T2W, DTI) to account for correlation among these multiple measurements.

8. Confidence and predictive intervals based on a Monte Carlo simulation are estimated for structural and diffusion growth trajectories. The predictive intervals can be used as abnormality detection.

9. Future growth characteristics (i.e., diffusion parameters) of new individuals with limited data are estimated. Subject-specific growth trajectories along with predictive intervals are estimated for the new individual.

1.4 Overview of Chapters

The remainder of this dissertation is organized as follows:

Chapter 2 discusses the framework that is necessary to optimally model longitudinal changes of brain structures. Multiple growth functions that are common in the literature or appropriate for this age group are compared and discussed.

In Chapter 3, the application of our framework to neurodevelopment is presented. Patterns of the development in different regions of white matter are characterized. Inferences are made in regard to regional differences and growth is described quantitatively in terms of asymptote, delay, and speed.

Chapter 4 presents the results and challenges of the autism study. Inferences on the Gompertz parameters of mean trajectories of groups diagnosed with autism and the group not diagnosed are made.

In Chapter 5, developmental trajectories of monozygotic and dizygotic twins are compared. Subsequently, the two groups are combined and their developmental trajectories are compared to singletons.

Chapter 6 provides an extension to univariate nonlinear mixed effects modeling by jointly estimating multimodal growth trajectories of structural and diffusion data.

Chapter 7 focuses on subject specific analysis, with the goal of obtaining individual trajectories for each subject in the study and also an estimate of the individual trajectories for new subjects by utilizing the normative model as prior knowledge.

Chapter 8 reviews contributions of this dissertation, discusses its limitations, and presents future work.

CHAPTER 2

FRAMEWORK FOR MODELING GROWTH TRAJECTORIES OF EARLY BRAIN DEVELOPMENT

2.1 Introduction

This chapter provides background on the choice of parametric growth functions and introduces mixed effects models. Growth curves provide a convenient way of modeling a large set of measurements with relatively few parameters. These curves characterize changes in mean responses over time and enable comparison of growth rates and prediction of future growth. In longitudinal data analysis, covariances among repeated measurements need to be properly modeled to yield valid inferences about the parameters of growth curves [18]. This is illustrated in Fig. 1.3 in which the group trend shows completely different results when considering correlation among individuals. In section 2.3, we introduce mixed effects models, which provide a powerful way to analyze longitudinal data. Mixed effects models overcome limitations of traditional approaches to repeated ANOVA and summary measures methods as these models do not require the same number of observations per individual nor do they require measurements to be taken at the exact time for all the individuals. In section 2.4, we review criteria used to select a growth curve parameterization for mixed-effects modeling of longitudinal structural and diffusion MRI data.

2.2 Growth Models

The simplest model and one that is used commonly in the literature is a linear model, where the relationship between response variable Y_i and independent variable X_i is formulated as

$$Y_i = \beta_0 + \beta_1 g_1(X_{i1}) + \cdots + \beta_p g_p(X_{ip}) + e_i \qquad i = 1, \cdots, n \tag{2.1}$$

where there are p explanatory variables $(X_1 \cdots X_p)$, e is the error term, and $g_1, \cdots, g_p$ may

be nonlinear functions. These models are called linear models as the expectation function is linear in its parameters, β. Explanatory variables X are treated as fixed values. Polynomial functions are an example of these models where degree of zero is simply a constant function, degree of one is a line, degree of two is a quadratic, and so on. With an increasing order of polynomials, one can obtain an increasingly accurate approximation to the observed data within the observed range. These growth curves are categorized as empirical models, which are based solely on the relationship between the response and the independent variable with no regard to the underlying mechanism producing the data. Nonlinear models, on the other hand, are often mechanistic, where the sole purpose is not to just fit the data, but rather to describe the mechanism that produces the response [20]. Even when the nonlinear models are derived empirically, characteristics of the data, such as asymptotes and monotonicity, are considered. These models are considered semimechanistic [20]. Nonlinear models generally use fewer parameters than their linear counterparts to describe the data, providing a more parsimonious description of the data. Also, nonlinear models provide better prediction outside of the range of observed data.

Mechanistic models of growth are generally based on a differential equation relating growth rate dy/dt to response variable y (i.e., size, diffusion parameter) [21]. This formulation has led to a variety of growth models, such as exponential, monomolecular, logistic, and Gompertz functions.

2.2.1 Exponential and Monomolecular

Exponential growth is based on the assumption that growth rate is proportional to size: $dy/dt = ry$. The solution to this differential equation is

$$y(t) = y_0 e^{rt} = \kappa e^{rt}. \tag{2.2}$$

Growth can be both increasing and decreasing. Exponential decay is formulated as $dy/dt = -ry$, where the solution is

$$y(t) = y_0 e^{-rt} = \kappa e^{-rt}. \tag{2.3}$$

Parameter y_0 is the initial size, diffusion parameter, or intensity value of MRI at age zero. Exponential decay could be a good model for diffusivity measures and T2W, as these values decline over time. However, exponential growth can be valid only for a very short period of time, which is not plausible for our datasets. Even though we are modeling development

only during the first 2 years of life, asymptotic properties are already observed during this age range. We can use two variants of exponential growth that have asymptotic properties.

$$y(t) = y_\infty(1 - e^{-rt}) = \alpha(1 - e^{rt}), \tag{2.4}$$

and

$$y(t) = y_\infty - (y_\infty - y_0)e^{-rt} = \alpha - (\alpha - \kappa)e^{rt}. \tag{2.5}$$

Notice, (2.4) is a special case of 2.5 when $y_0 = 0$. Equations 2.4 and 2.5 are examples of monomolecular growth models, where the growth rate is $dy/dt = r(y_\infty - y)$. These models are also referred to as asymptotic regression models and the von Bertalanffy curve [22].

2.2.2 Logistic

Logistic curves incorporate three stages of growth in the model: 1) initial growth where $dy/dt = ry$, 2) linear growth where $y = y_0 + rt$, and 3) limiting stage where the growth rate approaches zero and y approaches y_∞. Incorporating these three stages in the model results in the following differential equation $dy/dt = ry(y_\infty - y)/y_\infty$ [21]. The solution to this differential equation is the logistic curve:

$$y = \frac{y_\infty}{1 + e^{\eta - rt}} = \frac{\alpha}{1 + e^{\eta - rt}}. \tag{2.6}$$

The inflection point of the logistic curve is when $y = \alpha/2$, where the absolute growth rate is maximal, and the curve is symmetric around its inflection point. This symmetry is one of the drawbacks of the logistic curve. The Gompertz curve as described in the following section is more flexible by allowing the curve to be asymmetric around its inflection point [21].

2.2.3 Gompertz

The Gompertz growth curve is similar to the logistic growth curve where it incorporates the three stages of growth mentioned above. However, in the case of Gompertz, the growth rate decreases exponentially with time, resulting in the following differential equation $dy/dt = kye^{-rt}$ [21]. The solution to this differential equation is

$$y = y_\infty e^{-(k/r)e^{-rt}} = y_\infty e^{-d\, e^{-rt}} = \alpha e^{-d\, e^{-rt}}, \tag{2.7}$$

where α is the final asymptotic value, parameter r specifies the decay in the growth rate, and parameter d relates the final and initial values of y. The b parameter can be thought of as the delay parameter. For example, if two curves, f_1 and f_2, have the same final value y_∞, and the initial values of these curves y_0 are such that $y_{01} > y_{02}$, then $d_{f_1} < d_{f_2}$.

2.2.4 Selection of Growth Models

Fig. 2.1 shows exponential, monomolecular, logistic, and Gompertz growth models. The curves most commonly used in studying human growth and development in regards to size, length, and mass are the Gompertz or logistic or a variation of these models [21]. However, a review of the literature on models of structural and diffusion changes of brain MRI reveals that mainly polynomial models, such as linear and quadratic, have been utilized. This is partially due to the ease of use of polynomials. They are relatively easy to fit, and statistical distribution properties of the parameters are easier to obtain [21]. However, polynomials cannot easily represent the asymptotic behavior of growth that is observed in early brain development. We prefer mechanistic or semimechanistic models of growth, as we are interested in understanding early brain development and polynomials do not represent biological mechanisms of growth. Among these mechanistic models, the Gompertz function provides the most flexibility and favors faster early growth, which is what we observe in the early years of life. The Gompertz function when compared to the logistic function has a faster initial growth and slower approach to the asymptote [21]. The parameters of the Gompertz function also provide intuitive parameterization of growth in terms of asymptotic value α, delay d, and growth rate r. In section 2.4, we will systematically evaluate all these functions applied to structural and diffusion MRI data of early brain development.

2.3 Mixed Effects Model

In longitudinal studies, response variables are measured repeatedly on the same individual, enabling direct study of change. Often, we cannot control the exact timing of when these measurements are taken. Therefore, individuals might have a different number of observations and variability among the timing of observations. Also, longitudinal data analysis requires a special type of statistical analysis to account for the intercorrelation among observations on each subject. This correlation needs to be considered to draw valid scientific inferences [19]. Mixed effects models provide a powerful and flexible environment for analyzing longitudinal data. In the mixed effects model, the observed data are assumed to be a combination of both *fixed effects*, β, parameters associated with the entire population (or at least within a subpopulation), and *random effects*, b, that are specific to an individual drawn at random from the population. Random effects account for the heterogeneity that is present in the population as these effects vary among subjects. An individual will have its own subject-specific mean trajectory; thus, repeated measures of an individual subject have common random effects, and thereby correlation among an individual's measurements

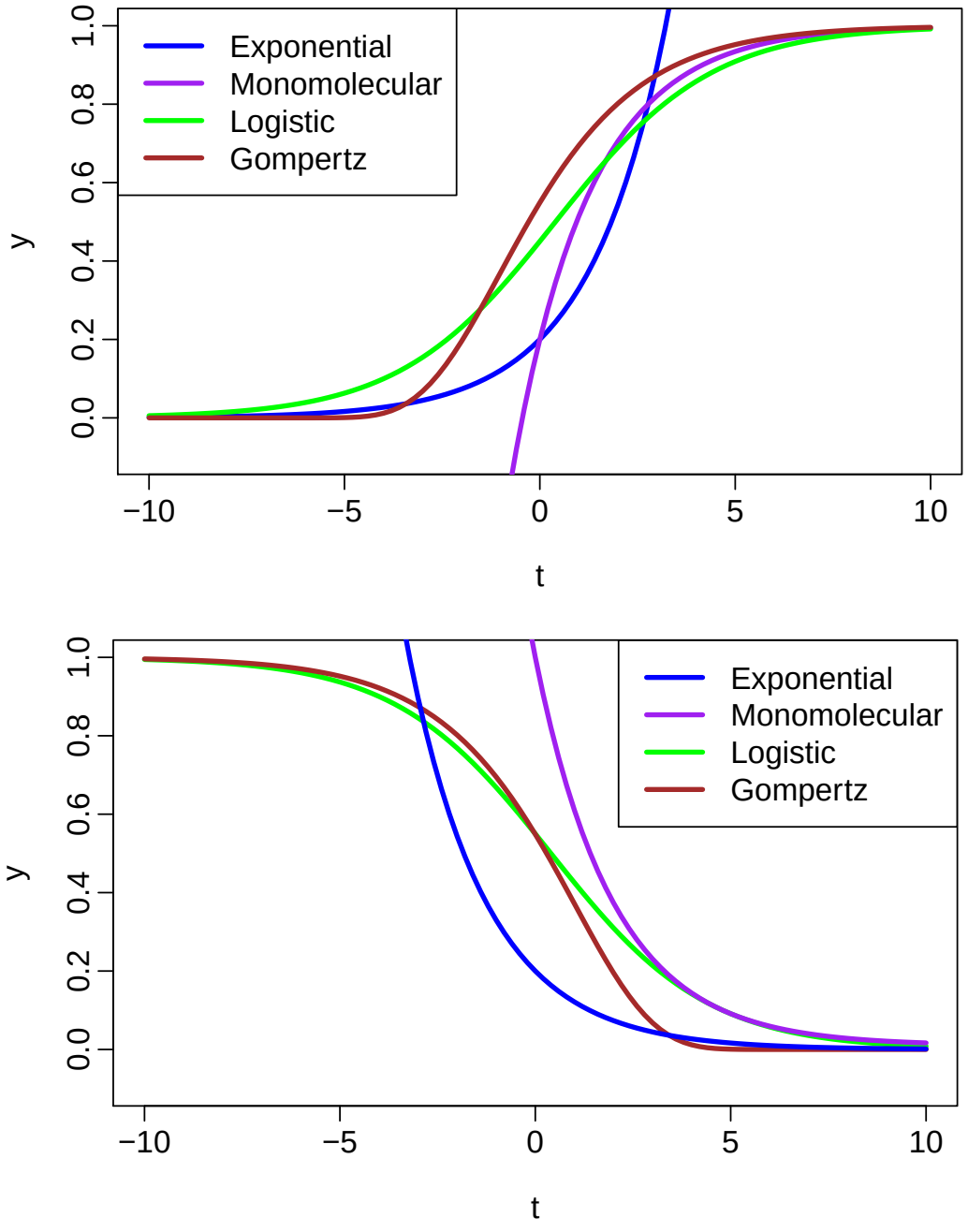

Figure 2.1: Increasing and decreasing growth models.

is taken into account. A mixed effects model distinguishes between a within-subject source of variability and a between-subject source of variability.

2.3.1 Linear Mixed Effects Model

Linear mixed effects models are mixed effect models where both the fixed and random effects enter the model linearly. In these models, the individual trend is a linear model built upon the overall population trend, which is also linear. Linear mixed effects models can be formulated as:

$$y_i = X_i\beta + Z_i b_i + e_i \qquad i = 1, \cdots, M, \tag{2.8}$$

where y_i is the $n_i \times 1$ vector of measurements for subject i. β is a $p \times 1$ vector of fixed effects and b_i is the $q \times 1$ vector of random effects. X_i and Z_i are design matrices that relate fixed effects and random effects to y_i. X_i is the $n_i \times p$ matrix, which can include variables such as clinical group, age, and gender. Z_i is the $n_i \times q$ matrix for the random effects and includes variables such as age. b_i is a multivariate gaussian with mean zero, $b_i \sim \mathcal{N}(0, \Psi)$, and e_i is the $n_i \times 1$ measurement error and is normally distributed $\mathcal{N}(0, \sigma^2)$. Random effects and measurement errors are assumed to be independent.

Let us consider the case where $X_i = Z_i$. In this case, each individual will have its own regression coefficients $\beta + b_i$ and thereby its own subject-specific mean trajectory:

$$E(y_i|b_i) = X_i\beta + Z_i b_i \tag{2.9}$$

and the mean response for the population is averaged over all the individuals in the population:

$$E(y_i) = X_i\beta. \tag{2.10}$$

The regression parameter β describes the mean response over time, while b_i explains an individual's deviation from the mean response. For example, if only the intercept is considered as a random effect, individual trajectories will vary only in intercept term. All the trajectories will have the same slope as the population model. However, if both intercept and slope are considered as random effects, each individual's trajectory will have a different intercept and slope. We can also distinguish the conditional covariance of $y_i|b_i$,

$$Cov(y_i|b_i) = Cov(e_i) = \sigma^2 I_{n_i}, \tag{2.11}$$

from the marginal covariance of y_i,

$$Cov(y_i) = Cov(Z_i b_i) + Cov(e_i) = Z_i \Psi Z_i^T + \sigma^2 I_{n_i}, \tag{2.12}$$

which is not a diagonal matrix, thereby accounting for correlation among observations of the same individual. Thus by including random effects, correlation among measurements of

y_i is modeled. Also, $Cov(y_i)$ is defined in terms of Ψ and σ^2, allowing for explicit analysis of between-subject, Ψ, and within-subject, σ^2, sources of variation. Because the covariance is a function of the times of measurements (time is usually modeled in Z_i), the mixed effects model is well suited when individuals have measurements at different times or have missing time points.

2.3.1.1 Parameter Estimation

The likelihood function for the linear mixed effect model of (2.8) is:

$$L(\beta, \Psi, \sigma^2|y) = \prod_{i=1}^{M} p(y_i|\beta, \Psi, \sigma^2). \tag{2.13}$$

Since nonobservable random effects are part of the model, we must integrate out random effects; thus, the marginal density of y_i is:

$$p(y_i|\beta, \Psi, \sigma^2) = \int p(y_i|\beta, b_i, \sigma^2)p(b_i|\Psi, \sigma^2)db_i. \tag{2.14}$$

The population growth parameters β and variance components Ψ and σ^2 are estimated by maximizing the likelihood equation of (2.14).

Equation 2.8 can be rewritten as $y_i = X_i\beta + e_i^*$, where $e_i^* = Z_i b_i + e_i$. In this formulation e^* is the sum of two independent multivariate normal random vectors with mean zero and covariance V_i, where $V_i = cov(Z_i b_i) + cov(e_i) = Z_i \Psi Z_i^T + \sigma^2 I_{n_i}$. It follows that $y_i \sim \mathcal{N}(X_i\beta, V_i)$, and for a given Ψ and σ, we have a closed form maximum likelihood estimate of β, $\hat{\beta} = \left(\sum_{i=1}^{M} X_i^T \hat{V}_i^{-1} X_i\right)^{-1} \sum_{i=1}^{M} X_i^T \hat{V}_i^{-1} y_i$. The estimates of Ψ and σ are obtained via the EM algorithm [23, 24] or the Newton-Raphson procedure [25].

2.3.2 Nonlinear Mixed Effects Model

In section 2.2, we discussed the need for nonlinear growth curves to model nonlinear changes of early brain development. The nonlinear mixed effect model (NLME) is a generalization of linear mixed effect and nonlinear regression. In NLME, some or all of the fixed or random effects enter the model nonlinearly. In the NLME model, each individual's response is modeled as:

$$y_i = f(\phi_i, t_i) + e_i, \tag{2.15}$$

where $\phi = A_i\beta + B_i b_i$. Similar to the linear mixed effect model, β are the fixed effect and b_i are random effects with distribution $\mathcal{N} \sim (0, \Psi)$. A_i and B_i are design matrices that indicate whether a specific fixed or random effect should be included in the model. The function f can be any nonlinear function. In section 2.4, we evaluate different nonlinear functions that may be candidates for modeling early brain development.

2.3.2.1 Parameter Estimation

Similar to linear mixed effects models, parameter estimation of NLME is also based on the maximum likelihood of marginal density of responses y as in (2.14). However, in the nonlinear mixed effects models, there is no closed form solution to this integral. We use the approximation method proposed by Lindstrom and Bates to obtain the model parameters [20].

This approximation method uses the Taylor expansion of model function f around conditional modes of random effects b and the current estimate of β to approximate the integral in (2.14). This method alternates between two steps, a penalized nonlinear least squares step and a linear mixed effects step [20].

2.3.2.2 Inference

The distribution of maximum likelihood estimator β of the fixed effect based on the linear mixed effect approximation is:

$$\hat{\beta} \sim \mathcal{N}\left(\beta, \left[\sum_{i=1}^{M} \hat{X}_i^T \hat{V}_i^{-1} \hat{X}_i\right]^{-1}\right), \tag{2.16}$$

where $\hat{V} = Z_i \Psi \hat{Z}_i^T + \sigma^2 I_{n_i}$, $\hat{X}_i = \frac{\partial f_i}{\partial \beta^T}|_{\hat{\beta},\hat{b}_i}$, $\hat{Z}_i = \frac{\partial f_i}{\partial b_i^T}|_{\hat{\beta},\hat{b}_i}$. Approximate confidence intervals of fixed effects can be calculated based on the estimated β and its sampling distribution. The approximate confidence interval of level $1-\alpha$ and for the kth fixed effects is

$$\hat{\beta}_k \pm t_{df_k}(1-\alpha/2)\sqrt{\left[\sum_{i=1}^{M} \hat{X}_i^T \hat{V}_i^{-1} \hat{X}_i\right]^{-1}}, \tag{2.17}$$

where $t_{df_k}(1-\alpha/2)$ denotes the $1-\alpha/2$ quantile of the t-distribution with df_k degrees of freedom.

For hypothesis testing, we also use $\hat{\beta}$ and its sampling distribution. For example, if we want to test whether our null hypothesis $\beta_k = 0$, a general t-statistic can be constructed as follows:

$$t = \frac{\hat{\beta}_k}{\sqrt{\left[\sum_{i=1}^{M} \hat{X}_i^T \hat{V}_i^{-1} \hat{X}_i\right]^{-1}}}. \tag{2.18}$$

2.4 Experiments and Results

2.4.1 Model Selection

Two important aspects of modeling longitudinal data are 1) modeling mean response (fixed effects) and 2) modeling the covariance or time dependence among the repeated

measures (structure of random effects). In section 2.2, we discussed various growth functions that could be used to model the mean responses of diffusion parameters of DTI or intensity values of structural MRI. Some of these models fall under the linear mixed effects modeling, such as polynomials, whereas the other parametric growth models of section 2.2 fall in the category of nonlinear mixed effects modeling. One important aspect of model selection is which growth curves we should choose for analyzing change over time. The model selection becomes more complicated in the mixed-effects models as selecting the best model has to include not only criteria on selecting the mean structure (fixed effects), but also the variance-covariance structure of random effects.

For example, let us consider modeling growth by a simple linear trend. Do we allow only intercept to vary among individuals, or do we allow both intercept and slope to vary among individuals? Also in the nonlinear mixed effects model, if we want to model growth via the Gompertz function, which parameters or combination of parameters of the Gompertz function do we allow to vary randomly among individuals? Various models can be constructed for each growth curve based on inclusion of different combinations of random effects. In the linear mixed effects model, backward and forward model building procedures have been suggested. In the forward procedure, models are initially fit with only the intercept term as a random effect. Then the linear term, and then quadratic and higher order terms are added to the model if their inclusion is significant.

The backward elimination model starts the modeling by including all the fixed effects as random effects and removing one variable at a time starting with higher order terms as long as their removal does not make a significant difference in the model. The likelihood ratio test can be used to test nested models (when one model represents a special case of another model, i.e., if L_2 is the likelihood of the more general model and L_1 is the likelihood of the restricted model). The likelihood ratio test is

$$2log(L_2/L_1) = 2\left[log(L_2) - log(L_1)\right]. \tag{2.19}$$

The likelihood ratio test statistic is χ^2 distributed with $k_2 - k_1$ degrees of freedom, where k_i is the number of parameters to be estimated in model i.

In nonlinear mixed effects modeling, there is no order about inclusion of random effects, so forward and backward procedures do not apply. Also, likelihood ratio tests are not applicable if we are comparing models that have different fixed effects (i.e., logistic vs. Gompertz). To overcome shortcomings of the likelihood ratio test, we prefer to use the Akaike Information Criteria (AIC) as an alternative model selection,

$$AIC = -2log(L_i) + 2n_{par}, \tag{2.20}$$

where L_i is the likelihood of model i and n_{par} is the number of parameters in the model. Under this formulation, a smaller AIC indicates a better model fit.

To select a model to characterize changes of structural and diffusion parameters of MRI for early brain development, we prefer a growth curve that has lower AIC measures, provides physical intuition about growth, and does not violate knowledge about development already existing in the literature.

2.4.2 Evaluation of Growth Curves

To select among the variety of developmental models introduced in section 2.2, we fit these growth curves to longitudinal diffusion data of 26 healthy individuals ranging from 2 weeks to 2 years old. Multiple regions of interests that are known to have a distinctive pattern of development were selected to evaluate the model fit. As mentioned in section 2.4.1, not only do we need to select among growth models (i.e., polynomials, exponential, monomolecular, logistic, and Gompertz), we also need to select how many of the fixed effects in these models are allowed to vary randomly among subjects.

The following criterion was used to select random effects for each growth curve: for linear models, the forward procedure was applied in selecting the combination of random effects. For nonlinear mixed effects models, a maximum of two parameters was used for random effects. If the parameters are highly correlated or the individuals do not exhibit large variation with regard to the corresponding parameter, inclusion of the extra random effects poses challenges in the estimation [26]. Thus, we limit the number of random effects to two for nonlinear mixed effects models. We evaluate the model fits on fractional anisotropy (FA), which shows an increasing trend over time, and radial diffusivity (RD), which shows a decreasing trend over time.

Table 2.1 displays the results of model fitting to observed FA values of longitudinal data for posterior thalamic radiation as is shown in Fig. 2.2. Among linear and quadratic growth curves, the linear trend with only the intercept term and the quadratic model also with only the intercept term as random effects were among the best models for the polynomial group for not only this region, but also for the majority of the regions that we analyzed.

Table 2.2 displays the results for varying random effects of the monomolecular model when the growth rate is limited. This model has two random effects: α, which is the asymptote as x approaches infinity, and r, which is the rate constant. The y value at $x = 0$ is assumed to be zero. For most regions, inclusion of both parameters α and r as random effects improved the model fitting.

Table 2.1: Comparison of Linear Mixed Effects Model.

Model	df (NLME)*	AIC
FA.lme.quadratic1 (random effects: intercept)	5	939.96
FA.lme.quadratic3 (random effects: all the parameters)	10	942.40
FA.lme.quadratic2 (random effects: intercept & age)	7	943.96
FA.lme (random effects: intercept)	4	966.85
FA.lme2 (random effects: intercept & slope)	6	970.66

*df(NLME) refers to the degrees of freedom used in the NLME model. Degrees of freedom are calculated based on the number of fixed effects β, the unique parameters of the variance-covariance of random effects Ψ, and the within-group error term σ.

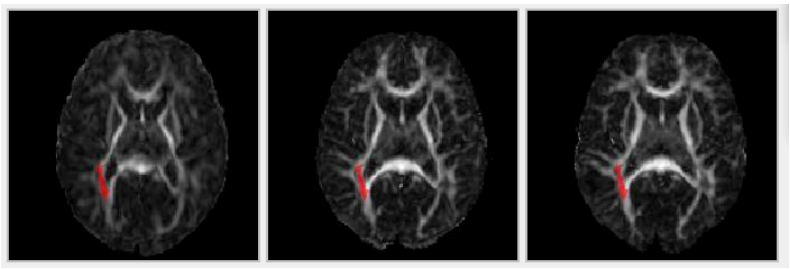

Figure 2.2: Posterior thalamic radiation is shown as a red label on the longitudinal FA images of one subject. Images taken at 2 weeks, 1 year, and 2 years.

Table 2.2: Comparison of Two-parameter Monomolecular Model.

Model	df (NLME)	AIC
FA.nlme.monomolecular.αr (random effects: all the parameters)	6	994.50
FA.nlme.monomolecular.r (random effects: r)	4	1001.03
FA.nlme.monomolecular.α (random effects: α & r)	4	1022.49

Table 2.3 displays the results for the three-parameter monomolecular model where κ is added to the model. κ is the value at $x = 0$, so the model does not have to pass through the origin as does the two-parameter monomolecular model. Inclusion of random effects α and κ yielded the best fits among monocular models for most of the brain regions based on the AIC measures.

Tables 2.4 and 2.5 display the results for logistic and Gompertz growth curves. For the logistic function, inclusion of α parameter or both α and r were among the best models for the majority of regions, whereas for the Gompertz function, inclusion of only α or inclusion of both α and d (delay) resulted in the lowest AICs.

Fig. 2.3 shows the results of model fitting via linear and nonlinear mixed effects mod-

Table 2.3: Three-parameter Monomolecular Model.

Model	df (NLME)	AIC
FA.nlme.monomolecular.$\alpha\kappa$ (random effects: α & κ)	7	975.61
FA.nlme.monomolecular.α (random effects: α)	5	987.91
FA.nlme.monomolecular.αr (random effects: α & r)	7	991.90
FA.nlme.monomolecular.r (random effects: r)	5	1001.00
FA.nlme.monomolecular.κ (random effects: κ)	5	1015.89

Table 2.4: Logistic Model.

Model	df (NLME)	AIC
FA.nlme.logis.α (random effects: α)	5	976.54
FA.nlme.logis.η (random effects: η)	5	1015.83

Not all the models converged.

Table 2.5: Gompertz Model.

Model	df (NLME)	AIC
FA.nlme.gompertz.αd (random effects: α & d)	7	976.34
FA.nlme.gompertz.α (random effects: α)	5	976.60
FA.nlme.gompertz.αr (random effects: α & r)	7	980.59
FA.nlme.gompertz.d (random effects: d)	5	1015.86
FA.nlme.gompertz.dr (random effects: d & r)	7	1019.86

eling for posterior thalamic radiation. Combinations of random effects were selected for each growth curve based on the AIC. The linear models do poorly outside the range of observed data and also violate the asymptotic property that is known for this age group. Among the nonlinear growth models, all three growth curves—monomolecular, logistic, and Gompertz—seem to fit the observed range of the data similarly. The monomolecular growth curve can predict values less than zero, which is not possible for diffusion measures. Gompertz has a smaller AIC compared to logistic for most regions that we analyzed. Overall, the Gompertz function with asymptote and delay as random effects performed reasonably well compared to other growth curves and has the asymptotic properties in the observed age range that are known from pediatric neuroanatomy.

We also performed a similar model building procedure for radial diffusivity, RD, that shows a decreasing trend. For modeling a decreasing trend, we used linear mixed effect models similar to the ones shown for modeling FA. In the case of the nonlinear mixed effects models, we used the exponential decay function and dropped the two-parameter

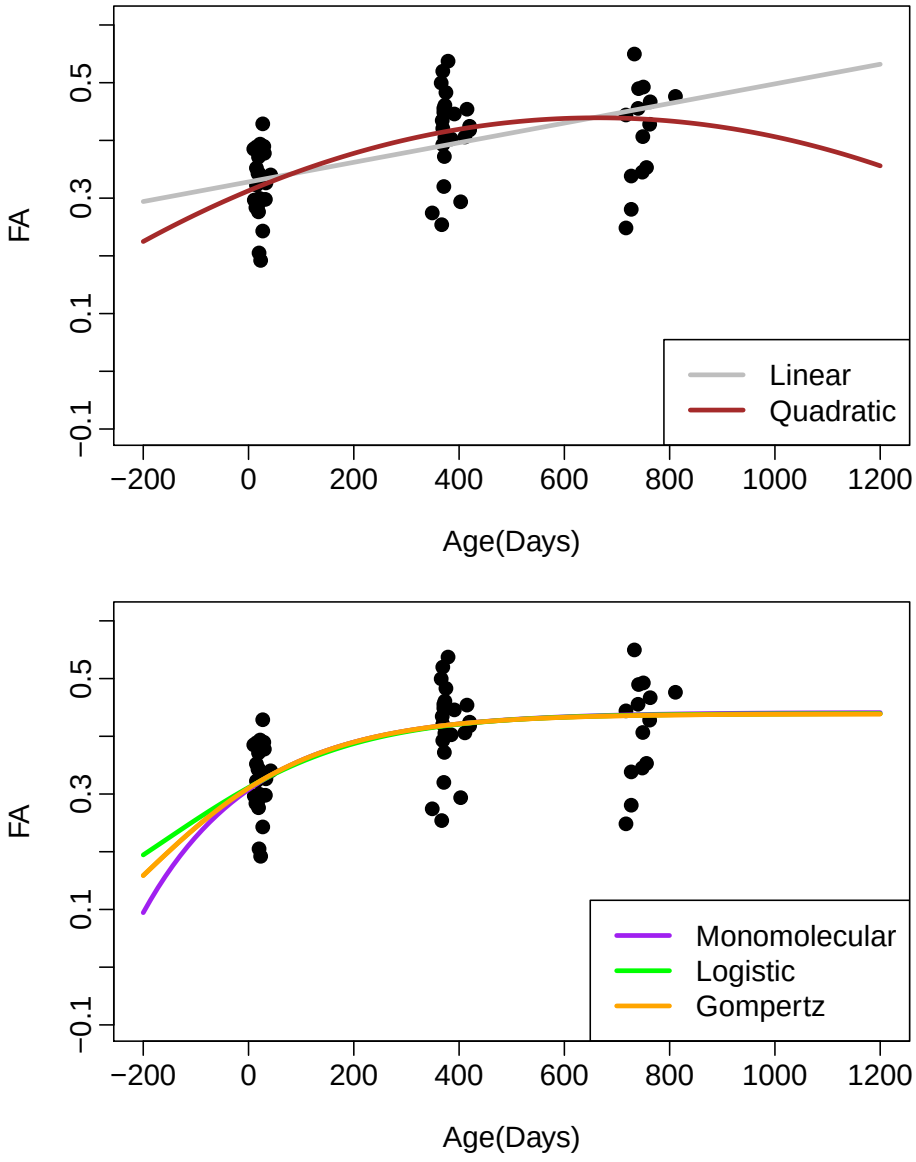

Model	df (NLME)	AIC
FA.nlme.monomolecular.$\alpha\kappa$ (random effects: α & κ)	7	910.63
FA.nlme.gompertz.αd (random effects: α & d)	7	911.93
FA.nlme.logis.α (random effects: α)	5	919.01
FA.lme.quadratic1 (random effects: intercept)	5	919.01
FA.lme (random effects: intercept)	4	929.80

Figure 2.3: Comparison of different growth models for longitudinal FA data. Top: linear mixed effect models; Middle: nonlinear mixed effect models. Linear mixed effects models are not valid beyond the observed range of data.

monomolecular model as this model makes a strong assumption that the y value is zero; at time point zero, however, this is not the case for the DTI data. Here, time zero means when subjects are born, and clearly the diffusion values are not zero at that time. Among the models considered, the quadratic model with all the parameters as random effects performed the best among linear models. Exponential models with the asymptote as random effects performed better compared to other combinations of random effects. For the Gompertz function, including asymptote and delay, α and d, as random effects resulted in the lowest AIC for the majority of regions.

Fig. 2.4 shows the results of growth curves with their best combination of random effects (i.e., the combination of random effects that yielded the lowest AIC measure for a given growth curve). As is evident in the plots, the linear mixed effects models of polynomials do poorly outside the range of observed values. Monomolecular and Gompertz growth curves do a better job of modeling the observed changes and show asymptotic properties that are known in the literature. Between monomolecular and Gompertz growth functions, Gompertz did have lower AIC measures.

We also evaluated other properties of the models, such as how realistic the prediction is and how well the model matches what is known about the development process during infancy. We know that the growth rate cannot be constant during this time period. We also know that diffusion parameters and intensity values of MRI seem to saturate by age 2. We therefore prefer models with asymptotic behavior. We prefer nonlinear growth functions rather than polynomials, as the parameters of nonlinear growth functions usually can be related to biological processes, and polynomial functions tend to make spurious upward/downward predictions that are not biological at this age. Another problem with some of the models, such as monomolecular models, is that they can predict negative values for earlier time points, which is not possible for diffusion or intensity values of MRI. Gompertz and logistic models are both sigmoid type functions and have asymptotic properties as $x \to \infty$ and $x \to -\infty$. For FA values, Gompertz and logistic models had similar AIC measures, with Gompertz having slightly lower AIC measures for the majority of regions. However, for RD measures, we had convergence issues with the logistic function and Gompertz performed relatively better based on the AIC measures for the majority of regions. The Gompertz curve fits the data well and uses intuitive parameters related to growth such as asymptote, delay, and speed. For the rest of this chapter and in following chapters, we therefore use the Gompertz model with asymptote and delay as random effects for our growth curve.

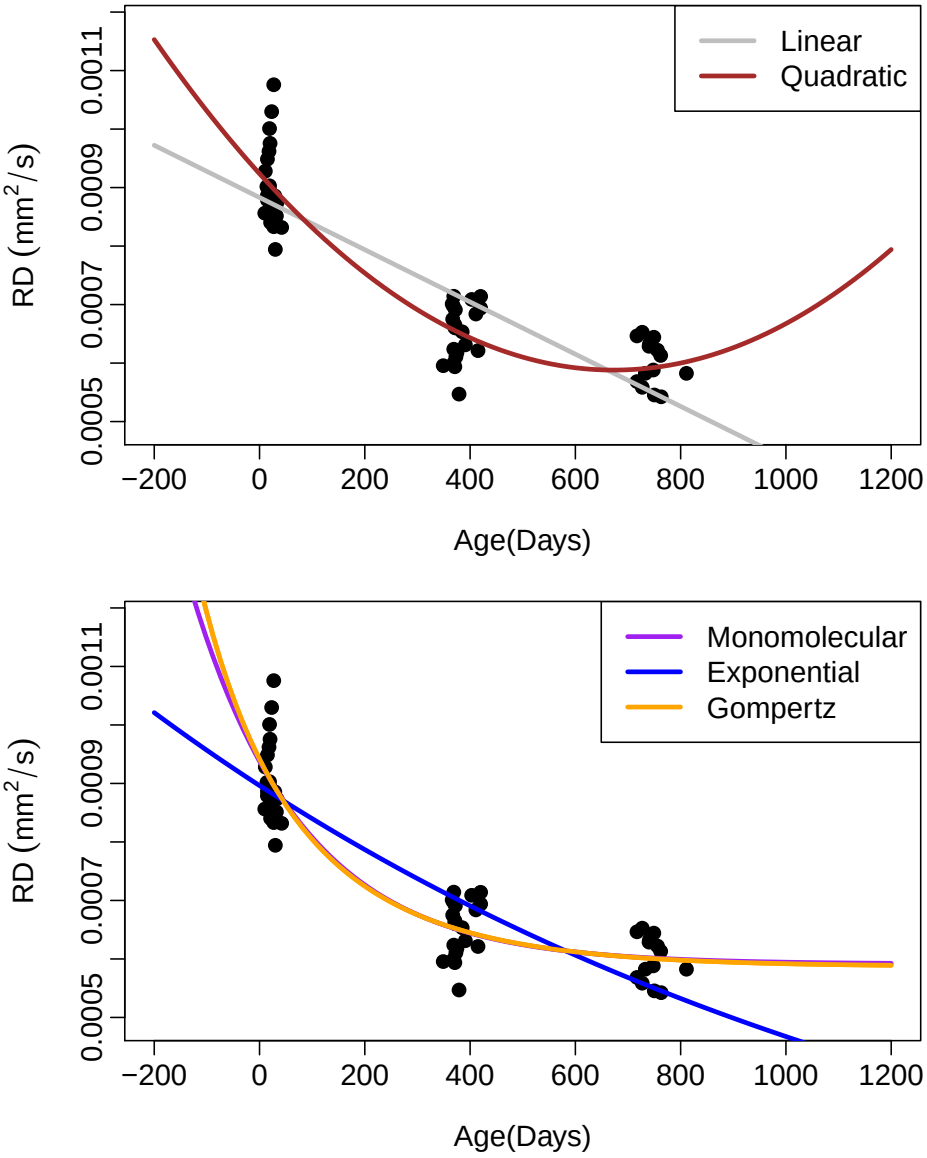

Model	df (NLME)	AIC
Gompertz (random effects: α & d)	7	352.03
Monomolecular (random effects: α & κ)	7	353.95
Quadratic (random effects: intercept)	5	362.12
Exponential (random effects: α)	4	395.78
Linear (random effects: intercept)	4	407.80

Figure 2.4: Comparison of different growth models for longitudinal RD data of posterior thalamic radiation. Top: linear mixed effects models; Middle: nonlinear mixed effects models.

2.4.3 Hypothesis Testing

We generated synthetic longitudinal data to ensure our analysis methodology can capture underlying differences as presented in the synthetic data. Random data representing two regions (R_1 and R_2) are generated, and we verify that the overall trend of the population and each subject's specific growth trajectory matches the known ground truth. We also verify that the Gompertz parameters are significantly different between the two regions in a way that matches the synthetic model. Synthetic longitudinal data are generated following (2.15) where $\beta^{R_1} = [0.8, 0.6, .991]$, $\Psi = diag(0.04^2, 0.02^2, .002^2)$, and $\sigma^2 = 0.005^2$. Values for three time points of 15 subjects are generated while keeping some of the fixed parameters of β^{R_2} the same as β^{R_1}. We then vary one, two, or all of the fixed parameters of R_2 and perform hypothesis testing between two regions to identify fixed parameters that are significantly different between these two regions. Fig. 2.5, 2.6, and 2.7 summarize some of our experimental results. The results demonstrate that our approach can detect significant discriminatory features of growth patterns in a pair of regions in terms of Gompertz parameters.

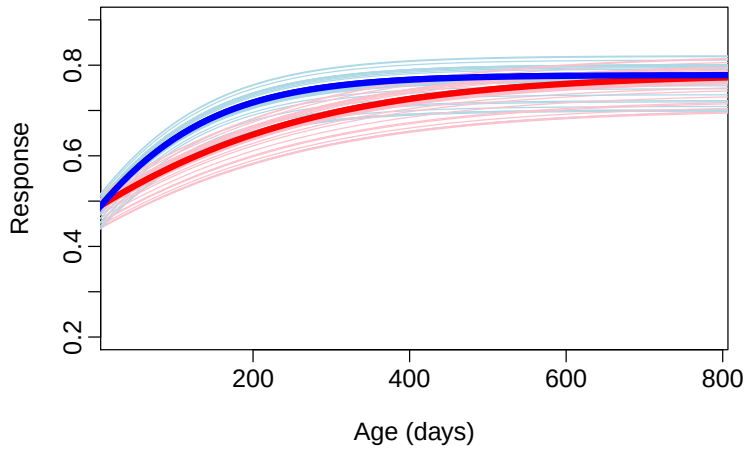

	Truth R_1	Estimated R_1	Truth R_2	Estimated R_2	p-value
β_1	0.8	0.7764	0.8	0.8022	0.9981
β_2	0.5	0.4898	0.5	0.4844	0.7488
β_3	.991	0.9889	0.995	0.9951	1.33×10^{-5}

Figure 2.5: Example of randomly generated synthetic longitudinal data for two regions colored blue (R_1) and red (R_2) by varying β_3 between the two regions. Hypothesis testing correctly identifies β_3 as being significantly different between these two regions.

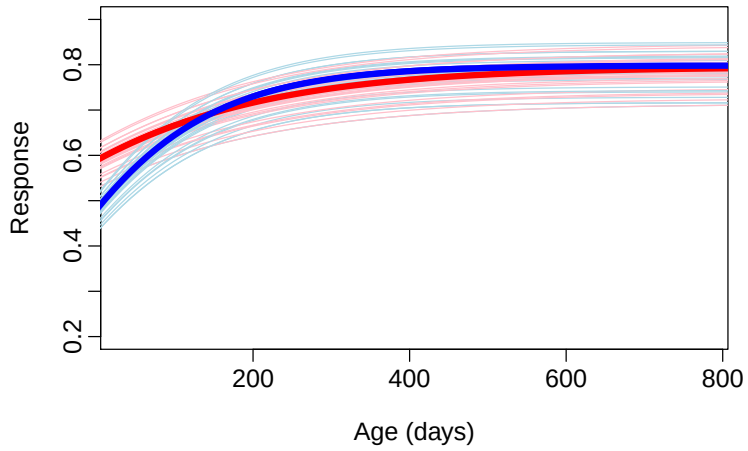

	Truth R_1	Estimated R_1	Truth R_2	Estimated R_2	p-value
β_1	0.8	0.7848	0.8	0.79	0.7109
β_2	0.5	0.4916	0.3	0.2971	4.19×10^{-24}
β_3	0.991	0.9913	0.995	0.9945	3.51×10^{-06}

Figure 2.6: Example of randomly generated synthetic longitudinal data for two regions colored blue (R_1) and red (R_2) by varying β_2 and β_3 between the two regions. Hypothesis testing correctly identifies β_2 and β_3 as being significantly different between these two regions.

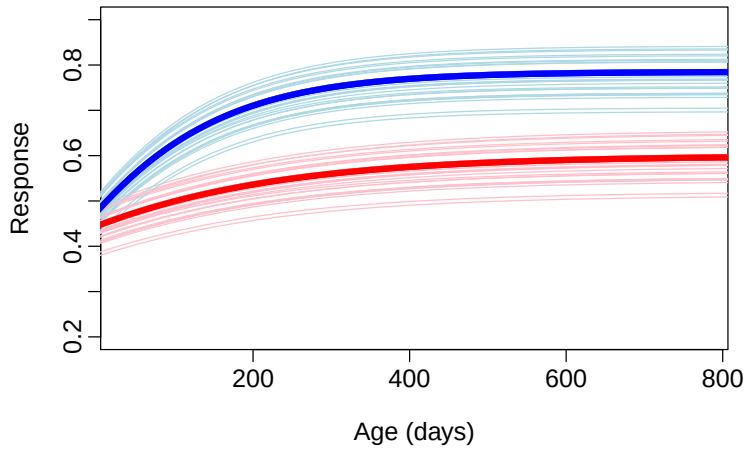

	Truth R_1	Estimated R_1	Truth R_2	Estimated R_2	p-value
β_1	0.8	0.8206	0.6	0.6057	1.32×10^{-25}
β_2	0.5	0.4965	0.3	0.2917	5.01×10^{-26}
β_3	0.991	0.9911	.995	0.9949	3.93×10^{-06}

Figure 2.7: Example of randomly generated synthetic longitudinal data for two regions colored blue (R_1) and red (R_2) by varying β_1, β_2, and β_3 between the two regions. Hypothesis testing correctly identifies all the fixed parameters as being significantly different between these two regions.

CHAPTER 3

REGIONAL CHARACTERIZATION OF LONGITUDINAL DT-MRI TO STUDY WHITE MATTER MATURATION OF THE EARLY DEVELOPING BRAIN

Reprinted with permission from N. Sadeghi, M. Prastawa, P.T. Fletcher, J. Wolff, J. H. Gilmore, and G. Gerig. "Regional characterization of longitudinal DT-MRI to study white matter maturation of the early developing brain." *NeuroImage*, vol. 68, pp. 236–247, 2013.

NeuroImage 68 (2013) 236–247

Contents lists available at SciVerse ScienceDirect

NeuroImage

journal homepage: www.elsevier.com/locate/ynimg

Regional characterization of longitudinal DT-MRI to study white matter maturation of the early developing brain

Neda Sadeghi [a,*], Marcel Prastawa [a], P. Thomas Fletcher [a], Jason Wolff [b], John H. Gilmore [c], Guido Gerig [a]

[a] Scientific Computing and Imaging Institute, University of Utah, Salt Lake City, UT 84112, USA
[b] Carolina Institute for Developmental Disabilities, University of North Carolina, Chapel Hill, NC 27599, USA
[c] Department of Psychiatry, University of North Carolina, Chapel Hill, NC 27599, USA

ARTICLE INFO

Article history:
Accepted 15 November 2012
Available online 9 December 2012

Keywords:
Longitudinal brain imaging
Early brain development
DTI
Nonlinear mixed effect modeling

ABSTRACT

The human brain undergoes rapid and dynamic development early in life. Assessment of brain growth patterns relevant to neurological disorders and disease requires a normative population model of growth and variability in order to evaluate deviation from typical development. In this paper, we focus on maturation of brain white matter as shown in diffusion tensor MRI (DT-MRI), measured by fractional anisotropy (FA), mean diffusivity (MD), as well as axial and radial diffusivities (AD, RD). We present a novel methodology to model temporal changes of white matter diffusion from longitudinal DT-MRI data taken at discrete time points. Our proposed framework combines nonlinear modeling of trajectories of individual subjects, population analysis, and testing for regional differences in growth pattern. We first perform deformable mapping of longitudinal DT-MRI of healthy infants imaged at birth, 1 year, and 2 years of age, into a common unbiased atlas. An existing template of labeled white matter regions is registered to this atlas to define anatomical regions of interest. Diffusivity properties of these regions, presented over time, serve as input to the longitudinal characterization of changes. We use non-linear mixed effect (NLME) modeling where temporal change is described by the Gompertz function. The Gompertz growth function uses intuitive parameters related to delay, rate of change, and expected asymptotic value; all descriptive measures which can answer clinical questions related to quantitative analysis of growth patterns. Results suggest that our proposed framework provides descriptive and quantitative information on growth trajectories that can be interpreted by clinicians using natural language terms that describe growth. Statistical analysis of regional differences between anatomical regions which are known to mature differently demonstrates the potential of the proposed method for quantitative assessment of brain growth and differences thereof. This will eventually lead to a prediction of white matter diffusion properties and associated cognitive development at later stages given imaging data at early stages.

Introduction

Improved understanding of typical brain development during infancy, an interval characterized by rapid sculpting, organization and vulnerability to exogenous influences, is of a great importance both for clinical and scientific research. Many neurobehavioral disorders have their origins during neurodevelopment (Gilmore et al., 2010; Huppi, 2008). Establishing a normative model of early brain development is a critical step to understanding the timing and potential mechanisms of atypical development and how intervention might alter such trajectories and improve developmental outcomes (Als et al., 2004; Marsh et al., 2008). Once normative models are available, they can inform research and practice concerning children at risk for neurodevelopmental disorders and may eventually lead to earlier and improved diagnosis and treatment. Longitudinal trajectory-based studies provide a better understanding of human brain development compared to cross-sectional studies (Karmiloff-Smith, 2010). In cross-sectional data, calculation of the average trajectory may not be representative for the growth patterns of individual subjects as this approach is inherently insensitive to individual developmental differences and cohort effects (Gogtay et al., 2004). Cross-sectional analysis might falsely report magnitude of changes over time or may fail to detect changes (Casey et al., 2005).

Growth modeling from longitudinal data, on the other hand, makes use of sets of individual temporal trajectories which results in significantly improved models of growth and growth variability, as longitudinal studies can differentiate between cohort and age effects (Diggle et al., 2002).

Previous imaging studies of early brain development have substantially contributed to our current understanding of brain development. Some of the studies considered size or shape differences (Huppi, 2008; Knickmeyer et al., 2008; Xu et al., 2008; Xue et al., 2007), others have looked at changes of contrast in MRI (Sadeghi et al., 2010) or

* Corresponding author.
E-mail address: neda@sci.utah.edu (N. Sadeghi).

1053-8119/$ – see front matter © 2012 Elsevier Inc. All rights reserved.
http://dx.doi.org/10.1016/j.neuroimage.2012.11.040

diffusion parameters in DTI (Gao et al., 2009; Geng et al., 2012; Hermoye et al., 2006; Huppi et al., 1998; Mukherjee et al., 2002; Sadeghi et al., 2012). However, most of these studies are based on cross-sectional data or children older than 2 years (Dubois et al., 2008; Faria et al., 2010; Gao et al., 2009; Hermoye et al., 2006; Mukherjee et al., 2002). In this study we focus on developing longitudinal models spanning birth to about two years of age. The models are based on the parameters obtained from diffusion tensor imaging (DTI). DTI-derived diffusivity parameters provide relevant information about the maturation of the underlying tissue as they assess water content (Huppi, 2008). These measurements are a possible reflection of axonal density and/or degree of myelination (Neil et al., 1998; Song et al., 2002) which correlate with cognitive functions (Dubois et al., 2006) and early developmental outcomes (Als et al., 2004; Ment et al., 2009; Wolff et al., 2012). In this study we focus on fractional anisotropy (FA), mean diffusivity (MD), radial (RD) and axial diffusivity (AD) to explain brain maturation and to gain a better understanding of white matter development. Driven by earlier findings that myelination follows a nonlinear spatio-temporal pattern (Dubois et al., 2008), our goal is to capture these changes in terms of the parameters of the Gompertz function which provides an intuitive parameterization representing delay, growth, and asymptotic values for each region.

In contrast to previous studies, we use an explicit growth function (the Gompertz function) and a nonlinear mixed effect modeling scheme (Pinheiro and Bates, 2000). In a nonlinear mixed effects model, the diffusion parameters are modeled in a hierarchical fashion, with fixed-effect representing the overall population trend, and random effect associated with each individual. Nonlinear mixed effect models are suited for longitudinal data where each subject has repeated scans with the possibility of missing data points and uneven spacing between scans of all the individuals in the group. Unlike most previous studies of early brain development, we make use of longitudinal imaging where each subject is imaged repeatedly over the first few years of life. This enables a more accurate characterization of developmental pattern (Giedd et al., 1999). Nonlinear mixed effect model provides a direct way of estimating individual trajectories along with longitudinally derived typical developmental curves as illustrated in Fig. 2. This leads to the characterization of a normative model for healthy developmental patterns and estimation of personalized, individual trajectories of growth, which is a property that will be desirable for comparison and diagnostic assessment of individual subjects.

We apply our analysis framework to a set of white mater regions that are known to have different patterns of growth to establish normative developmental patterns for each region. Quantitative analysis of diffusion changes in these regions provide further insight into brain maturation process and will enable prediction of subject-specific growth trajectory with the potential of detecting pathological deviation related to brain disorders.

Materials and methods

Subjects

This study was approved by the Institutional Review Board of the University of North Carolina School of Medicine. Children analyzed in this study are controls in an ongoing longitudinal study of early brain development in high risk children (Geng et al., 2012). A total of 26 control subjects were selected for this study. Scans of these subjects were obtained at around two weeks, 1 year and 2 years. Four of the subjects had sub-optimal scans at 1 year that were removed, but their scans for other time points were kept. In total, we used 59 datasets, the temporal distribution of scan data is shown in Table 1. To ensure maximal success rate of scanning, all subjects were fed, swaddled and fitted with ear protection. All subjects were scanned without sedation during their natural sleep.

Table 1
Distribution of scans across different time points. *N* indicates the number of subjects with the associated temporal pattern.

Available scans	N
Neonate scan only	2
1 year scan only	0
2 year scan only	0
Neonate + 1 year scan	10
Neonate + 2 year scan	2
1 year + 2 year scan	3
Neonate + 1 year + 2 year scan	9

Image acquisition and data processing

All images were acquired using a 3 T Allegra head-only MR system using a single shot echo-planar spin echo diffusion tensor imaging sequence with the following parameters: TR = 5200 ms, TE = 73 ms, slice thickness of 2 mm and in-plane resolution of 2×2 mm^2. One image without diffusion gradients (b = 0) along with 6 gradient directions with a b-value of 1000 mm^3/s were acquired. The sequence was repeated 5 times for improved single-to-noise ratio. All DWIs were checked and corrected for motion artifacts using the DTIChecker tool.[1] Tensor maps were calculated for each DTI scan using weighted least squares tensor estimation on the images that have been averaged over sequence repeats (Salvador et al., 2005). T2-weighted structural images were obtained using turbo spin echo sequence with TR = 7 s, TE = 15 and 90 ms, slice thickness of 1.95 mm and in-plane resolution of 1.25×1.25 mm^2. T2W and baseline DWI of all the subjects' scans were skull stripped using Brain Extraction Tool (BET) (Smith, 2002).

Due to significant contrast changes in early brain development, we utilized two registration frameworks: one for intra-subject and inter-modality registration, and the other for inter-subject registration. For inter-subject registration, we applied the unbiased atlas building framework of Joshi et al. (2004) based on the Large Deformation Diffeomorphic Metric Mapping (LDDMM) (Miller et al., 2002) to the set of T2W images of scans at year 1 to obtain spatial mappings between all subjects through the estimated atlas coordinate system. Intra-subject registration was performed by IRTK software, using affine and nonlinear registration method of Rueckert et al. (1999) using normalized mutual information as the image match metric (Studholme et al., 1999) that appears robust to changing contrast properties in early brain development.[2] All time points of each subject are registered to the unbiased atlas via linear and non-linear transformations, first by mapping these images to the year 1 scan and then cascading the two transformations for a mapping to the atlas. Details on the registration methods and parameters are summarized in Appendix A. The tensors are registered to the atlas using transformations obtained by registering the DTI baseline (B0) images to T2W images. Tensors are resampled using finite strain reorientation and Riemannian interpolation (Alexander et al., 2001; Fletcher and Joshi, 2007; Pennec et al., 2006). After all the images are transformed into the atlas space, the tensors are averaged using the log-Euclidean method to produce a tensor atlas (Arsigny et al., 2006). In this study, we extract the mean, axial, radial diffusivity, and fractional anisotropy features from the registered tensors, $MD = \frac{\lambda_1+\lambda_2+\lambda_3}{3}$, $AD = \lambda_1$, $RD = \frac{\lambda_2+\lambda_3}{2}$ and $FA = \sqrt{\frac{1}{2}}\frac{\sqrt{(\lambda_1-\lambda_2)^2+(\lambda_1-\lambda_3)^2+(\lambda_2-\lambda_3)^2}}{\sqrt{\lambda_1^2+\lambda_2^2+\lambda_3^2}}$ where λ_i are the eigenvalues of the tensor sorted from largest to smallest. Fig. 1 shows an overview of our method and analysis workflow.

Nonlinear mixed effects model

In this subsection, we describe the nonlinear mixed effects model used to analyze the longitudinal DTI data. Compared to a nonlinear

[1] http://www.ia.unc.edu/dev/download/dtichecker.
[2] http://www.doc.ic.ac.uk/~dr/software.

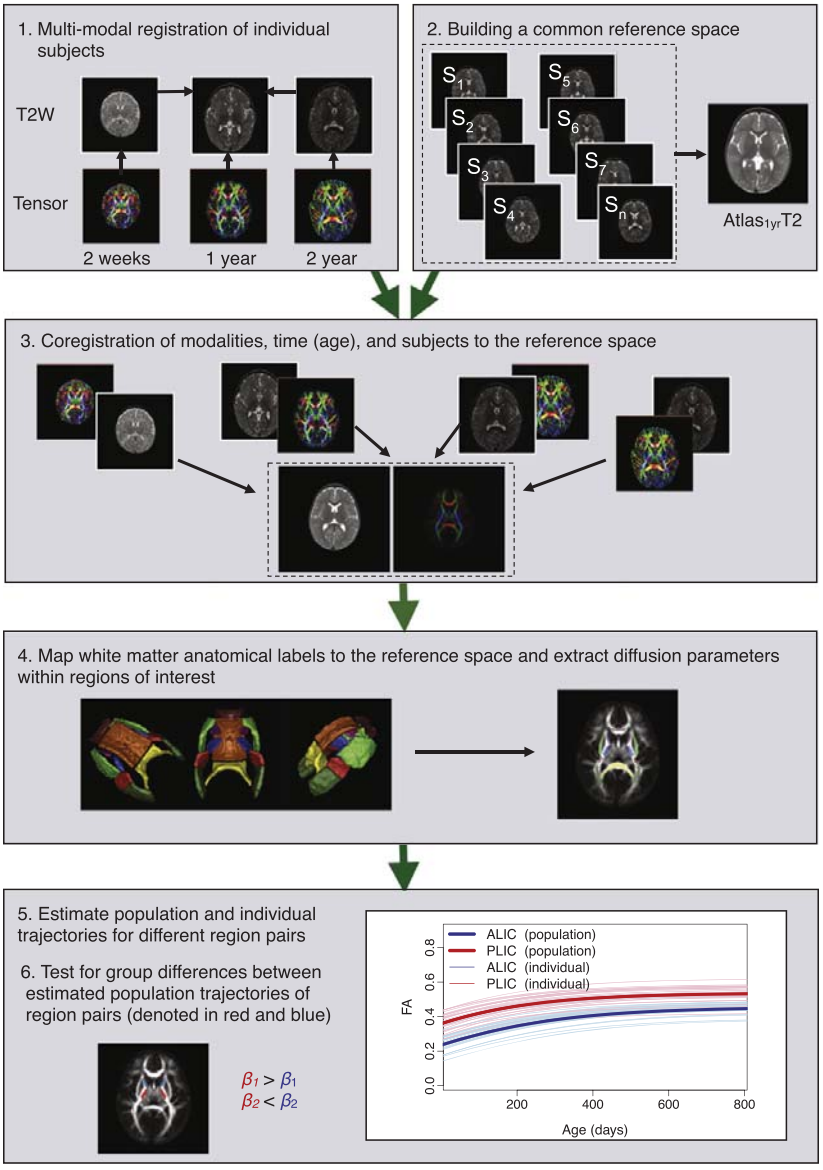

Fig. 1. Overview of the proposed longitudinal DTI region based analysis.

least squares (NLS) method, a nonlinear mixed effects (NLME) model does not assume that the sample data points are independent and identically distributed, rather it assumes that there is correlation across repeated measurements. Also, the average trend estimated based on the mixed effect model is an average of individual trajectories rather than a least squares fit to the individual data points. This results in better representation of trajectories in the population as illustrated in Fig. 2.

Model formulation

In the mixed effects model, the observed data is a combination of fixed effects which are parameters associated with the entire population or a sub-population, and random effects which are parameters associated to an individual. In the nonlinear mixed effect models, some or all the parameters appear nonlinearly in the model. We use the NLME model proposed by Lindstrom and Bates (1990) where each individual's observation is modeled as:

$$y_{ij} = f\left(\phi_i, t_{ij}\right) + e_{ij} \quad i = 1, \cdots, M; \quad j = 1, \cdots, n_i \tag{1}$$

where i indexes the individual subjects and j indexes the time points, M is the number of individuals, n_i is the number of observations on the ith individual, f is a nonlinear function of the covariate vector (time) t_{ij} and parameter vector ϕ_{ij}, and $e_{ij} \sim N(0,\sigma^2)$ is an i.i.d. error

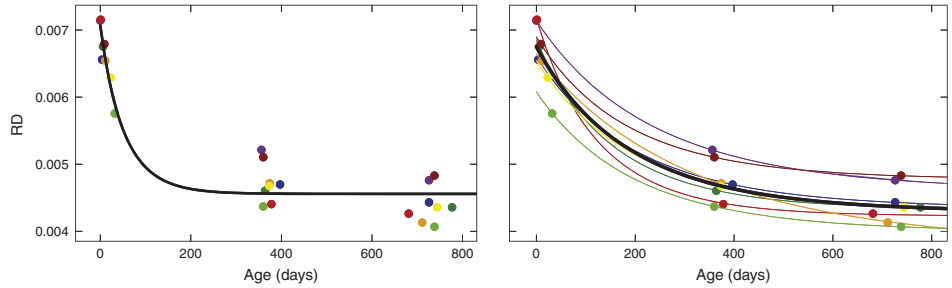

Fig. 2. Population growth models, represented as black curves, obtained using nonlinear least squares (NLS) in a cross-sectional fashion (left) and nonlinear mixed effect modeling (NLME) via longitudinal analysis (right). Colored points represent data observations, and colored curves represent the individual growth trajectories. Note that given the same data points, cross-sectional analysis provides a very different result than longitudinal analysis.

term. The parameter vector can vary among individuals by writing ϕ_i as

$$\phi_i = A_i\beta + B_i b_i \; b_i \sim N(0, \Psi) \tag{2}$$

where β is a p-vector of fixed effects, and b_i is a q-vector of random effects associated with individual i with variance–covariance Ψ. A_i and B_i are identity matrices for our study.

The function f can be any nonlinear function. Since early brain development is characterized by rapid initial development which slows down in later years, it is preferable to use growth functions which reflect these properties. One such growth function is the Gompertz function which can be written as:

$$y = \textbf{asymptote} \;\; \exp(-\textbf{delay} \;\; \exp(-\textbf{speed} \;\; t)). \tag{3}$$

The effects of varying the three parameters asymptote, delay and speed of the Gompertz function are shown in Fig. 3, for a function that decreases as time progresses.

To use the Gompertz function in the nonlinear mixed effect model, we apply the following formulation where the Gompertz function is parameterized as $y = f(\phi, t) = \phi_1 \exp\{-\phi_2 \phi_3^t\}$, where ϕ_1 denotes asymptote, ϕ_2 is delay, and ϕ_3 is exp(−speed). Combining the nonlinear mixed effect model with the Gompertz function, each observation can be represented as follows:

$$y_{ij} = f\left(\phi_i, t_{ij}\right) + e_{ij} = \phi_{1i} \exp\left\{-\phi_{2i}\phi_{3i}^{t_{ij}}\right\} + e_{ij} \tag{4}$$

where the mixed effects are $\phi_i = [\phi_{1i} \;\; \phi_{2i} \;\; \phi_{3i}]^T = \beta + b_i$, the fixed effects are $\beta = [\beta_1 \;\; \beta_2 \;\; \beta_3]^T$, and the random effects for each subject i are $b_i = [b_{1i} \;\; b_{2i} \;\; 0]^T$. We set one of the random effects to zero to reduce the number of random effects in the model. As we only have a maximum of three time points per subject, including an additional random effect may cause the matrix Ψ to be rank-deficient (singular) and thus create problems in the estimation of the parameters.

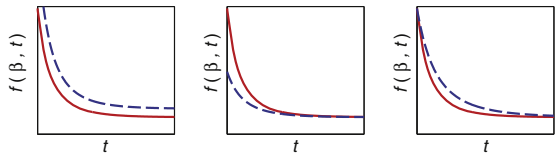

Fig. 3. Effect of varying the three parameters of the Gompertz function. The red curve shows the reference curve where parameters are held fixed. Left to right: the dashed blue curves show the effect of increasing values of β_1, β_2, and β_3 associated with asymptote, delay and speed, respectively.

Model estimation

Different methods have been proposed to estimate the parameters as shown in Eq. (4). Since random effects are unobserved quantities, we use the marginal density of responses y to obtain the parameters of the nonlinear mixed effects model. The following maximum likelihood estimation is performed to obtain the parameters of Eq. (4):

$$y_i : p\left(y_i|\beta, \Psi, \sigma^2\right) = \int p\left(y_i, |\beta, b_i, \Psi, \sigma^2\right) p(b_i) db_i. \tag{5}$$

Due to nonlinearity presented in the random effects of function f, there is generally no closed form solution to the integral. Here, we use the estimation method proposed by Lindstrom and Bates (1990) using the nlme package (Pinheiro et al., 2012) in R[3] to obtain the model parameters. This algorithm iterates between two steps: a penalized nonlinear least square step and a linear mixed effects step until convergence.

Inference and predictions

Under the linear mixed effects approximation, the distribution of maximum likelihood estimators $\hat{\beta}$ of the fixed effect is:

$$\hat{\beta} \sim N\left(\beta, \sigma^2 \left[\sum_{i=1}^{M} \hat{X} \Sigma_i^{-1} \hat{X}_i\right]^{-1}\right) \tag{6}$$

where $\Sigma_i = I + \hat{Z}_i \Delta^{-1} \Delta^{-T} \hat{Z}_i^T$, $\hat{X}_i = \frac{\partial f_i}{\partial \beta^T}\Big|_{\hat{\beta}, \hat{b}_i}$, $\hat{Z}_i = \frac{\partial f_i}{\partial b_i^T}\Big|_{\hat{\beta}, \hat{b}_i}$, and Δ is the precision factor such that $\Psi^{-1} = \sigma^{-2}\Delta^T\Delta$ (Pinheiro and Bates, 2000).

Knowing fixed parameters $\hat{\beta}$ and its sampling distribution, it is straightforward to conduct hypothesis testing among different regions or between healthy and/or at-risk populations. We can also obtain individual growth trajectories based on the estimated random effects for each individual. For example, the individual response for subject i is $\hat{y}_i = f(\beta + b_i, t)$, and the population growth trajectory is estimated when random effects are set to their mean value, 0, resulting in $\hat{y} = f(\beta, t)$.

Regional analysis of longitudinal data using NLME

We use the nonlinear mixed effects to model the longitudinal DTI data within anatomical regions and perform hypothesis testing between trajectories of these regions. Maps of these anatomical regions were developed and disseminated by Mori et al. (2008), and mapped to our unbiased atlas via linear followed by nonlinear B-spline registration (Rueckert et al., 1999). We select 13 anatomical regions in the atlas space as shown in Fig. 4. In this study, left and right regions of anatomical locations are combined, giving a total of

[3] http://r-project.org.

eight regions. Future studies on lateralization of growth differences will analyze left and right regions separately. The labeling of regions in the atlas space allows automatic partitioning of each subjects' scans into the different anatomical regions. We then estimate growth trajectories for these regions using the NLME model (Lindstrom and Bates, 1990) described previously. The mixed parameters are the asymptote ϕ_1, delay ϕ_2 and speed ϕ_3 of the Gompertz function for each region, which requires a slight modification to Eq. (4) to account for regions:

$$y_{rij} = f\left(\phi_{ri}, t_{ij}\right) + e_{ij} = \phi_{1ri} \exp\left\{-\phi_{2ri}\phi_{3ri}{}^{t_{ij}}\right\} + e_{ij}. \quad (7)$$

We then conduct hypothesis testing between pairs of regions to determine modes of longitudinal changes in terms of the Gompertz growth parameters. With N number of regions, we perform $\frac{N(N-1)}{2}$ pairwise fitting of nonlinear mixed effect modeling. The significant parameters are determined through t-tests, corrected for multiple comparisons by Bonferroni correction. The parameters that are found to be significant between two pairs of regions can be interpreted as the distinguishing feature between the longitudinal trajectories of these regions.

Results

We applied our framework to longitudinal pediatric DTI data of 26 subjects. In total, we selected 13 regions in the unbiased atlas as shown in Fig. 4. The regions are as follows: anterior limb of internal capsule (right and left; ALIC), posterior limb of internal capsule (right and left; PLIC), genu, body of corpus callosum (BCC), splenium (Sp), external capsule (right and left; ExCap), retrolenticular part of internal capsule (right and left; RLIC), and posterior thalamic radiation which includes optic radiation (right and left; PTR). The right and left of each anatomical region were combined giving a total of eight regions. Fig. 5 plots the average FA, MD, RD, and AD of each region for each subject. In all the regions, FA increases with age, whereas MD, RD and AD decrease with age. Interestingly, each region develops in a distinctly different temporal pattern.

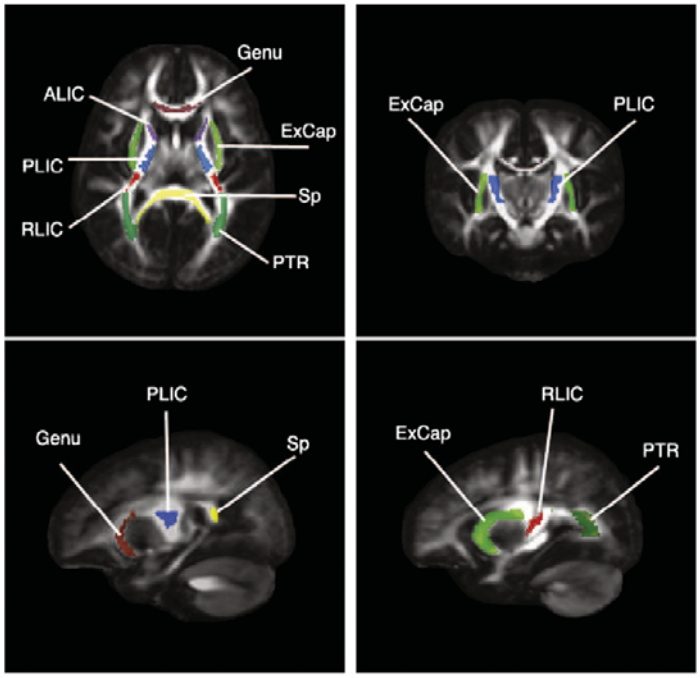

White matter anatomical structures	
Anterior limb of internal capsule	ALIC
Posterior limb of internal capsule	PLIC
Retrolenticular part of the internal capsule	RLIC
Posterior thalamic radiation	PTR
Genu of Corpus Callosum	Genu
Splenium of Corpus Callosum	Sp
Body of Corpus Callosum	BCC
External Capsule	ExCap

Fig. 4. White matter anatomical labels that are used for regional analysis. Labels are overlaid on the FA (Fractional Anisotropy) map of the reference space that is the population atlas.

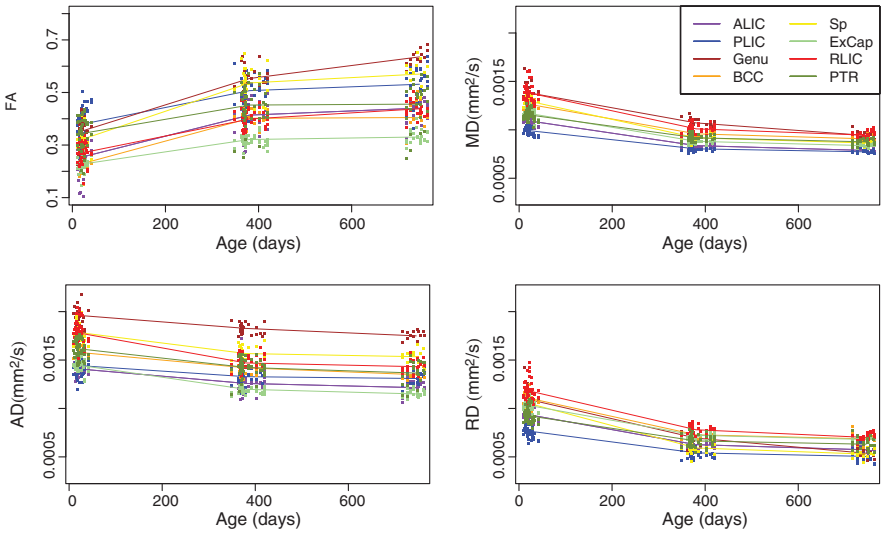

Fig. 5. Plots of diffusivity measures (FA, MD, AD and RD) versus age, shown for 26 control subjects and eight regions. Colors indicate different regions (purple: ALIC, light green: ExCap, brown: Genu, blue: PLIC, dark green: PTR, red: RLIC, yellow: Sp, orange: BCC), solid lines connect the mean of each region. In all the regions, FA increases with age, whereas MD, RD and AD decrease with age. Interestingly, each region develops in a distinctly different temporal pattern.

Paired t-tests of growth trajectories were performed for all combination of pairs of regions for all the diffusion parameters. The results of all pairwise comparisons can be found in Table 3 in Appendix B. Differences in parameters β_1 and β_2 were significant between most pairwise comparisons among diffusion parameters, whereas β_3 was only significant in a few regions: genu, splenium, and body of corpus callosum, and mostly when considering the RD or MD measurements. Genu was the only structure that was significantly different than all the other regions in the β_3 parameter of RD and MD. This region decreased in MD and RD at a slower rate compared to all the other regions. We didn't find any pattern that was consistent among different parameters and different measurements since each parameter measures a different aspect of growth. Interestingly, we noticed some pairwise comparisons with significant differences in β_1 parameter between AD and RD trajectories, but no differences in MD (ALIC vs. PLIC, Genu vs. ExCap). This happens when reverse temporal patterns are seen for AD and RD, suggesting that analysis of AD and RD may reveal much better insight into maturation than MD alone.

In this section, we focus on PLIC/ALIC, body of corpus callosum (BCC), and splenium comparisons as examples of commissural and projection fibers. These regions are known to have a distinctive maturation pattern and axonal density. The PLIC is one of the structures

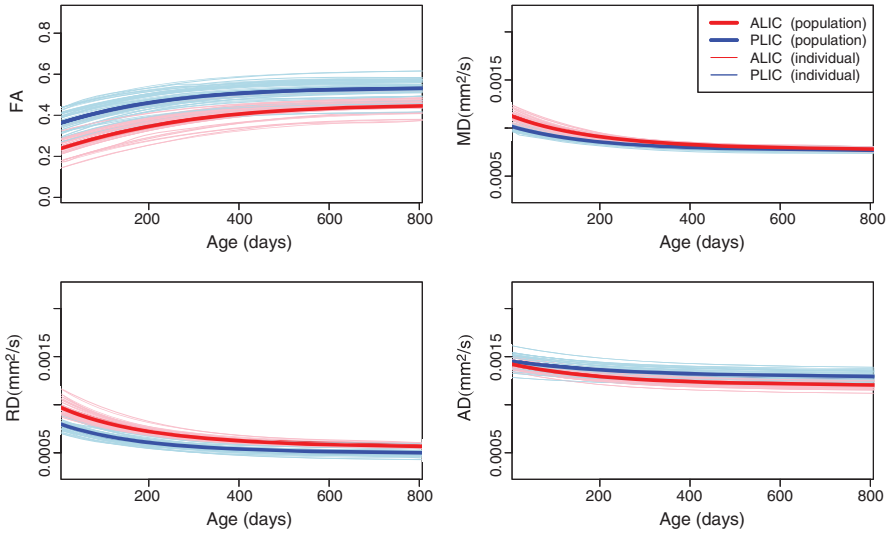

Fig. 6. Population and individual growth trajectories for PLIC and ALIC regions. Thicker curves illustrate the average growth trajectories, and individual trajectories are shown via the red and blue functions of individual subjects for ALIC and PLIC, respectively. Gompertz parameters with statistically significant differences are: FA: β_1^{**}, β_2^{**}, MD: β_2^{**}, RD: β_1^{**}, β_2^{**}, AD: β_1^{*}, where * denotes $p<0.05$, ** denotes $p<0.01$ and where β_1, β_2 and β_3 represent asymptote, delay and speed.

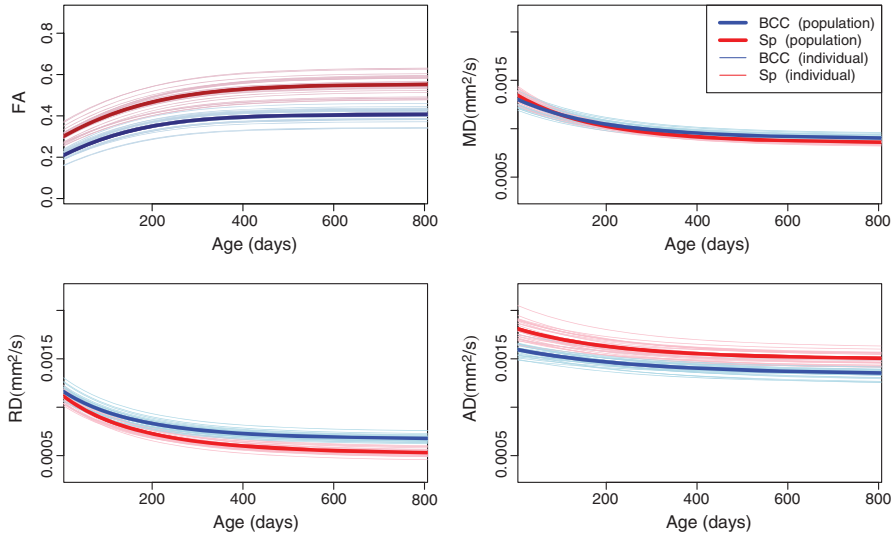

Fig. 7. Population and individual growth trajectories for the body of the corpus callosum (BCC, blue) and the splenium (Sp, red). Thick curves are the average growth trajectories. Gompertz parameters with significant differences are: FA: β_1^{**}, β_2^{**}, MD: β_2^{**}, RD: β_1^{**}, β_2^{**}, AD: β_1^{*}, where * denotes $p<0.05$, ** denotes $p<0.01$ and where β_1, β_2 and β_3 represent asymptote, delay and speed, respectively.

that shows early myelination, while ALIC shows later maturation compared to PLIC as is shown in higher FA, and lower RD and MD. Fig. 6 shows the population and individual trajectories of FA, MD, RD and AD as modeled by Nonlinear Mixed Effect for ALIC/PLIC. As expected, the PLIC shows a higher FA compared to ALIC at birth mainly explained by lower RD. After about 800 days both regions have the same MD and similar FA and RD values. However, the ALIC shows a higher AD compared to PLIC, possibly indicating a different structuring of this tract region. The delay parameter of the Gompertz function β_2 was significantly different between ALIC and PLIC for FA, MD, and RD measurements, an indication of later development of ALIC compared to PLIC. Also, the asymptote β_1 was significantly different for FA, RD and AD.

The body of the corpus callosum (BCC) and splenium (Sp) are known to have very limited myelination at birth but higher axonal density compared to ALIC and PLIC, and the splenium shows earlier myelination compared to BCC (Rutherford, 2002). Fig. 7 shows population and individual growth trajectories for the body of the corpus callosum and splenium. The splenium shows higher FA at birth and also throughout the first two years, while RD is about same at birth, but diverges at two years. Reverse patterns are seen for AD and RD at about two years, which causes MD to be about the same. All three parameters of the Gompertz function for RD were significantly different between BCC and Splenium, suggesting that RD may capture early maturation patterns more sensitively than the other measures. The asymptote parameter was significantly different among all the measurements between these two regions.

Fig. 8 shows FA, RD and AD of PLIC (shown in blue) compared to the other three regions ALIC, BCC, and Sp (shown in red). In this figure, solid lines are the average estimated growth trajectories for each region, the shaded regions are the 95% confidence interval of these average curves. Monte Carlo simulation was used to generate 1000 curves based on the approximate distribution of the maximum likelihood estimates of fixed effects. The 95% range of these curves are calculated pointwise to obtain the confidence interval. The dashed lines show the 95% predicted interval which is also calculated based on the Monte Carlo simulation of 1000 curves based on the approximate distribution of both fixed effects and random effects.

The splenium shows a high RD at birth relative to PLIC, by about 800 days however, both regions have approximately the same RD value as shown in Fig. 8. The splenium has very limited myelination at birth, while the PLIC is known to have a higher level of myelination at this time of development. These facts are evident in the difference in RD at birth between splenium and PLIC. At age two, however, the splenium shows approximately the same RD value, indicating that it catches up with PLIC.

The values of Gompertz parameters for all the regions and all diffusivity measures are shown in Fig. 9. Each region shows a distinct pattern of development as is depicted by the β_1, β_2, and β_3 parameters of Gompertz function. As indicated in the section 'Model formulation' the parameters β_1, β_2, and β_3 represent asymptote, delay and speed, respectively. When $\beta_1 : R_A > R_B$, the expected value of diffusion parameters for region A is higher than region B at year 2. When $\beta_2 : |R_A| > |R_B|$, region R_B matures earlier compared to R_A. The scenario $\beta_3 : R_A > R_B$ indicates accelerated growth for R_B compared to R_A. Note that the delay parameter is negative for RD, AD and MD measurements as these values decrease during early brain development, where as the delay parameter is positive for FA as fractional anisotropy increases during this time period.

Discussion

Assessment of brain growth patterns in these regions reveals a nonlinear pattern of maturation with considerable regional variation as shown in previous studies (Hermoye et al., 2006; Mukherjee et al., 2001; Schneider et al., 2004). In agreement with previous studies, increased FA and decreased MD, AD, RD were observed within all the white matter regions during this period (Forbes et al., 2002; Mukherjee et al., 2001; Schneider et al., 2004; Zhang et al., 2005). This longitudinal pediatric study supports a rapid change during the first 12 month followed by slower maturation during the second year similar to previous studies (Geng et al., 2012; Hermoye et al., 2006). Our study, in addition to supporting earlier cross-sectional reports on negative correlation between age and diffusion parameters, provides greater statistical power to examine nonlinear pattern of maturation in various white matter regions.

Beyond the analysis of FA and MD measurements, in this study we included RD and AD analysis of these white matter regions. The regional comparisons of white matter regions indicates that

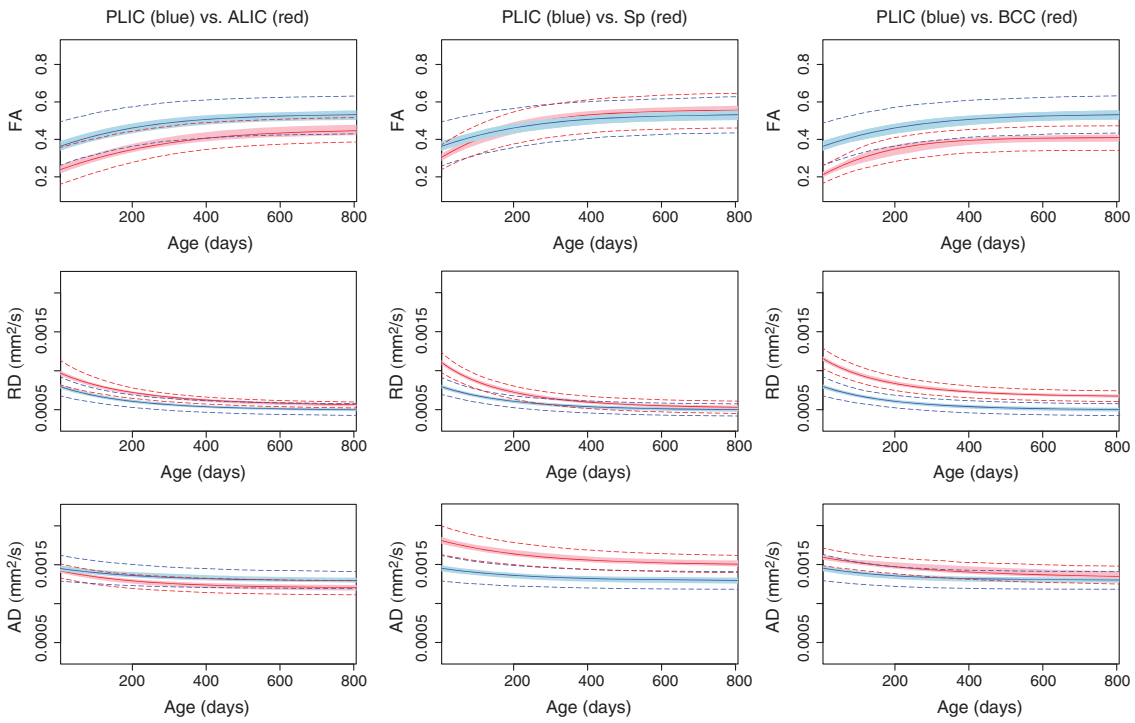

Fig. 8. PLIC (blue) compared to three other regions. Left column: ALIC (red), middle column splenium (red) and right column BCC (red). Solid curves are the estimated growth trajectories, the 95% confidence interval of the curves are shown as shaded regions. The dashed lines show the 95% predicted intervals for each region. Gompertz parameters with statistically significant differences are the following: ALIC vs. PLIC: FA: β_1^{**}, β_2^{**}, RD: β_1^{**}, β_2^{**}, AD: β_1^{*}. PLIC vs. Sp: FA: β_2^{**}, RD: β_2^{*}, AD: β_1^{**}, β_2^{*}. PLIC vs. BCC: FA: β_1^{**}, β_2^{**}, RD: β_1^{*}, where * denotes $p<0.05$, ** denotes $p<0.01$, and β_1, β_2 and β_3 represent asymptote, delay and speed, respectively.

individual AD and RD carry important information which may not be found in the MD diffusivity measures. The relationship of AD/RD and FA is complex and nonlinear, but our data suggest that modeling FA, AD, RD as time trajectories provides more information than only FA as illustrated in Figs. 6 and 7.

For example, FA of splenium and PLIC are approximately the same values at birth, yet we know that the splenium is not myelinated at birth, and we see the significant differences of RD between these regions. The high FA value of the splenium at birth may be due to its high density of axons. This discussion of FA for PLIC and splenium clearly reflects that FA is not necessarily a good indicator for the degree of myelination and may be greatly influenced by axonal density particular to this developmental interval (LaMantia and Rakic, 1990). In contrast, the similarity of FA trajectories for PLIC and splenium, for which we see very different AD and RD patterns and thus different tensor shapes, illustrates that interpretation of FA with respect to myelination and structural integrity is difficult, and that the additional AD and RD measures provide richer information.

Modeling the nonlinear growth changes of white matter by the Gompertz function and inclusion of AD and RD to the analysis provides a more detailed and comprehensive picture of the changes within these white matter regions. Compared to previous studies of linear fitting with logarithm of age (Chen et al., 2011; Faria et al., 2010; Lobel et al., 2009) we fit the nonlinear growth curves (Gompertz function) to the diffusion data and actual age, this enables the parameterization of the trajectories in terms of asymptote, delay and speed and models nonlinear temporal changes with improved accuracy. Based on our finding, the delay parameter of the Gompertz function, β_2 of RD seems to be closest related to myelination process if we compare results to what is known from the literature. Looking at RD and β_2 delay parameter of the Gompertz function as is shown in Fig. 9, we see a good correspondence with previous radiology findings, such as in Rutherford (2002). In fact, RD has been considered to be in correspondence with histological changes in demyelination (Song et al., 2002). Table 2 compares our findings versus existing knowledge from radiology literature, which indicates development of PLIC prior to ALIC, and splenium prior to genu which is also consistent with previous histological findings (Brody et al., 1987; Kinney et al., 1988).

Our framework is designed not only to provide qualitative comparisons, but to give researchers and clinicians quantitative parameters and a statistical testing scheme. Moreover, the method includes modeling of growth trajectories of individuals, resulting in personalized profiles. This property will be crucial for efforts to improve prediction and diagnosis for individuals, as well as partitioning groups of subjects according to subtypes and subtle variations in early developmental trajectories. Models which assume invariance or linearity between neurobehavioral markers are apt to miss crucial shifts in development (Shaw et al., 2006; Thomas et al., 2009). The ability of the present framework to capture the dynamic properties of inter- and intra-individual development has the potential to substantially improve clinical applications of developmental neuroimaging.

There are some limitations to our proposed framework. Our analysis depends on accurate image registration among all the subjects and time points. Early brain development is characterized by a rapid change of contrast and size of the brain, which makes registration a challenging task. However, in this study we decided to use ROI defined regions

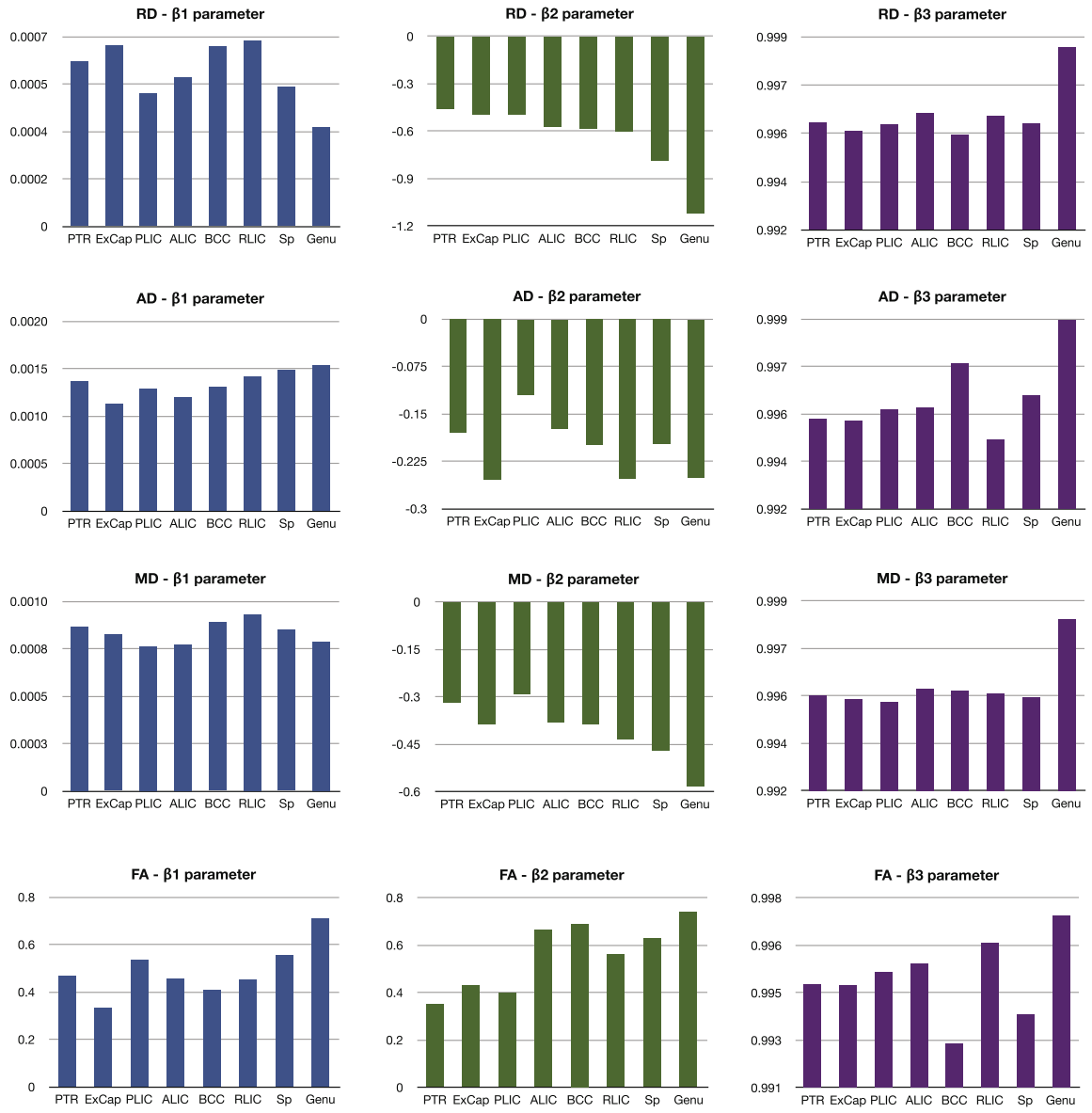

Fig. 9. Gompertz parameters RD, AD, MD and FA, from top to bottom. Left to right: β_1 is the asymptote parameter of the Gompertz function (blue), β_2 is the delay parameter (green), and β_3 is related to the speed (purple). The delay parameter is negative for RD, AD, and RD as the estimated model represents a decreasing Gompertz function, whereas the FA delay parameters are positive since FA values increase during development. When $\beta_1 : R_A > R_B$, the expected value of diffusion parameters for region A is higher than region B at year 2. When $\beta_2 : |R_A| > |R_B|$, region R_B matures earlier compared to R_A. $\beta_3 : R_A > R_B$ indicates accelerated growth for R_B compared to R_A.

Table 2
Relative order of appearance of myelin from term to 2 years.

Distribution of myelin as seen in T1W and T2W by Rutherforld	Estimated based on RD delay parameter β_2
PLIC and optic radiation	PLIC, PTR and ExCap
ALIC	ALIC and BCC
Not available	RLIC
Splenium	Splenium
Genu	Genu

which we expect to be more robust to misregistration compared to voxel-based analysis, and these regions are located more interiorly where we expect less registration problems. Nonetheless, improved spatial registration will potentially improve the accuracy of the model. Another limitation is that the statistical analysis is based on the log-likelihood of nonlinear mixed effects modeling, which does not have a closed form solution. We have used a linear mixed effect approximation, so greater care should be taken when doing hypothesis testing with the estimated parameters.

In the future, we plan to extend our method to tract-based regions with modeling along the tract changes. We also plan to extend the model to multivariate growth function similar to (Xu et al., 2008) and include a much larger set of regions for analysis.

Conclusions

We have presented a framework for the processing of longitudinal images in order to characterize longitudinal development of white matter regions at both the individual and group level. By utilizing nonlinear mixed effects modeling, we jointly estimate the population trajectory along with each individual trajectories. Gompertz parameterization of diffusion changes provides an intuitive parameterization of growth trajectory in terms of asymptote, delay and speed. This provides a description of longitudinal changes with potential for detecting deviations from a typical growth trajectory sensitive to multiple neurodevelopmental phenomena. We have also presented a method for making inference about regional differences in diffusion properties known to vary by microstructural properties and developmental course (Dubois et al., 2008; Kinney et al., 1988; LaMantia and Rakic, 1990; Lebel and Beaulieu, 2011). This is in contrast to standard modeling and analysis of testing for group or regional differences as it reveals the type, timing, and nature of differences. The proposed analysis can be extended to an arbitrary number of regions, and applied to other measurement such as structural MRI.

As discussed in the previous section, the present study clearly illustrate that studying FA alone as an indicator of white matter maturation or integrity insufficiently characterizes structural properties of white matter and may produce misleading results as regions with very different axonal density and differing degrees of myelination may show similar FA values. We suggest that in addition to FA, studies should include statistical analysis of AD and RD, which provide important additional information to better explain FA measures. In regard to early maturation, we demonstrate that the radial diffusivity (RD) measure and the delay parameter β_2 of the Gompertz function seem to be the best combination to describe early brain maturation. We will further explore this in applying our framework to DTI of infants with developmental delay and myelination storage disorders such as Krabbe's disease.

Acknowledgments

Supported by NIH grants: R01 MH070890 (JHG, GG), Conte Center MH064065 (JHG, GG), National Alliance for Medical Image Computing (NA-MIC) U54 EB005149 (GG) and the Utah Science Technology and Research (USTAR) initiative at the University of Utah.

Appendix A. Summary of registration parameters

Intra-subject and inter-modality registration

We use the IRTK software (Rueckert et al., 1999) to perform intra-subject and inter-modality registration. The registration method is a multi-scale approach using B-spline transformation, where we use the normalized mutual information image match metric. We use three different scales and discretize the image intensity histograms into 64 bins. In this study, the B-spline transforms are parametrized using $14\times14\times14$ control points.

Inter-subject registration

We construct an unbiased atlas (Joshi et al., 2004) and the associated inter-subject registration using the Large Deformation Diffeomorphic Metric Mapping (LDDMM) (Miller et al., 2002) that minimizes the following objective function:

$$\underset{v:\phi_t=v_t(\phi)}{\arg\min}\frac{1}{\sigma^2}\sum_i\left\|\bar{I}-I_i\circ\phi_i^{-1}\right\|_{L^2}^2+\sum_i\int_{t=0}^{T}\|v_{it}\|_v^2 \tag{8}$$

where $\bar{I}$ is the image atlas, I_i is the image of subject i, ϕ_i is the mapping relating subject i to the atlas that is parametrized using the velocity v_i. Regularity of the mapping ϕ is enforced by minimizing

$$\|v_t\|_v^2=\langle Lv,v\rangle, L=\alpha\nabla^2+\beta\nabla+\gamma I \tag{9}$$

Table 3
Results of pairwise testing of all white matter regions and all diffusivity measures. Gompertz parameters with significant differences are denoted by * for $p<.05$ and ** for $p<.01$. Non significant parameters are indicated by "ns".

		Alic	Plic	Genu	BCC	Sp	ExCap	Rlic	PTR
Alic	FA		β_1^{**}, β_2^{**}	β_1^{**}	β_1^{**}	β_1^{**}	β_1^{**}	ns	β_2^{**}
	MD	NA	β_2^{**}	β_2^{**}, β_3^{**}	β_1^{**}	β_1^{**}, β_2^{**}	β_1^{**}	β_1^{**}, β_2^{*}	β_1^{**}, β_2^{**}
	RD		β_1^{**}, β_2^{**}	β_1^{**}, β_2^{**}, β_3^{**}	β_1^{**}	β_2^{**}	β_1^{**}, β_2^{**}	β_1^{**}	β_1^{*}, β_2^{**}
	AD		β_1^{*}	ns	ns	β_1^{**}	β_1^{**}, β_2^{**}	β_1^{**}, β_2^{**}	β_1^{**}
Plic	FA	β_1^{**}, β_2^{**}		β_1^{**}, β_2^{**}	β_1^{**}, β_2^{**}	β_2^{**}	β_1^{**}	β_1^{*}, β_2^{*}	ns
	MD	β_2^{**}	NA	β_2^{**}, β_3^{**}	β_1^{**}, β_2^{**}	β_1^{**}, β_2^{**}	β_1^{**}, β_2^{**}	β_1^{**}, β_2^{**}	β_1^{**}
	RD	β_1^{**}, β_2^{**}		β_1^{*}, β_2^{**}, β_3^{**}	β_1^{*}	β_2^{*},	β_1^{*}	β_1^{**}, β_2^{**}	β_1^{**}
	AD	β_1^{*}		β_1^{**}, β_3^{**}	ns	β_1^{**}, β_2^{*}	β_1^{**}, β_2^{**}	β_1^{**}, β_2^{**}	ns
Genu	FA	β_1^{**}	β_1^{**}, β_2^{**}		β_1^{**},	β_1^{**}, β_3^{**}	β_1^{**}, β_2^{**}	β_1^{**}, β_2^{**}	β_1^{**}, β_2^{**}
	MD	β_2^{**}, β_3^{**}	β_2^{**}, β_3^{**}	NA	β_1^{**}, β_2^{**}	β_3^{**}	β_2^{**}, β_3^{**}	β_3^{**}	β_2^{**}, β_3^{**}
	RD	β_1^{**}, β_2^{**}, β_3^{**}	β_1^{**}, β_2^{**}, β_3^{**}		β_1^{*}, β_2^{**}, β_3^{**}	β_3^{**}	β_1^{**}, β_2^{**}, β_3^{**}	β_1^{**}, β_3^{**}	β_1^{**}, β_3^{**}
	AD	ns	β_1^{**}, β_3^{**}		ns	β_1^{**}	β_1^{**}, β_2^{**}, β_3^{**}	β_3^{**}	ns
BCC	FA	β_1^{**}	β_1^{**}, β_2^{**}	β_1^{**}		β_1^{**}	β_1^{**}, β_2^{**}	β_2^{*}	β_2^{**}
	MD	β_1^{**}	β_1^{**}, β_2^{**}	β_2^{**}, β_3^{**}	NA	β_1^{**}, β_2^{**}	β_1^{**}	ns	β_2^{**}
	RD	β_1^{**}	β_1^{*}	β_1^{**}, β_2^{**}, β_3^{**}		β_1^{**}, β_2^{**}, β_3^{**}	β_1^{*}	β_1^{**}, β_2^{**}, β_3^{**}	β_1^{**}, β_3^{**}
	AD	ns	ns	ns		β_1^{**}	β_1^{*}, β_2^{**}	ns	ns
Sp	FA	β_1^{**}	β_2^{**}	β_1^{**}, β_3^{**}	β_1^{**}		β_1^{**}, β_2^{**}	β_1^{**}	β_1^{*}, β_2^{**}
	MD	β_1^{**}, β_2^{**}	β_1^{**}, β_2^{**}	β_3^{**}	β_1^{**}, β_2^{**}	NA	β_1^{*}, β_2^{**}	β_1^{*}	β_2^{**}
	RD	β_2^{**}	β_2^{*}	β_3^{**}	β_1^{**}, β_2^{**}, β_3^{**}		β_1^{**}, β_2^{**}	β_1^{**}, β_2^{**}	β_1^{**}, β_2^{**}
	AD	β_1^{**}	β_1^{**}, β_2^{**}	β_1^{**}	β_1^{**}		β_1^{**}, β_2^{**}	ns	ns
ExCap	FA	β_1^{**}	β_1^{**}	β_1^{**}, β_2^{**}	β_1^{**}, β_2^{**}	β_1^{**}, β_2^{**}		β_1^{**}	β_1^{**}
	MD	β_1^{**}	β_1^{**}, β_2^{**}	β_2^{**}, β_3^{**}	β_1^{**}	β_1^{*}, β_2^{**}	NA	β_1^{**}	β_1^{*}, β_2^{**}
	RD	β_1^{**}, β_2^{**}	β_1^{**}	β_1^{**}, β_2^{**}, β_3^{**}	β_1^{**}	β_1^{**}, β_2^{**}		β_2^{**}	β_1^{**}
	AD	β_1^{**}, β_2^{**}	β_1^{**}, β_2^{**}	β_3^{**}	β_1^{**}, β_2^{**}	β_1^{**}, β_2^{**}		β_1^{*}	β_1^{**}, β_2^{**}
Rlic	FA	ns	β_1^{*}, β_2^{*}	β_1^{**}, β_2^{**}	β_2^{*}	β_1^{**}	β_1^{**}		β_2^{**}
	MD	β_1^{**}, β_2^{**}	β_1^{**}, β_2^{**}	β_3^{**}	ns	β_1^{*}	β_1^{**}	NA	β_1^{**}, β_2^{***}
	RD	β_1^{**}	β_1^{**}, β_2^{*}	β_1^{**}, β_3^{**}	β_1^{**}, β_2^{**}, β_3^{**}	β_1^{**}, β_2^{**}	β_2^{**}		β_1^{**}, β_2^{**}
	AD	β_1^{**}, β_2^{**}	β_1^{**}, β_2^{**}	β_3^{**}	ns	ns	β_1^{**}		β_2^{**}

Table 3 (*continued*)

		Alic	Plic	Genu	BCC	Sp	ExCap	Rlic	PTR
PTR	FA	β_2^{**}	ns	β_1^{**}, β_2^{*}	β_2^{**}	β_1^{*}, β_2^{**}	β_1^{**}	β_2^{**}	
	MD	β_2^{**}, β_3^{**}	β_1^{**}	β_1^{**}, β_2^{**}	β_2^{**}	β_2^{**}	β_1^{**}, β_2^{**}	β_1^{**}, β_2^{**}	NA
	RD	β_1^{**}, β_2^{**}	β_1^{**}	β_1^{**}, β_3^{**}	β_1^{**}, β_3^{**}	β_1^{**}, β_2^{**}	β_1^{**}	β_1^{**}, β_2^{**}	
	AD	β_1^{**}	ns	ns	ns	ns	β_1^{**}, β_2^{**}	β_2^{**}	β_2^{**}

where L is the Navier–Stokes operator. In this study, we use $\alpha = .01$, $\beta = .01$, $\gamma = .001$, and $\sigma = 1$.

Appendix B. Summary of *p*-values of pairwise comparisons

Table 3 provides the result of pairwise testing of all white matter regions and all the diffusivity measurements.

References

Alexander, D., Pierpaoli, C., Basser, P., Gee, J., Nov 2001. Spatial transformations of diffusion tensor magnetic resonance images. IEEE Trans. Med. Imaging 20 (11), 1131–1139.

Als, H., Duffy, F., McAnulty, G., Rivkin, M., Vajapeyam, S., Mulkern, R., Warfield, S., Huppi, P., Butler, S., Conneman, N., Fischer, C., Eichenwald, E., Apr 2004. Early experience alters brain function and structure. Pediatrics 113 (4), 846–857.

Arsigny, V., Commowick, O., Pennec, X., Ayache, N., 2006. A log-Euclidean framework for statistics on diffeomorphisms. Med Image Comput Comput Assist Interv 9 (Pt 1), 924–931.

Brody, B., HC, K., AS, K., HG, F., 1987. Sequence of central nervous system myelination in human infancy. I. An autopsy study of myelination. J. Neuropathol. Exp. Neurol. 46 (3), 283–301 (May).

Casey, B.J., Tottenham, N., Liston, C., Durston, S., 2005. Imaging the developing brain: what have we learned about cognitive development? Trends Cogn. Sci. (Regul. Ed.) 9 (3), 104–110 (Mar).

Chen, Y., An, H., Zhu, H., Jewells, V., Armao, D., Shen, D., Gilmore, J.H., Lin, W., Oct 2011. Longitudinal regression analysis of spatial–temporal growth patterns of geometrical diffusion measures in early postnatal brain development with diffusion tensor imaging. NeuroImage 58 (4), 993–1005.

Diggle, P., Heagerty, P., Liang, K., Zeger, S., 2002. Analysis of Longitudinal Data, second edition. Edition. Oxford University Press, New York.

Dubois, J., Hertz-Pannier, L., Dehaene-Lambertz, G., Cointepas, Y., Le Bihan, D., May 2006. Assessment of the early organization and maturation of infants' cerebral white matter fiber bundles: a feasibility study using quantitative diffusion tensor imaging and tractography. NeuroImage 30, 1121–1132.

Dubois, J., Dehaene-Lambertz, G., Perrin, M., Mangin, J., Cointepas, Y., Duchesnay, E., Le Bihan, D., Hertz-Pannier, L., Jan 2008. Asynchrony of the early maturation of white matter bundles in healthy infants: quantitative landmarks revealed noninvasively by diffusion tensor imaging. Hum. Brain Mapp. 29, 14–27.

Faria, A., Zhang, J., Oishi, K., Li, X., Jiang, H., Akhter, K., Hermoye, L., Lee, S.K., Hoon, A., Stashinko, E., Miller, M.I., van Zijl, P.C., Mori, S., Aug 2010. Atlas-based analysis of neurodevelopment from infancy to adulthood using diffusion tensor imaging and applications for automated abnormality detection. NeuroImage 52, 415–428.

Fletcher, P., Joshi, S., 2007. Riemannian geometry for the statistical analysis of diffusion tensor data. Signal Process. 87 (2), 250–262.

Forbes, K.P., Pipe, J.G., Bird, C.R., Feb 2002. Changes in brain water diffusion during the 1st year of life. Radiology 222 (2), 405–409.

Gao, W., Lin, W., Chen, Y., Gerig, G., Smith, J., Jewells, V., Gilmore, J., Feb 2009. Temporal and spatial development of axonal maturation and myelination of white matter in the developing brain. AJNR Am. J. Neuroradiol. 30 (2), 290–296.

Geng, X., Gouttard, S., Sharma, A., Gu, H., Styner, M., Lin, W., Gerig, G., Gilmore, J.H., July 2012. Quantitative tract-based white matter development from birth to age 2 years. NeuroImage 61, 542–557.

Giedd, J.N., Blumenthal, J., Jeffries, N.O., Castellanos, F.X., Liu, H., Zijdenbos, A., Paus, T., Evans, A.C., Rapoport, J.L., Oct 1999. Brain development during childhood and adolescence: a longitudinal MRI study. Nat. Neurosci. 2 (10), 861–863.

Gilmore, J., Kang, C., Evans, D., Wolfe, H., Smith, J., Lieberman, J., Lin, W., Hamer, R., Styner, M., Gerig, G., Sep 2010. Prenatal and neonatal brain structure and white matter maturation in children at high risk for schizophrenia. Am. J. Psychiatry 167 (9), 1083–1091.

Gogtay, N., Giedd, J.N., Lusk, L., Hayashi, K.M., Greenstein, D., Vaituzis, A.C., Nugent, T.F., Herman, D.H., Clasen, L.S., Toga, A.W., Rapoport, J.L., Thompson, P.M., May 2004. Dynamic mapping of human cortical development during childhood through early adulthood. Proc. Natl. Acad. Sci. U. S. A. 101 (21), 8174–8179.

Hermoye, L., Saint-Martin, C., Cosnard, G., Lee, S.K., Kim, J., Nassogne, M.C., Menten, R., Clapuyt, P., Donohue, P.K., Hua, K., Wakana, S., Jiang, H., van Zijl, P.C., Mori, S., Jan 2006. Pediatric diffusion tensor imaging: normal database and observation of the white matter maturation in early childhood. NeuroImage 29 (2), 493–504.

Huppi, P., Oct 2008. Neuroimaging of brain development—discovering the origins of neuropsychiatric disorders? Pediatr. Res. 64, 325.

Huppi, P., Maier, S., Peled, S., Zientara, G., Barnes, P., Jolesz, F., Volpe, J.J., Oct 1998. Microstructural development of human newborn cerebral white matter assessed in vivo by diffusion tensor magnetic resonance imaging. Pediatr. Res. 44 (4), 584–590.

Joshi, S., Davis, B., Jomier, M., Gerig, G., 2004. Unbiased diffeomorphic atlas construction for computational anatomy. NeuroImage 23, S151–S160.

Karmiloff-Smith, A., Jun 2010. Neuroimaging of the developing brain: taking "developing" seriously. Hum. Brain Mapp. 31 (6), 934–941.

Kinney, H., Brody, B., Kloman, A., Gilles, F., May 1988. Sequence of central nervous system myelination in human infancy. II. Patterns of myelination in autopsied infants. J. Neuropathol. Exp. Neurol. 47 (3), 217–234.

Knickmeyer, R., Gouttard, S., Kang, C., Evans, D., Wilber, K., Smith, J., Hamer, R., Lin, W., Gerig, G., Gilmore, J., Nov 2008. A structural MRI study of human brain development from birth to 2 years. J. Neurosci. 28, 12176–12182.

LaMantia, A., Rakic, P., Jul 1990. Axon overproduction and elimination in the corpus callosum of the developing rhesus monkey. J. Neurosci. 10 (7), 2156–2175.

Lebel, C., Beaulieu, C., Jul 2011. Longitudinal development of human brain wiring continues from childhood into adulthood. J. Neurosci. 31 (30), 10937–10947.

Lindstrom, M., Bates, D., Sep 1990. Nonlinear mixed effects models for repeated measures data. Biometrics 46, 673–687.

Lobel, U., Sedlacik, J., Gullmar, D., Kaiser, W.A., Reichenbach, J.R., Mentzel, H.J., Apr 2009. Diffusion tensor imaging: the normal evolution of ADC, RA, FA, and eigenvalues studied in multiple anatomical regions of the brain. Neuroradiology 51 (4), 253–263.

Marsh, R., Gerber, A., Peterson, B., Nov 2008. Neuroimaging studies of normal brain development and their relevance for understanding childhood neuropsychiatric disorders. J. Am. Acad. Child Adolesc. Psychiatry 47 (11), 1233–1251.

Ment, L., Hirtz, D., Huppi, P., Nov 2009. Imaging biomarkers of outcome in the developing preterm brain. Lancet Neurol. 8 (11), 1042–1055.

Miller, M., Trouve, A., Younes, L., 2002. On the metrics and Euler–Lagrange equations of computational anatomy. Annu. Rev. Biomed. Eng. 4, 375–405.

Mori, S., Oishi, K., Jiang, H., Jiang, L., Li, X., Akhter, K., Hua, K., Faria, A., Mahmood, A., Woods, R., Toga, A., Pike, G., Neto, P., Evans, A., Zhang, J., Huang, H., Miller, M., van Zijl, P., Mazziotta, J., Apr 2008. Stereotaxic white matter atlas based on diffusion tensor imaging in an ICBM template. NeuroImage 40, 570–582.

Mukherjee, P., Miller, J., Shimony, J., Conturo, T., Lee, B., Almli, C., McKinstry, R., Nov 2001. Normal brain maturation during childhood: developmental trends characterized with diffusion-tensor MR imaging. Radiology 221 (2), 349–358.

Mukherjee, P., Miller, J., Shimony, J., Philip, J., Nehra, D., Snyder, A., Conturo, T., Neil, J., McKinstry, R., Oct 2002. Diffusion-tensor MR imaging of gray and white matter development during normal human brain maturation. AJNR Am. J. Neuroradiol. 23 (9), 1445–1456.

Neil, J., Shiran, S., McKinstry, R., Schefft, G., Snyder, A., Almli, C., Akbudak, E., Aronovitz, J., Miller, J., Lee, B., Conturo, T., Oct 1998. Normal brain in human newborns: apparent diffusion coefficient and diffusion anisotropy measured by using diffusion tensor MR imaging. Radiology 209 (1), 57–66.

Pennec, X., Fillard, P., Ayache, N., January 2006. A Riemannian framework for tensor computing. Int. J. Comput. Vis. 66 (1), 41–66.

Pinheiro, J., Bates, D., 2000. Mixed-Effects Models in S and S-Plus. Springer.

Pinheiro, J., Bates, D., DebRoy, S., Sarkar, D., R Core Team, 2012. nlme: linear and nonlinear mixed effects models. R package version 31–104.

Rueckert, D., Sonoda, L., Hayes, C., Hill, D., Leach, M., Hawkes, D., Aug 1999. Nonrigid registration using free-form deformations: application to breast MR images. IEEE Trans. Med. Imaging 18 (8), 712–721.

Rutherford, M. (Ed.), 2002. MRI of the Neonatal Brain. WB Saunders.

Sadeghi, N., Prastawa, M., Gilmore, J., Lin, W., Gerig, G., 2010. Spatio-temporal analysis of early brain development. Proceedings IEEE Asilomar Conference on Signals, Systems and Computers, pp. 777–781.

Sadeghi, N., Prastawa, M., Fletcher, P., Gilmore, J., Lin, W., Gerig, G., 2012. Statistical growth modeling of longitudinal DT-MRI for regional characterization of early brain development. Proceedings of IEEE ISBI, pp. 1507–1510.

Salvador, R., Pena, A., Menon, D., Carpenter, T., Pickard, J., Bullmore, E., Feb 2005. Formal characterization and extension of the linearized diffusion tensor model. Hum. Brain Mapp. 24 (2), 144–155.

Schneider, J.F., Il'yasov, K.A., Hennig, J., Martin, E., Apr 2004. Fast quantitative diffusion-tensor imaging of cerebral white matter from the neonatal period to adolescence. Neuroradiology 46 (4), 258–266.

Shaw, P., Greenstein, D., Lerch, J., Clasen, L., Lenroot, R., Gogtay, N., Evans, A., Rapoport, J., Giedd, J., Mar 2006. Intellectual ability and cortical development in children and adolescents. Nature 440 (7084), 676–679.

Smith, S.M., 2002. Fast robust automated brain extraction. Hum. Brain Mapp. 17 (3), 143–155 (Nov).

Song, S., Sun, S., Ramsbottom, M., Chang, C., Russell, J., Cross, A., Nov 2002. Dysmyelination revealed through MRI as increased radial (but unchanged axial) diffusion of water. NeuroImage 17 (3), 1429–1436.

Studholme, C., Hill, D., Hawkes, D., et al., 1999. An overlap invariant entropy measure of 3D medical image alignment. Pattern Recogn. 32 (1), 71–86.

Thomas, M., Annaz, D., Ansari, D., Scerif, G., Jarrold, C., Karmiloff-Smith, A., Apr 2009. Using developmental trajectories to understand developmental disorders. J. Speech Lang. Hear. Res. 52 (2), 336–358.

Wolff, J., Gu, H., Gerig, G., Elison, J., Styner, M., Gouttard, S., Botteron, K., Dager, S., Dawson, G., Estes, A., Evans, A., Hazlett, H., Kostopoulos, P., McKinstry, R.C., Paterson, S., Schultz,

R., Zwaigenbaum, L., Piven, J., 2012. Differences in white matter fiber tract development present from 6 to 24 months in infants with autism. Am. J. Psychiatry (Feb).
Xu, S., Styner, M., Gilmore, J., Gerig, G., 2008. Multivariate nonlinear mixed model to analyze longitudinal image data: MRI study of early brain development. MMBIA: IEEE Comp Soc, pp. 1–8 (June).
Xue, H., Srinivasan, L., Jiang, S., Rutherford, M., Edwards, A., Rueckert, D., Hajnal, J.V., 2007. Automatic cortical segmentation in the developing brain. IPMI, pp. 257–269.
Zhang, L., Thomas, K.M., Davidson, M.C., Casey, B.J., Heier, L.A., Ulug, A.M., 2005. MR quantitation of volume and diffusion changes in the developing brain. AJNR Am. J. Neuroradiol. 26 (1), 45–49 (Jan).

CHAPTER 4

PEDIATRIC LONGITUDINAL AUTISM STUDY

4.1 Introduction

Autism spectrum disorders (ASDs) are disorders of neurodevelopment typically characterized by repetitive behavior and social deficit. ASDs are usually diagnosed when the child is around 2 to 3 years old. The occurrence of ASDs in the general population is about 1 in 110 children, with higher rates among boys than girls [27]. The risk increases substantially for at risk families, with an occurrence of one in five [28]. The Infant Brain Imaging Study (IBIS) is designed to increase the understanding of early brain development in children with ASDs by recruiting and conducting MRI scans of younger siblings of children with autism [29]. As these children are at increased risk of autism, about 20% will be diagnosed with autism at later ages. Therefore, by studying these children from an early age (6 months), we gain valuable insight about the disorder that might shed some light on when and how deviation from the normative path occurs. The hope is that if there are earlier signs of the disorder, we can predict who among high risk individuals will eventually develop autism. This can lead to earlier intervention and the hope for a better outcome.

This study included subjects from an Autism Center of Excellence at four clinical sites (University of North Carolina, Chapel Hill; University of Washington, Seattle; Childrens Hospital of Philadelphia; and Washington University, St. Louis). Subjects were recruited and scanned at 6 months with follow-up assessment and scans at 12 and 24 months. The study was approved by the institutional review board at each site.

4.2 DTI Analysis

4.2.1 Subjects

Fifty high risk subjects were selected for this study who had scans at 6, 12, and 24 months and behavioral assessments at age 24 months. Symptoms of ASDs were measured

at 24 months by using the Autism Diagnostic Observation Schedule [30]. At 24 months, 13 of the high risk infants met the criteria for ASDs (HR+) and 37 did not (HR–).

4.2.2 Image Acquisition and Processing

MRI brain scans of children were acquired at multiple clinical sites on 3T Siemens Trio scanners. To ensure a maximal success rate of scanning, all subjects were fed, swaddled, and fitted with ear protection. All subjects were scanned without sedation during their natural sleep. An echo planar imaging (ep2d_diff) pulse sequence was used for diffusion tensor imaging with the following parameters: TR = 12800–13300 ms, TE = 102 ms, variable b values of 0 to 1000 s/mm^2, 25 gradient directions, and scan time of 5–6 minutes. The voxel resolution was $2 \times 2 \times 2$ mm^3. All diffusion weighted images (DWIs) were checked and corrected for motion and eddy current artifacts by using DTIprep software [31]. Motion between baseline scans is removed by rigidly registering all baseline scans and averaging them together. This averaged baseline image is used for subsequent motion and eddy current corrections. Diffusion weighted images are registered rigidly to the baseline image to correct for head motion artifacts. To correct for eddy currents, DWIs are registered via affine transformation to the baseline image.

To study changes of diffusion parameters of subjects, we map all the individual scans to a common template. First, the DTI baseline (B0) images are registered to a T2W atlas via the nonlinear registration method of Rueckert *et al.* [32] using normalized mutual information as the image match metric. This is followed by the unbiased atlas building framework of Joshi *et al.* [33] based on the Large Deformation Diffeomorphic Metric Mapping (LDDMM) [34] applied to the curvature FA images of all the available scans. The result is an atlas along with a set of invertible transformations between all the subjects and the atlas. The tensors are registered to the atlas using transformations obtained from atlas building procedures. Tensors are resampled using finite strain reorientation and Riemannian interpolation [35, 36, 37]. After all the images are transformed into the atlas space, the tensors are averaged using the log-Euclidean method to produce a tensor atlas [38].

4.2.3 Regional Analysis

In the first analysis, we used regions of interests defined by tractography methods by our collaborators at the University of North Carolina [29]. We had label maps for the following fiber tracts available: fornix, inferior longitudinal fasciculus, and anterior thalamic radiation. These fiber tracts were extracted from the same atlas and as such, we were able to use them. For each fiber tract, fractional anisotropy (FA), mean diffusivity (MD), radial

(RD), and axial diffusivity (AD) measures were generated.

We also used white matter label maps of anatomical regions of interests that were developed and disseminated by Mori *et al.* [39]. The white matter label map was registered to our unbiased atlas via linear followed by nonlinear B-spline registration [32]. The labeling of regions in the atlas space allows automatic partitioning of each subject's scans into different anatomical regions as all the subjects are registered to the atlas as described in section 4.2.2. For each region, FA, RD, and AD values were calculated.

We attempted to model longitudinal trajectories of mean FA, RD, and AD for regions of interests for HR– and HR+ by using the nonlinear mixed effect modeling of Chapter 2. However, the models failed to converge for all the regions defined by white matter label maps and worked for only the right inferior longitudinal fasiculus, which was defined by tractography. Initially, the Gompertz curve with asymptote and delay as random effects was used to model the growth trajectories. Subsequent tries with few random effects (i.e., only using asymptote as random effects) also failed. A closer look at the raw data indicated high levels of noise in the DTI data. Fig. 4.1 shows the mean FA value for the left inferior longitudinal fasiculus; however, as is shown, not all the FA values display an increasing trend that is expected during this age range [40]. This is the case for both high risk infants who did get diagnosed with the disorder and those who did not, so we do not believe this is a characteristic of the disorder.

Also, upon more detailed analysis of raw images, we noticed a vibration artifact. This source of artifact is due to a patient table vibration and has recently been reported in other studies [41]. This vibration is simulated by the low frequency gradient switching associated with the diffusion weighting [41]. The resulting effect on the image shows as a signal loss when there is a strong component of the diffusion gradient vector in the left-right direction. As a result, the colored FA images have a more than normal reddish color as shown in Fig. 4.2. This artifact is also referred to as the red artifact, as the areas affected by the artifact will have high FA values in the left-right direction (red color denotes the left-right diffusion in colored FA images).

4.3 T1-Weighted Analysis

4.3.1 Image Acquisition and Processing

In addition to the DTI data, T1W images were also obtained for each subject. MP-Rage was used to obtain 3D T1W images on Siemens scanners with the following parameters: TR: 2400 ms, TE 3.16 ms. The voxel resolution was $1 \times 1 \times 1$. All the available data underwent the following steps by our collaborators at the Montreal Neurological Institute: 1) bias

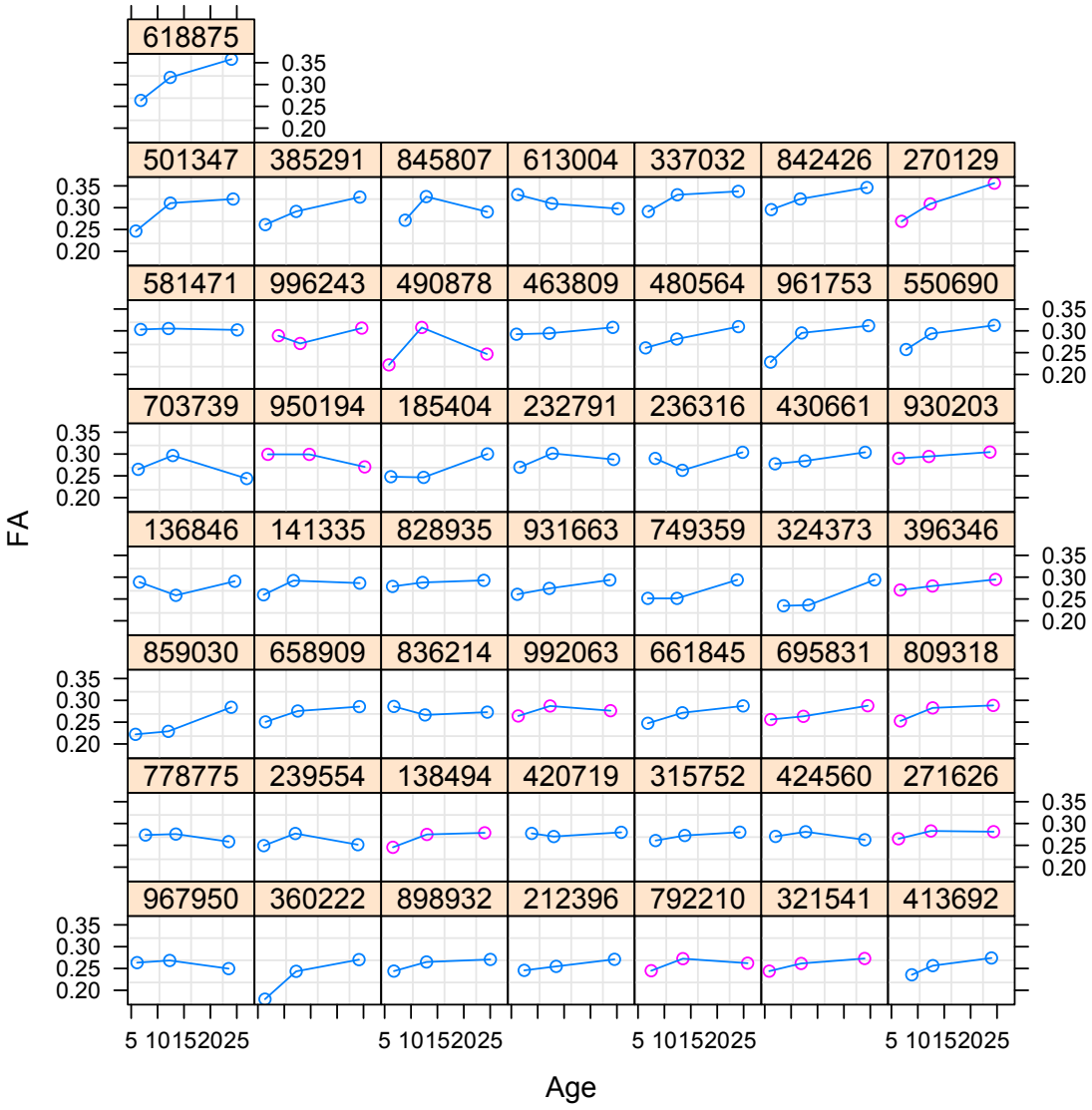

Figure 4.1: Mean FA values for the left inferior longitudinal fasiculus. Blue circles: HR–, Purple circles: HR+. The data do not show a consistent increasing trend as is expected during this age range, most probably due to the large noise level of this special infant DTI pulse sequence and also some residual scanner vibration artifacts.

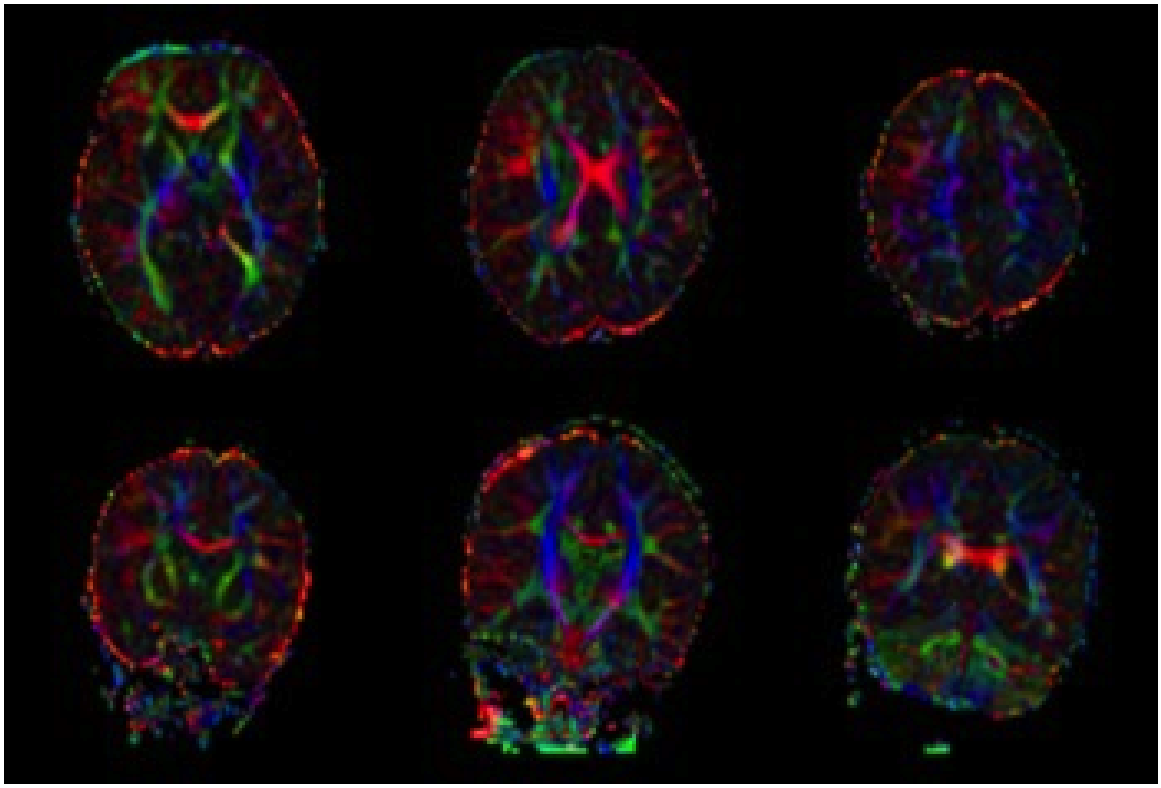

Figure 4.2: Axial and coronal cross-section of a colored FA of subject's scan at 1 year demonstrating vibration artifacts.

correction using the method of Sled, Zijdenbos, and Evans [42] and 2) rigid registration to stereotaxic space.

Eighty-eight subjects (HR–: 69, HR+: 19) who had available data at 6, 12, or 24 months and behavioral assessments at age 24 months were selected for this study. In total, 198 scans were available for these subjects: 51 scans at 6 months, 88 scans at 1 year, and 59 scans at 2 years. The distribution of the data is shown in Table 4.1.

Unbiased atlas building was used to build a template atlas of all the year 1 T1W scans [33]. All time points of each subject are registered to the unbiased atlas via linear and nonlinear transformations [32], first by mapping these images to the year 1 scan and then cascading the two transformations for a mapping to the atlas. Once all the images are in a common reference space, we remove the variations in the intensity ranges of images via intensity normalization. Scans were normalized using a high intensity value of a fatty tissue region between the skull and the skin.

Similar to previous studies in this dissertation, white matter label maps [39] were registered to our unbiased atlas via linear and nonlinear B-spline registration [32] to define

Table 4.1: Distribution of Scans Across Different Time Points for High Risk Infants.

	6 months	1 year	2 year	Total
HR–	42	69	45	156
HR+	9	19	14	42
Total	51	88	59	198

anatomical regions of interest.

4.3.2 Statistical Analysis of White Matter Regions

We used the framework proposed in Chapter 2 to estimate the longitudinal trajectories for mean T1W values of selected regions of interest (ROIs) and compare them between HR– and HR+. Fig. 4.3 shows the trajectories of T1W for anterior, superior, and posterior corona radiata. Low p-values were observed for posterior corona radiata; however, after multiple comparison corrections, none of the regions were significant between the two groups. Overall, we analyzed 21 regions, and resulting p-values from a comparison of HR– and HR+ are shown in Table 4.2. Higher intensity values were observed for HR+ for all the regions considered. Even though none of the regions showed a significant difference between the two groups, the average trajectory for HR+ was consistently higher than HR–. We were surprised by this finding, as autism spectrum disorder is hypothesized by an early brain overgrowth, followed by slower growth rate after years 2–5 [43].

We performed a second study in which we compared healthy controls (LR–) and HR+ (Table 4.3). We found a pattern similar to that for the comparison of HR+ to HR–. Fig. 4.4 shows the longitudinal trajectories of T1W for anterior, superior, and posterior corona radiata for LR– and HR+. The observed patterns of HR– and LR– are very similar, as shown in Fig. 4.5. Again, HR+ consistently showed a higher average trajectory compared to LR– and HR–, but no significant differences were found between LR– and HR+. The results of group testing between growth trajectories of LR– and HR+ are shown in Table 4.4.

4.4 Discussion

In this chapter, we compared growth trajectories of infants at high risk of autism spectrum disorder and healthy controls in DTI and T1W scans. Our attempts to model the growth trajectories as represented in the DTI were unsuccessful. We believe this is mainly due to noisy data and still insufficient correction for subject motion and scanner related artifacts. Rigorous measures have been taken as this is a multisite study. However, it

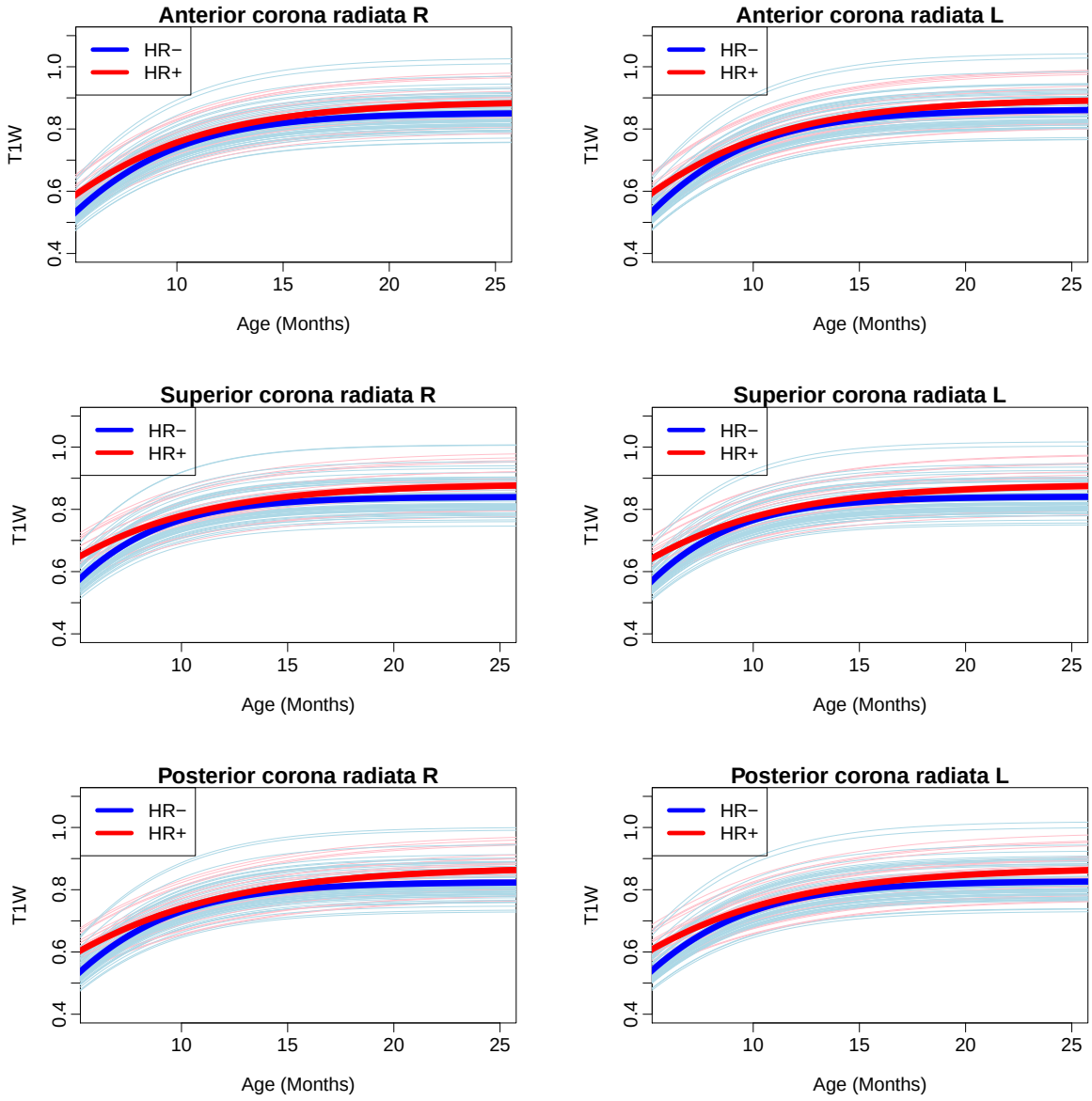

Figure 4.3: Group differences in T1W of white matter regions in 88 infants with (HR+) and without (HR–) diagnosis of autism spectrum disorder. The thicker lines are the average trajectories whereas the thin lines are the individual trajectories.

Table 4.2: Group Differences in Gompertz Parameters of T1W of White Matter Regions Between HR– and HR+.

WM Label	Asymptote		Delay		Speed	
	Raw p	p*	Raw p	p*	Raw p	p*
Genu of corpus callosum	0.171	0.197	0.145	0.169	0.191	0.201
Body of corpus callosum	0.088	0.181	0.087	0.140	0.116	0.171
Splenium of corpus callosum	0.083	0.181	0.066	0.140	0.070	0.171
Anterior limb of internal capsule R	0.147	0.181	0.153	0.169	0.146	0.171
Anterior limb of internal capsule L	0.147	0.181	0.145	0.169	0.112	0.171
Posterior limb of internal capsule R	0.102	0.181	0.247	0.247	0.122	0.171
Posterior limb of internal capsule L	0.130	0.181	0.225	0.237	0.112	0.171
Retrolenticular part of internal capsule R	0.078	0.181	0.071	0.140	0.064	0.171
Retrolenticular part of internal capsule L	0.111	0.181	0.079	0.140	0.095	0.171
Anterior corona radiata R	0.178	0.197	0.152	0.169	0.257	0.257
Anterior corona radiata L	0.207	0.207	0.093	0.140	0.177	0.196
Superior corona radiata R	0.116	0.181	0.077	0.140	0.114	0.171
Superior corona radiata L	0.139	0.181	0.068	0.140	0.104	0.171
Posterior corona radiata R	0.079	0.181	0.032	0.140	0.048	0.171
Posterior corona radiata L	0.121	0.181	0.045	0.140	0.090	0.171
Posterior thalamic radiation R	0.144	0.181	0.041	0.140	0.055	0.171
Posterior thalamic radiation L	0.084	0.181	0.054	0.140	0.061	0.171
External capsule R	0.128	0.181	0.105	0.147	0.138	0.171
External capsule L	0.113	0.181	0.081	0.140	0.134	0.171
Superior longitudinal fasciculus R	0.139	0.181	0.047	0.140	0.075	0.171
Superior longitudinal fasciculus L	0.191	0.201	0.081	0.140	0.142	0.171

*Based on the false discovery rate adjustment for multiple comparisons introduced by Benjamini and Hochberg (BH) [44]. Note that it is possible for the adjusted p-values to have the same value. BH FDR p-value adjustment is defined as $Q_{adj}^{BH}(p_i) = \min_{i \leq k}\{p_k.\frac{m}{k}\}$ where $i = 1, \ldots, m$ and $k = i, \ldots, m$ ordered p-values [45].

Table 4.3: Distribution of Scans Across Different Time Points for Healthy Controls (LR–) and High Risk Infants Diagnosed with Autism Spectrum Disorder (HR+).

	6 months	1 year	2 year	Total
LR–	19	23	7	49
HR+	9	19	14	42
Total	28	42	21	91

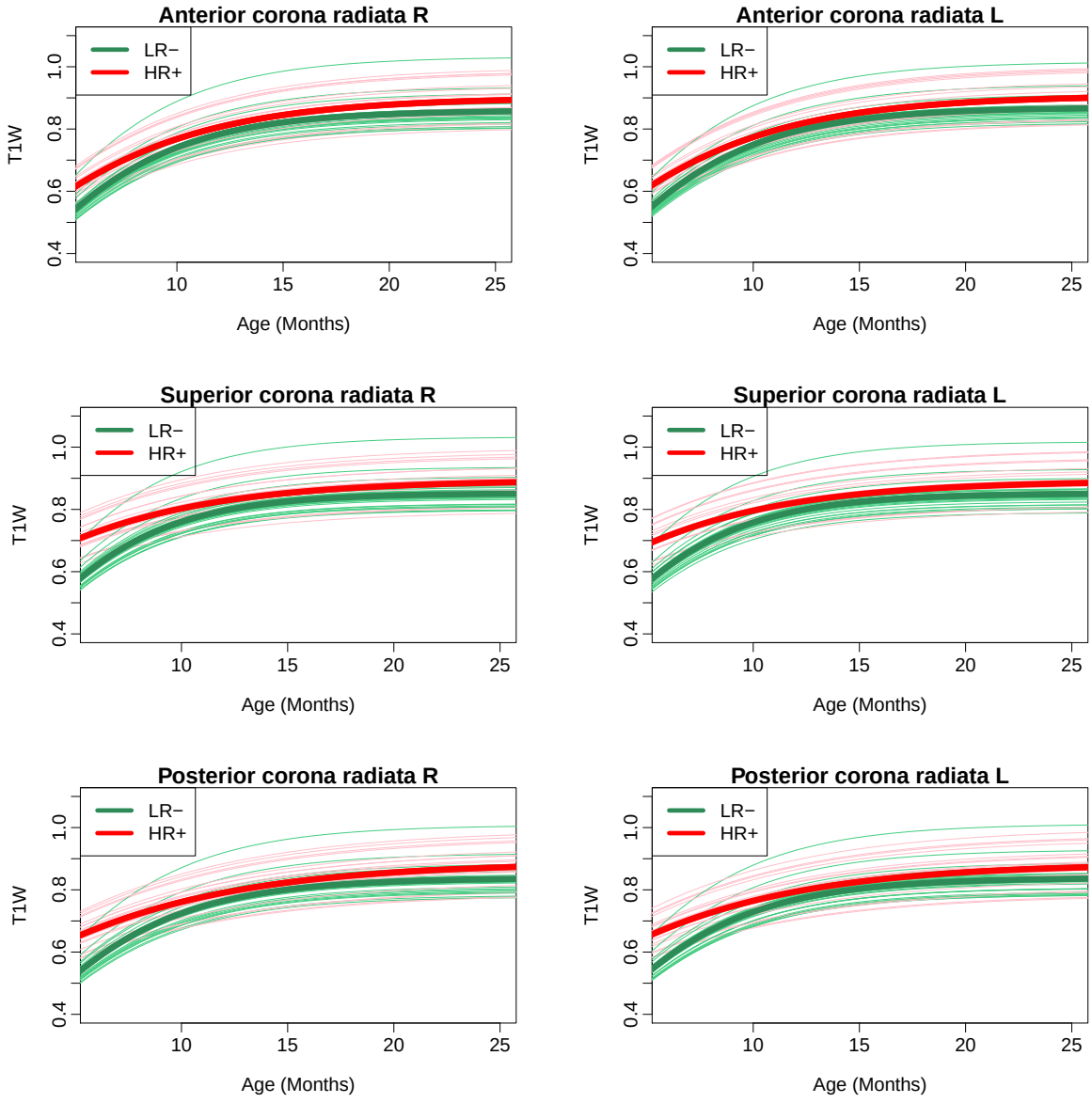

Figure 4.4: Group differences in T1W of white matter regions in 88 infants with diagnosis for autism spectrum disorder (HR+) and healthy controls (LR–). The thicker lines are the average trajectories whereas the thin lines are the individual trajectories.

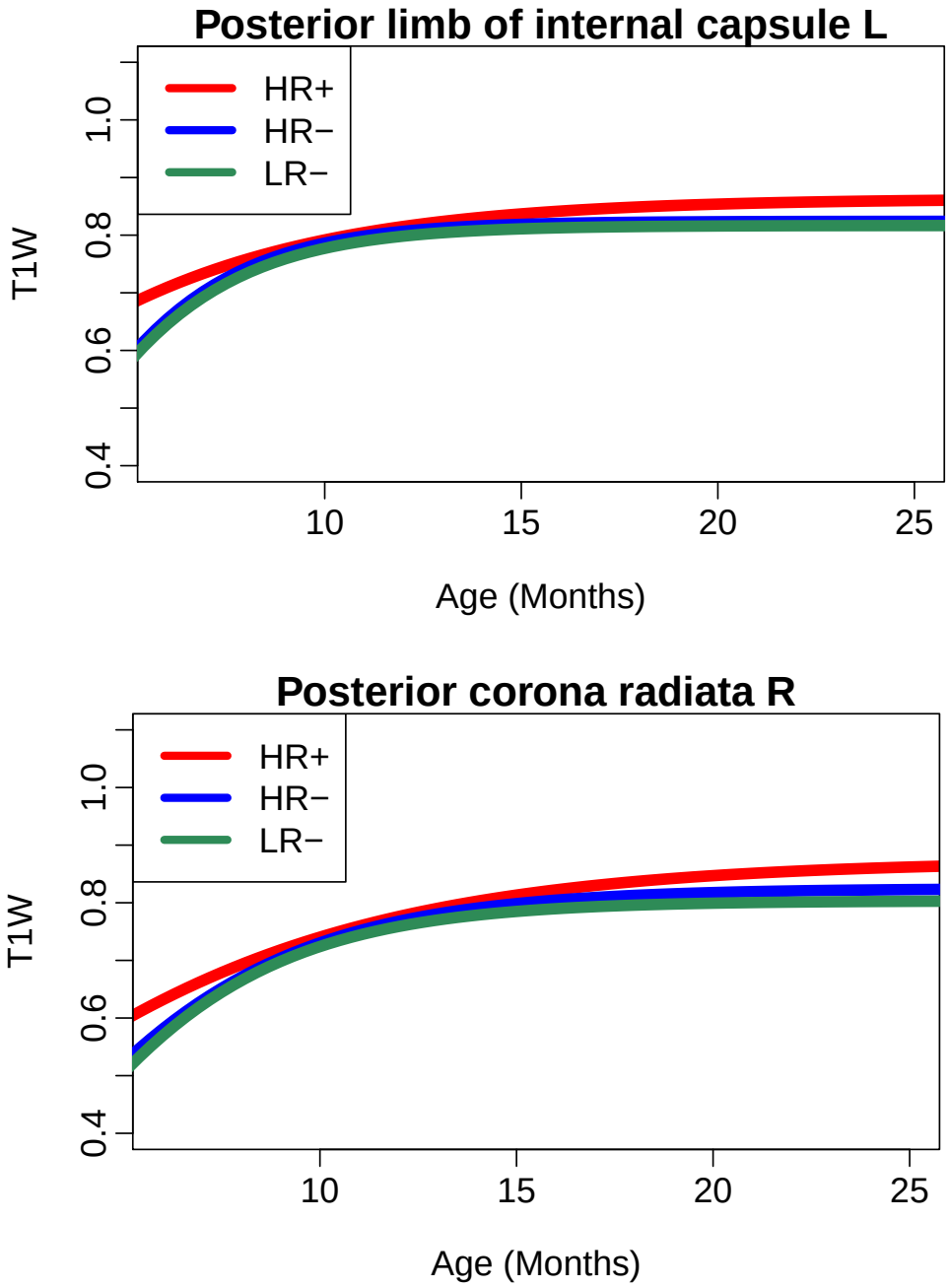

Figure 4.5: Trajectories of T1W of the posterior limb of the internal capsule and the posterior corona radiate for infants with (HR+) and without (HR–) diagnosis of autism spectrum disorder and healthy controls (LR–). HR+ displays higher values of T1W during this age range, whereas the developmental trajectories of HR– and LR– are very similar.

Table 4.4: Group Differences in Gompertz Parameters of Longitudinal Trajectories of T1W for White Matter Regions Between LR– and HR+.

WM Label	Asymptote		Delay		Speed	
	Raw p	p*	Raw p	p*	Raw p	p*
Genu of corpus callosum	0.166	0.166	0.424	0.511	0.416	0.416
Body of corpus callosum	0.079	0.166	0.370	0.511	0.301	0.368
Splenium of corpus callosum	0.073	0.166	0.417	0.511	0.286	0.368
Anterior limb of internal capsule R	0.135	0.166	0.462	0.511	0.329	0.368
Anterior limb of internal capsule L	0.130	0.166	0.447	0.511	0.314	0.368
Posterior limb of internal capsule R	0.165	0.166	0.531	0.531	0.344	0.368
Posterior limb of internal capsule L	0.158	0.166	0.519	0.531	0.326	0.368
Retrolenticular part of internal capsule R	0.112	0.166	0.414	0.511	0.257	0.368
Retrolenticular part of	0.098	0.166	0.400	0.511	0.259	0.368
Anterior corona radiata R	0.121	0.166	0.348	0.511	0.345	0.368
Anterior corona radiata L	0.137	0.166	0.347	0.511	0.351	0.368
Superior corona radiata R	0.092	0.166	0.367	0.511	0.245	0.368
Superior corona radiata L	0.094	0.166	0.349	0.511	0.240	0.368
Posterior corona radiata R	0.062	0.166	0.278	0.511	0.163	0.368
Posterior corona radiata L	0.080	0.166	0.288	0.511	0.183	0.368
Posterior thalamic radiation R	0.101	0.166	0.379	0.511	0.211	0.368
Posterior thalamic radiation L	0.089	0.166	0.349	0.511	0.213	0.368
External capsule R	0.098	0.166	0.371	0.511	0.260	0.368
External capsule L	0.058	0.166	0.359	0.511	0.250	0.368
Superior longitudinal fasciculus R	0.142	0.166	0.320	0.511	0.253	0.368
Superior longitudinal fasciculus L	0.136	0.166	0.354	0.511	0.289	0.368

*Based on the false discovery rate adjustment for multiple comparisons

appears that the data still contain artifacts despite correcting for motion and eddy current. A new source of artifacts was discovered that has not been corrected yet, the vibration artifact. As was shown earlier, this artifact manifests itself as a signal loss and would be interpreted as higher diffusion in the left-right direction. Due to the high level of artifacts, we were not able to apply our framework to the DTI data of the autism study. The clinical sites are aware of the problem and have taken measures to reduce the vibration. For phase II of this project, a newly developed high angular resolution sequence (HARDI) with significantly improved image quality was added. In the future, we can try to exclude the subjects with high levels of artifacts or possibly apply the newly proposed method of [41] as it does not require modifying the acquisition sequence.

In the second part of this study, we analyzed the T1W scans. As expected for this age range, the T1W intensity values increased in all the white matter regions that we analyzed. We performed two sets of experiments: 1) comparison of high risk infants who were diagnosed with autism versus those who did not and 2) comparison of high risk infants who were diagnosed with autism versus healthy control. Healthy controls were the subjects who were not at high risk of autism and did not get diagnosed with autism during the course of the study. Overall, we did not find any regions that showed significant differences in the parameters of the Gompertz function; however, we observed that average T1W trajectories were consistently higher compared to controls and high risk infants who did not get diagnosed with autism. LR– and HR– had nearly indistinguishable growth profiles. We were surprised by the results as most developmental disorders show a decrease in myelination, which most likely will appear as a decrease in observed T1W scans. However, it has been suggested that there is a period of rapid growth during the early years in autism spectrum disorders [43]. The observed increase values in T1W could be due to overgrowth early on. We are not aware of any study on intensity values of T1W for subjects at risk of autism; however, recently there has been increased emphasis on studying infants at risk of autism through the use of DTI. Bashet *et al.* [46] observed increased FA and decreased diffusivity in white matter. Wolff *et al.* [29] reported increased FA values at 6 months for high risk infants diagnosed with autism compared to high risk infants who were not diagnosed; however, the pattern was reversed at 24 months when HR– had higher FA values compared to HR+. Other studies have shown that the FA values are still higher compared to normal control at 4 years of age [46]. There are few studies comparing intensity values of T1W scans between groups; however, our preliminary analysis demonstrates that studying T1W images can provide additional insight into early brain development.

CHAPTER 5

TWIN STUDY

5.1 Introduction

Twin studies have contributed substantially to our understanding of the heritability of many neuropsychiatric and neurodevelopment disorders [47]. Comparing identical (monozygotic twins, MZ) and fraternal (dizygotic, DZ) twins allows researchers to estimate contributions of heritability and environment to individual differences. Monozygotic twins share the same genetic material whereas dizygotic twins share on average about 50% of their genes [48]. Therefore, if a trait is heritable, we expect a higher correlation in MZ compared to DZ assuming twins of the same parents share a common environment. Twin studies have provided a valuable insight into the heritability of disease; however, it might be difficult to generalize these findings to a singleton population due to differences between twins and singletons in pre- and postnatal environments [49, 50]. The intrauterine environment might be suboptimal as twins share the womb and compete for nutrition. Also, the family environment can be suboptimal due to limited resources and competition between the twins [51].

Some studies have suggested the nongeneralizability of twin studies to singletons as they have found differences in cognitive measures [51, 52]. However, more recent studies have found no differences in IQ between twins and the singleton population, suggesting that findings in twin studies can be generalized to singletons [53]. It is not known whether twin studies provide reliable estimates of heritabilities of integrity of white matter. A recent study by Knickmeyer *et al.* found significant differences in gray matter development in MZ twins compared to DZ twins and singletons, but no difference was found in intracranial volume, total white matter volume, and lateral ventricle volume [49]. In this study, we examine the compatibility of white matter developmental trajectories between twins and singletons.

5.2 Materials and Methods

5.2.1 Subjects

Mothers were recruited during their second trimester of pregnancy from clinics at the University of North Carolina for a longitudinal twin study. In total, 26 singletons and 76 twins who had DTI scans were used for this study. Infants were scanned at about 2 weeks, 1 year, and 2 years without sedation during natural sleep. Not all the subjects had all three scans available. The distribution of scans along with information about zygocity is shown in Table 5.1. This study was approved by the Institutional Review Board of the University of North Carolina School of Medicine.

5.2.2 Image Acquisition and Data Processing

All images were acquired using a 3T Allegra head-only MR system using a single shot echo-planar spin echo diffusion tensor imaging sequence with the following parameters: TR = 5200 ms, TE = 73 ms, a slice thickness of 2 mm, and in-plane resolution of 2×2 mm^2. One image without diffusion gradients (b = 0) along with six gradient directions with a b-value of 1000 mm^3/s were acquired. The sequence was repeated five times for an improved signal-to-noise ratio. All DWIs were checked and corrected for motion artifacts using the DTIChecker tool.[1] Tensor maps were calculated for each DTI scan using a weighted least squares tensor estimation on the images that have been averaged over sequence repeats [54]. T2-weighted structural images were obtained using a turbo spin echo sequence with TR = 7 s, TE = 15 and 90 ms, a slice thickness of 1.95 mm, and in-plane resolution of 1.25×1.25 mm^2. T2W and baseline DWI of all the subjects' scans were skull stripped using the Brain Extraction Tool (BET) [55].

Image registration and processing was done in a similar fashion as described in section 3.2.2. Unbiased atlas building was used to provide a mapping between individuals to the template atlas [33]. The atlas was built from the population of data in the study as the average template. All individuals' scans were first mapped to their year 1 T2W scan via the linear and nonlinear registration method of Rueckert *et al.* [32] and subsequently to the atlas via deformation maps obtained during the atlas building procedure. The tensors are registered to the atlas using transformations obtained by registering the DTI baseline (B0) images to T2W images. Tensor maps were calculated using the weighted least-squares estimation method and transferred to the atlas using finite strain reorientation and Riemannian interpolation [35, 36, 37]. In this study, the axial diffusivity (AD), radial

[1] http://www.ia.unc.edu/dev/download/dtichecker

Table 5.1: Distribution of Scans Across Different Time Points and Zygocity.

	Neonate	1 year	2 year	Total
Singletons	23	22	14	59
Dizygotic	34	39	20	93
Monozygotic	35	36	15	86
Total	92	97	49	238

diffusivity (RD), and fractional anisotropy (FA) features are extracted from the registered tensors.

5.2.3 Statistical Analysis

The nonlinear mixed effects modeling of Chapter 2 is used to estimate trajectories of development as is shown in DTI within anatomical regions of interest. The Gompertz growth curve was used to model the mean trajectory. Longitudinal trajectories of mean FA, MD, RD, and AD were compared among monozygotic, dizygotic, and singletons. Among the 102 subjects included in the analysis, 92 had scans at neonate, 97 had scans at 1 year, and 49 had scans at 2 years. The white matter label map that was developed and disseminated by [39] was used to define anatomical regions of interest. This label map was mapped to the template atlas via linear followed by nonlinear b-spline registration [32]. The labeling of regions in the atlas space allows automatic partitioning of each subject's scans into the different anatomical regions.

5.3 Results

Comparison of mean trajectories among monozygotic, dizygotic, and singletons indicated that growth trajectories of monozygotic and dizygotic twins are very similar. No significant differences were found between the growth curves of MZ and DZ in terms of Gompertz parameters of asymptote, delay, and speed for any of the diffusion measurements. To further investigate whether twins and singletons show any developmental differences, DZ and MZ individuals were combined as there were no differences in their growth trajectories. Gestational age was controlled in the analysis as twin subjects are generally born earlier than singletons. In this study, twins were born about 25 days earlier than singletons on average. To ensure that the observed differences between MZ and DZ are not due to age, gestation age at the time of the MRI scan was taken into account rather than age. Table 5.2 shows the gestational age at birth and at the time of the first MRI scan for twins and singletons.

When comparing the combined twin group to singletons, the following regions showed

Table 5.2: Gestational Age of Singletons and Twins.

	Singletons	Twins
Gestational Age at Birth (days); Mean (SD)	272.43 (14.09)	247.07 (17.74)
Gestational Age at the First MRI (days); Mean (SD)	300.56 (28.67)	290.79 (20.56)

significant differences in the delay parameter of the axial diffusivity measures: right and left anterior limb of the internal capsule and right and left anterior corona radiate. There were no significant differences in asymptote and speed parameters between these two groups for any of the regions analyzed. There were also no significant differences between FA and RD measures between these two groups. In the regions in which the delay parameter was significant, AD reached the same level as singletons by the first 3 months, as though twin subjects "catch up" to singletons relatively shortly after birth. The changes from birth to 2 years in the axial diffusivity for the anterior limb of the internal capsule and the anterior corona radiata are shown in Fig. 5.1; the changes in delay parameter were significantly different in the two groups. However, most of the regions analyzed showed no significant differences between twins and singletons. AD trajectories for the posterior limb of the internal capsule that showed no difference between the twins and singletons are presented in Fig. 5.2.

5.4 Discussion

These preliminary findings suggest that twins and singletons follow similar growth trajectories for the majority of white matter regions. This study compared 21 anatomical regions, including projection fibers such as internal capsule and corona radiata, association fibers including superior longitudinal fasciculus and external capsule, and commissural fibers such as genu, body, and splenium of corpus callosum. Fractional anisotropy and radial diffusivity did not differ between twins and singletons in all the regions that were analyzed after correction for multiple comparisons. Analyses of fractional anisotropy and radial diffusivity are presented in Tables 5.3 and 5.4. These results indicate that heritability estimates for these measurements made in the twin samples are generalizeable to the singleton population, and there is no difference in developmental trajectories of monozygotic and dizygotic twins.

However, twins and singletons did exhibit differences in axial diffusivity measures in the anterior limb of the internal capsule and the anterior region of the corona radiate (Table 5.5). There were significant differences in the delay parameter of the Gompertz function for these

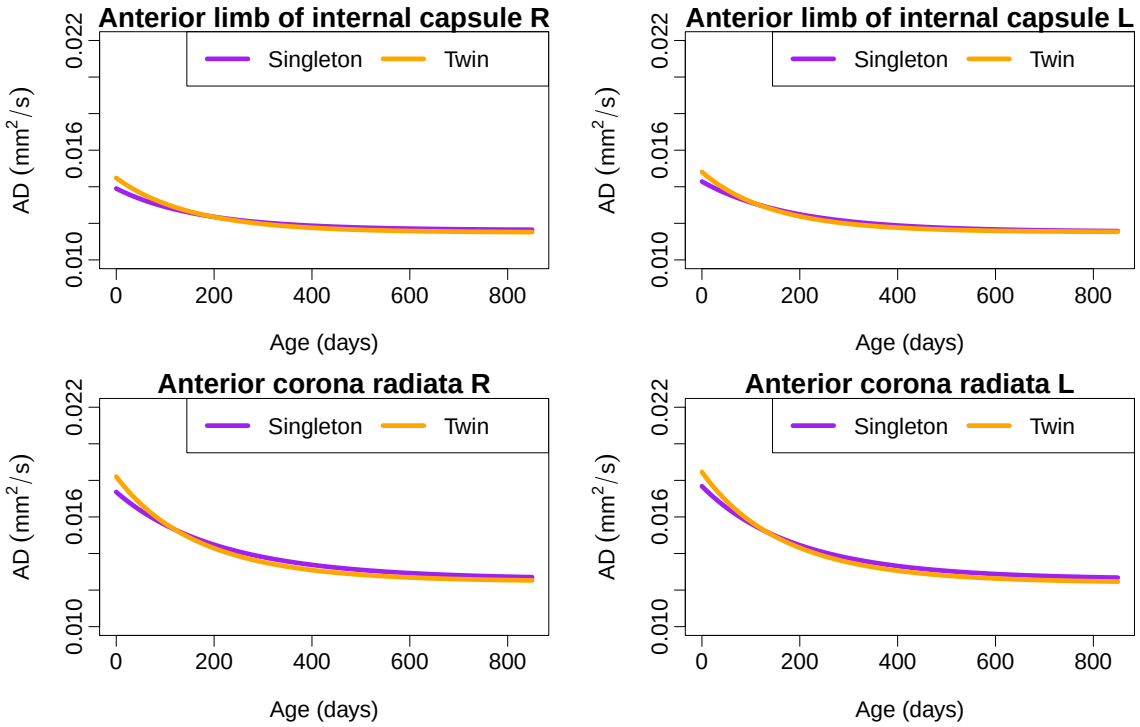

Figure 5.1: Comparison of AD growth trajectory of twins and singletons for the anterior limb of the internal capsule and the anterior corona radiata. The delay parameter was significantly different between twins and singletons in these regions.

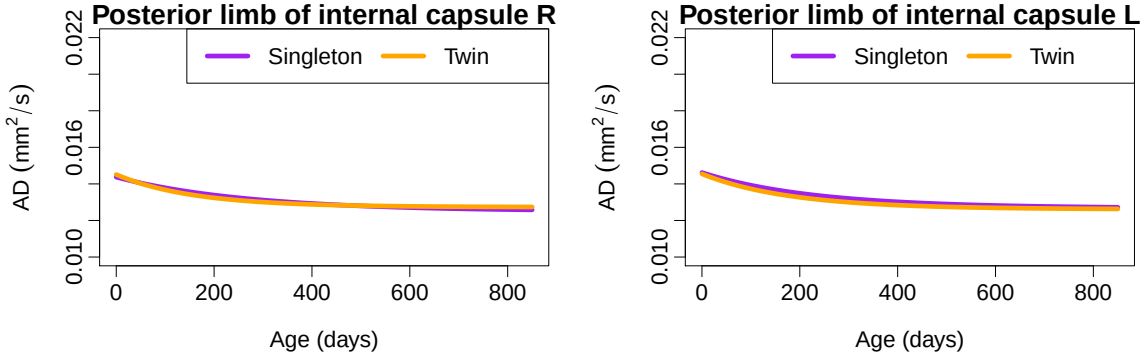

Figure 5.2: Comparison of AD growth trajectory of twins and singletons. There were no significant differences between twin and singleton trajectories in the posterior limb of the internal capsule.

Table 5.3: Group Differences in Fractional Anisotropy of White Matter Regions Between Singletons and Twins.

WM Label	Asymptote		Delay		Speed	
	Raw p	p*	Raw p	p*	Raw p	p*
Genu of corpus callosum	0.473	0.660	0.711	0.933	0.296	0.512
Body of corpus callosum	0.566	0.660	0.682	0.933	0.902	0.987
Splenium of corpus callosum	0.641	0.663	0.445	0.849	0.987	0.987
Anterior limb of internal capsule R	0.055	0.388	0.057	0.502	0.268	0.512
Anterior limb of internal capsule L	0.230	0.660	0.995	0.995	0.566	0.793
Posterior limb of internal capsule R	0.504	0.660	0.263	0.703	0.869	0.987
Posterior limb of internal capsule L	0.307	0.660	0.301	0.703	0.984	0.987
Retrolenticular part of internal capsule R	0.306	0.660	0.782	0.966	0.720	0.945
Retrolenticular part of internal capsule L	0.663	0.663	0.624	0.933	0.804	0.987
Anterior corona radiata R	0.542	0.660	0.156	0.656	0.312	0.512
Anterior corona radiata L	0.623	0.663	0.096	0.502	0.236	0.512
Superior corona radiata R	0.287	0.660	0.012	0.246	0.317	0.512
Superior corona radiata L	0.513	0.660	0.208	0.703	0.230	0.512
Posterior corona radiata R	0.433	0.660	0.075	0.502	0.162	0.512
Posterior corona radiata L	0.509	0.660	0.293	0.703	0.160	0.512
Posterior thalamic radiation R	0.096	0.504	0.350	0.734	0.080	0.512
Posterior thalamic radiation L	0.267	0.660	0.948	0.995	0.100	0.512
External capsule R	0.023	0.282	0.569	0.918	0.002	0.051
External capsule L	0.027	0.282	0.832	0.971	0.007	0.072
Superior longitudinal fasciculus R	0.340	0.660	0.955	0.995	0.190	0.512
Superior longitudinal fasciculus L	0.531	0.660	0.567	0.918	0.552	0.793

* Based on the false discovery rate adjustment for multiple comparisons

Table 5.4: Group Differences in Radial Diffusivity of White Matter Regions Between Singletons and Twins.

WM Label	Asymptote		Delay		Speed	
	Raw p	p*	Raw p	p*	Raw p	p*
Genu of corpus callosum	0.241	0.699	0.338	0.880	0.088	0.185
Body of corpus callosum	0.680	0.714	0.749	0.880	0.189	0.305
Splenium of corpus callosum	0.532	0.699	0.738	0.880	0.213	0.320
Anterior limb of internal capsule R	0.280	0.699	0.808	0.893	0.272	0.356
Anterior limb of internal capsule L	0.569	0.703	0.271	0.880	0.528	0.616
Posterior limb of internal capsule R	0.676	0.714	0.382	0.880	0.899	0.915
Posterior limb of internal capsule L	0.483	0.699	0.950	0.950	0.777	0.859
Retrolenticular part of internal capsule R	0.238	0.699	0.754	0.880	0.151	0.265
Retrolenticular part of internal capsule L	0.532	0.699	0.519	0.880	0.915	0.915
Anterior corona radiata R	0.411	0.699	0.295	0.880	0.046	0.185
Anterior corona radiata L	0.654	0.714	0.096	0.880	0.070	0.185
Superior corona radiata R	0.284	0.699	0.248	0.880	0.034	0.185
Superior corona radiata L	0.375	0.699	0.295	0.880	0.036	0.185
Posterior corona radiata R	0.508	0.699	0.361	0.880	0.087	0.185
Posterior corona radiata L	0.319	0.699	0.518	0.880	0.031	0.185
Posterior thalamic radiation R	0.257	0.699	0.589	0.880	0.088	0.185
Posterior thalamic radiation L	0.152	0.699	0.891	0.935	0.041	0.185
External capsule R	0.176	0.699	0.297	0.880	0.097	0.185
External capsule L	0.336	0.699	0.571	0.880	0.242	0.339
Superior longitudinal fasciculus R	0.437	0.699	0.670	0.880	0.085	0.185
Superior longitudinal fasciculus L	0.783	0.783	0.537	0.880	0.365	0.451

* Based on the false discovery rate adjustment for multiple comparisons

Table 5.5: Group Differences in Axial Diffusivity of White Matter Regions Between Singletons and Twins.

WM Label	Asymptote		Delay		Speed	
	Raw p	p*	Raw p	p*	Raw p	p*
Genu of corpus callosum	0.211	0.973	0.091	0.166	0.852	0.852
Body of corpus callosum	0.137	0.973	0.918	0.964	0.016	0.333
Splenium of corpus callosum	0.208	0.973	0.833	0.921	0.048	0.431
Anterior limb of internal capsule R	0.362	0.973	0.000	0.001	0.743	0.780
Anterior limb of internal capsule L	0.917	0.973	0.002	0.024	0.258	0.431
Posterior limb of internal capsule R	0.227	0.973	0.531	0.620	0.094	0.431
Posterior limb of internal capsule L	0.711	0.973	0.977	0.977	0.402	0.527
Retrolenticular part of internal capsule R	0.758	0.973	0.142	0.212	0.185	0.431
Retrolenticular part of internal capsule L	0.899	0.973	0.285	0.352	0.650	0.737
Anterior corona radiata R	0.588	0.973	0.009	0.045	0.169	0.431
Anterior corona radiata L	0.352	0.973	0.006	0.042	0.308	0.431
Superior corona radiata R	0.655	0.973	0.079	0.166	0.146	0.431
Superior corona radiata L	0.740	0.973	0.033	0.109	0.243	0.431
Posterior corona radiata R	0.959	0.973	0.211	0.295	0.192	0.431
Posterior corona radiata L	0.478	0.973	0.226	0.296	0.067	0.431
Posterior thalamic radiation R	0.595	0.973	0.036	0.109	0.473	0.584
Posterior thalamic radiation L	0.731	0.973	0.127	0.206	0.292	0.431
External capsule R	0.914	0.973	0.070	0.163	0.273	0.431
External capsule L	0.524	0.973	0.029	0.109	0.667	0.737
Superior longitudinal fasciculus R	0.973	0.973	0.052	0.137	0.259	0.431
Superior longitudinal fasciculus L	0.882	0.973	0.095	0.166	0.155	0.431

* Based on the false discovery rate adjustment for multiple comparisons

regions, indicating that twins were delayed compared to singletons. However, twins appear to have caught up to singletons by 3 to 4 months postterm as though they experience a period of "catch-up" growth postbirth. Fig. 5.3 shows the relative difference between twins and singletons during the first 6 months. There were no significant differences in the asymptote parameter of the Gompertz function, suggesting that the twin-singleton differences observed early on in these regions disappear by early childhood.

In summary, growth trajectories of fractional anisotropy and radial diffusivity showed no significant differences. Significant differences were observed only in the axial diffusivity in the anterior limb of the internal capsule and the anterior region of the corona radiata; however, these differences seem to disappear early in life. No effect of zygocity on growth trajectories was found. The findings suggest that twins can be included with singletons in studies of early brain development, but researchers should control for gestational age.

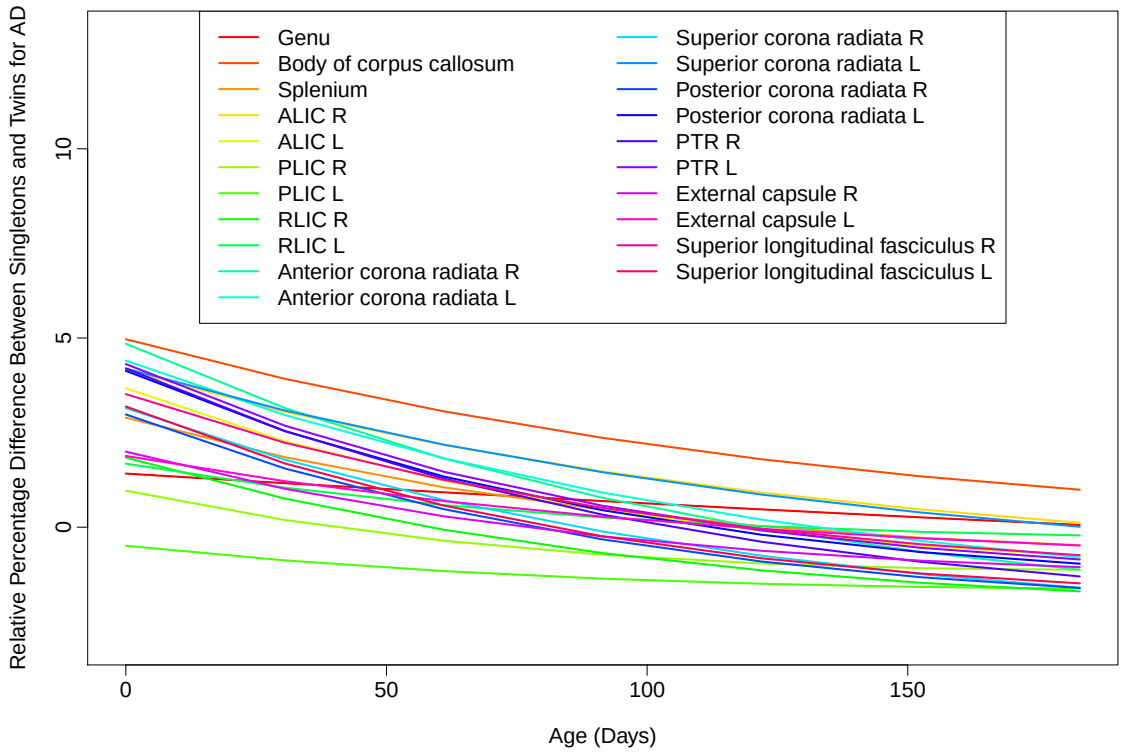

Figure 5.3: Relative percentage difference of AD between singletons and twins for the first 6 months after birth, $((AD_{twins} - AD_{singletons})/AD_{singletons}) * 100$. Twins have slightly higher AD values at birth; however, they catch up quickly to singletons during the first few months after birth. Anterior and posterior limb of the internal capsule are denoted as ALIC and PLIC, respectively. RLIC is the retrolenticular part of the internal capsule and PTR is the posterior thalamic radiation.

CHAPTER 6

MULTIVARIATE NONLINEAR MIXED EFFECTS MODELS

6.1 Introduction

In Chapters 3 and 4, we have primarily shown applications of the nonlinear mixed effects model to diffusion parameters. In Chapter 7, we showed that T1W anatomical MRI also shows an interesting pattern as the brain matures. In this chapter, we apply our framework to analysis of T1W and T2W images in addition to the diffusion measurements. Moreover, we propose a multivariate nonlinear mixed effects model as opposed to multiple univariate models as the former takes the correlation among the modalities into account.

Prior studies of diffusion and structural MRI have shown changes in early brain development, including changes of diffusion parameters over time [56, 57] and contrast changes as depicted in T1W and T2W [58]. Relatively few studies have looked at both DTI and MRI [15] and most of these studies have been cross-sectional. Due to the high water content of the infant brain, T1 and T2 times are relatively long and result in a low signal in white matter regions of the brain. As the infant grows, water content decreases, which results in changes of signal intensity. Also, myelination is associated with low signal intensity in T2W images and increased signal intensity in T1W images. As the brain matures, the observed signal intensities of T1W and T2W images change, reflecting the underlying biological changes.

In this chapter, we extend our nonlinear mixed effects framework to jointly model temporal changes of T1W, T2W, and fractional anisotropy to gain a better insight into brain maturation. We construct normative growth models for all the modalities, taking into account the correlation among the modalities and individuals, along with an estimation of the variability of the population trends.

6.2 Extension to Multivariate Analysis

T1 and T2 shortening happens more rapidly in the first year of life with gradual but less dramatic changes in the second year. The signal intensity of T2W decreases over time, in a pattern similar to RD, and T1W intensities show an increasing pattern similar to FA. As such, we model the changes of structural MRI with the Gompertz function. In Chapter 2, we showed the Gompertz function can appropriately model changes during early brain development. We extend the nonlinear mixed effects model introduced in Chapter 2 to multivariate modeling of multimodal MRI data to study the variation of different imaging modalities in space and time using intuitive parameterization of growth trajectories.

Specifically, we model temporal growth for an individual i, time points t_{ij} and image channel/modality $c \in \{c_1 \dots c_k\}$ by the nonlinear mixed effect model of the Gompertz function

$$\begin{bmatrix} y_{ij}^c \\ \vdots \end{bmatrix} = \begin{bmatrix} f(\phi_i^c, t_{ij}) \\ \vdots \end{bmatrix} + e_{ij} = \begin{bmatrix} \phi_{1i}^c \exp\{-\phi_{2i}^c \phi_{3i}^{c\, t_{ij}}\} \\ \vdots \end{bmatrix} + e_{ij} \tag{6.1}$$

where the mixed effects are $\phi_i^c = [\phi_{1i}^c \ \phi_{2i}^c \ \phi_{3i}^c]^T = \beta^c + b_i^c$. The fixed effects for modality c, $\beta^c = [\beta_1^c \ \beta_2^c \ \beta_3^c]^T$, represent mean values of parameter ϕ_i^c in the population. This parameterization intuitively decomposes the mean of temporal changes of a population as saturation (β_1), delay (β_2) and speed ($-\log \beta_3$). The random effects for each subject i and modality c , $b_i^c = [b_{1i}^c \ b_{2i}^c \ 0]^T$, explain individual variation from the mean. We set one of the random effects to zero to reduce the number of random effects in the model. Most of the variation of individuals can be captured by b_1 and b_2 and including extra random effects in the model may cause the matrix Ψ to be rank-deficient. Also, in Section 2.4.1, we concluded that the Gompertz function with asymptote and delay as random effects does well in fitting the growth trajectories during early brain development. By imposing joint multivariate distribution on random effects of all the modalities, $b_i = [b_{1i}^{c_1}, b_{2i}^{c_1}, \dots, b_{1i}^{c_k}, b_{2i}^{c_k}] \sim \mathcal{N}(0, \Psi)$, we capture both interindividual variability within a modality as well as associations among the growth patterns seen in different modalities.

6.3 Results

We perform an analysis on a set of repeated scans of 26 healthy subjects acquired at approximately 2 weeks, 1 year, and 2 years of age. These are the same subjects used in the studies in Chapter 3. However, in addition to the DTI data, T1W and T2W of subjects are also included. As was mentioned previously, four of the subjects had suboptimal DTI scans at 1 year that were removed, but their scans for other time points and modalities

were included. The images include T1W, T2W, and DTI. The registration methodology introduced in 3.2.2 was utilized where the unbiased atlas building framework [33] was applied to the set of T2W images at 1 year to obtain spatial mappings between each subject through the estimated atlas. Intrasubject registration was performed by IRTK software [32]. All time points of each subject are registered to this atlas via linear and nonlinear transformations, first by mapping these images to the year 1 scan and then cascading the two transformations for a mapping to the atlas. Tensor maps are calculated for each DTI scan, and are registered to the atlas using transformations obtained by registering the DTI baseline (B0) images to T2W images. T1W images were normalized using the intensity value of fatty tissue between the skull and skin. For T2W, the Cerebrospinal fluid (CSF) region of the ventricles was used for normalization. Fractional anisotropy features from the registered tensors were used for the joint analysis between DTI and structural MRI.

We analyzed growth trajectories in white and gray matter anatomical regions, using atlases developed and disseminated by Mori *et al.* [39] and the Harvard Center for Morphometric Analysis [59]. A parcellation map was registered to our year 1 atlas to define lobar regions. Also, in addition to regions defined by Mori *et al.*, we were interested in comparing white matter and gray matter regions in specific lobar regions. To accomplish this task, we applied the Prastawa *et al.* [60] segmentation method to obtain maps of gray and white matter. This segmentation map combined with the lobar regions was used to define white matter regions of interest in addition to white matter regions defined by Mori *et al.* [39]. Fig. 6.1 shows the parcellation map along with the segmentation results for the atlas. Regions of interest are extracted based on the lobe and tissue of interest. For example,

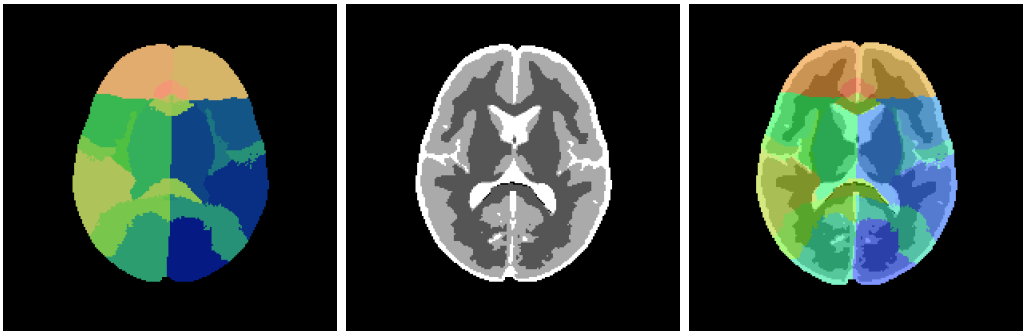

Figure 6.1: Parcellation and segmentation results. Left: Parcellation map of the atlas. Middle: Segmentation results, darker gray indicates white matter regions, light gray is gray matter and white areas are cerebrospinal fluid. Right: Parcellation map overlaid on top of the segmented atlas.

if one is interested in analyzing the frontal white matter, the white matter region in the frontal lobe is selected for further analysis.

Fig. 6.2 shows the right posterior thalamic radiation (PTR) overlaid on the longitudinal T1W, T2W, and FA images of one subject. Original data and the estimated multivariate population trend for T1W, T2W, and FA are shown in Fig. 6.3. PTR includes optic radiation, and it is one of the white matter tracts that matures early [61]. There is a rapid change in T1W and T2W in the first year followed by slower maturation during the second year.

Fig. 6.4 shows the population trends and confidence intervals for the body of corpus callosum (BCC), posterior limb of the internal capsule (PLIC), and superior longitudinal

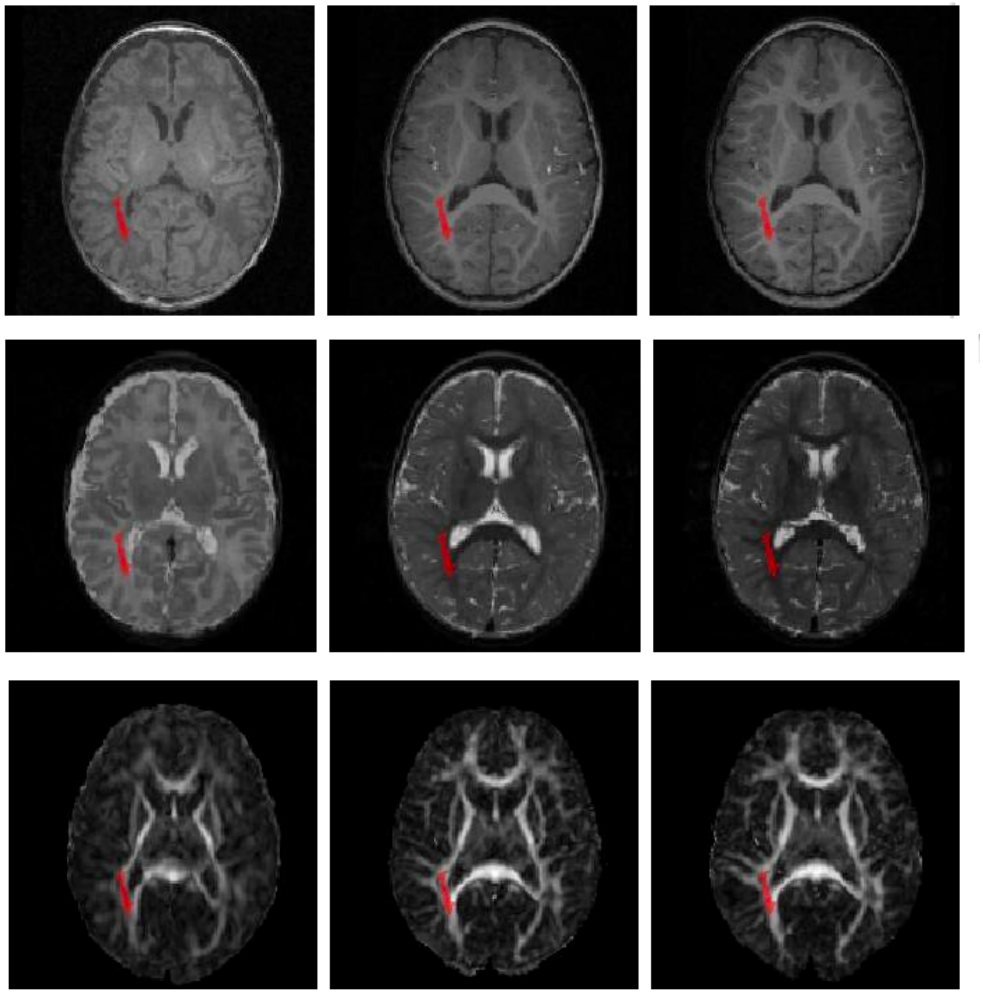

Figure 6.2: Coregistered multimodal MRI data. Left to right: Images taken at 2 weeks, 1 year, and 2 years. Top to bottom: T1W, T2W, and FA. Posterior thalamic radiation is shown by the red label on the images.

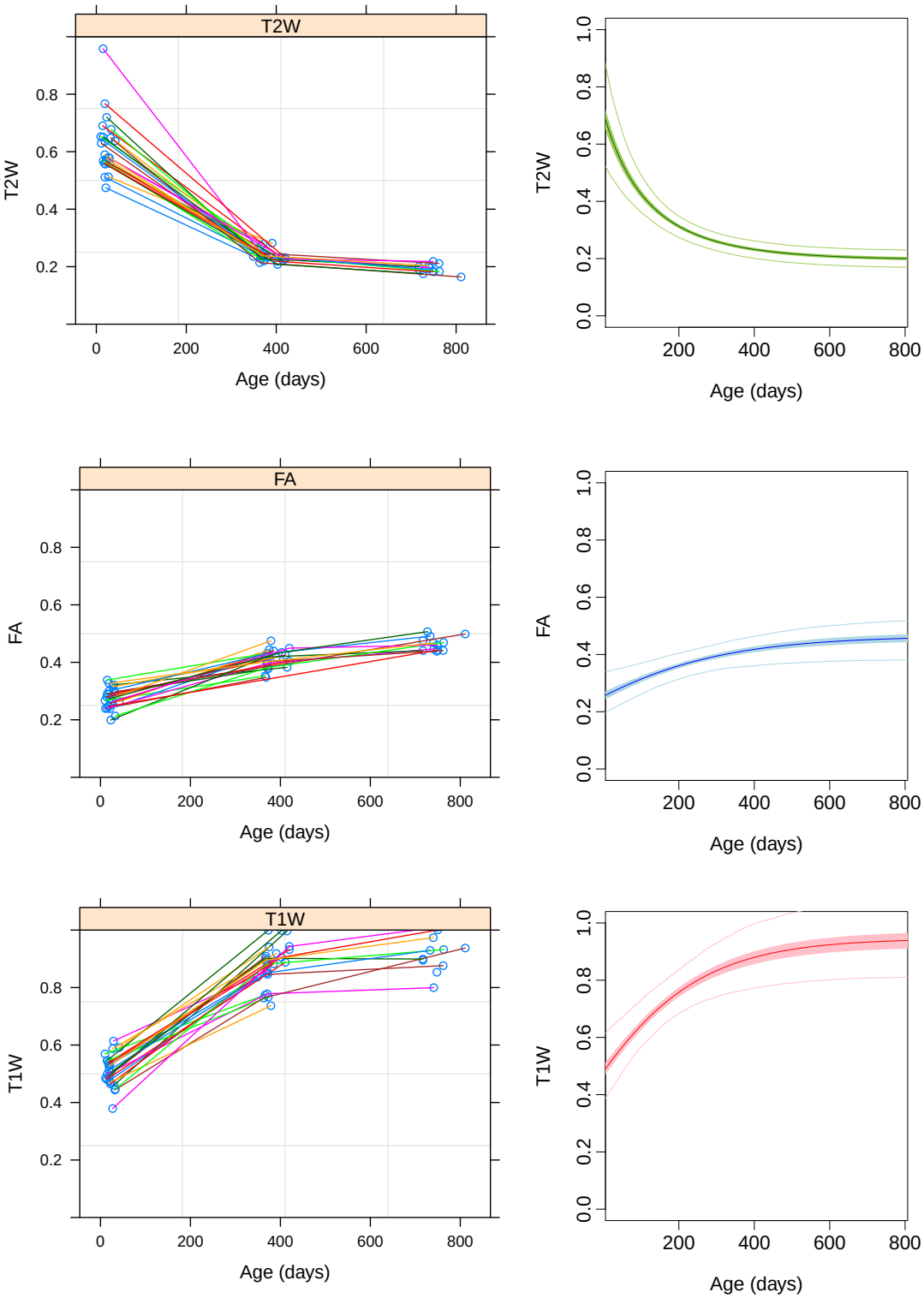

Figure 6.3: Age-related changes of T2W, T1W, and FA for PTR. Left: Original observed values for PTR from top to bottom: T2W, FA, and T1W. Right: Estimated population trajectory along with 95% confidence and predictive intervals. The shaded region denotes the confidence interval of the average trajectory whereas the predictive intervals are shown as thin lines above and below the mean trajectory.

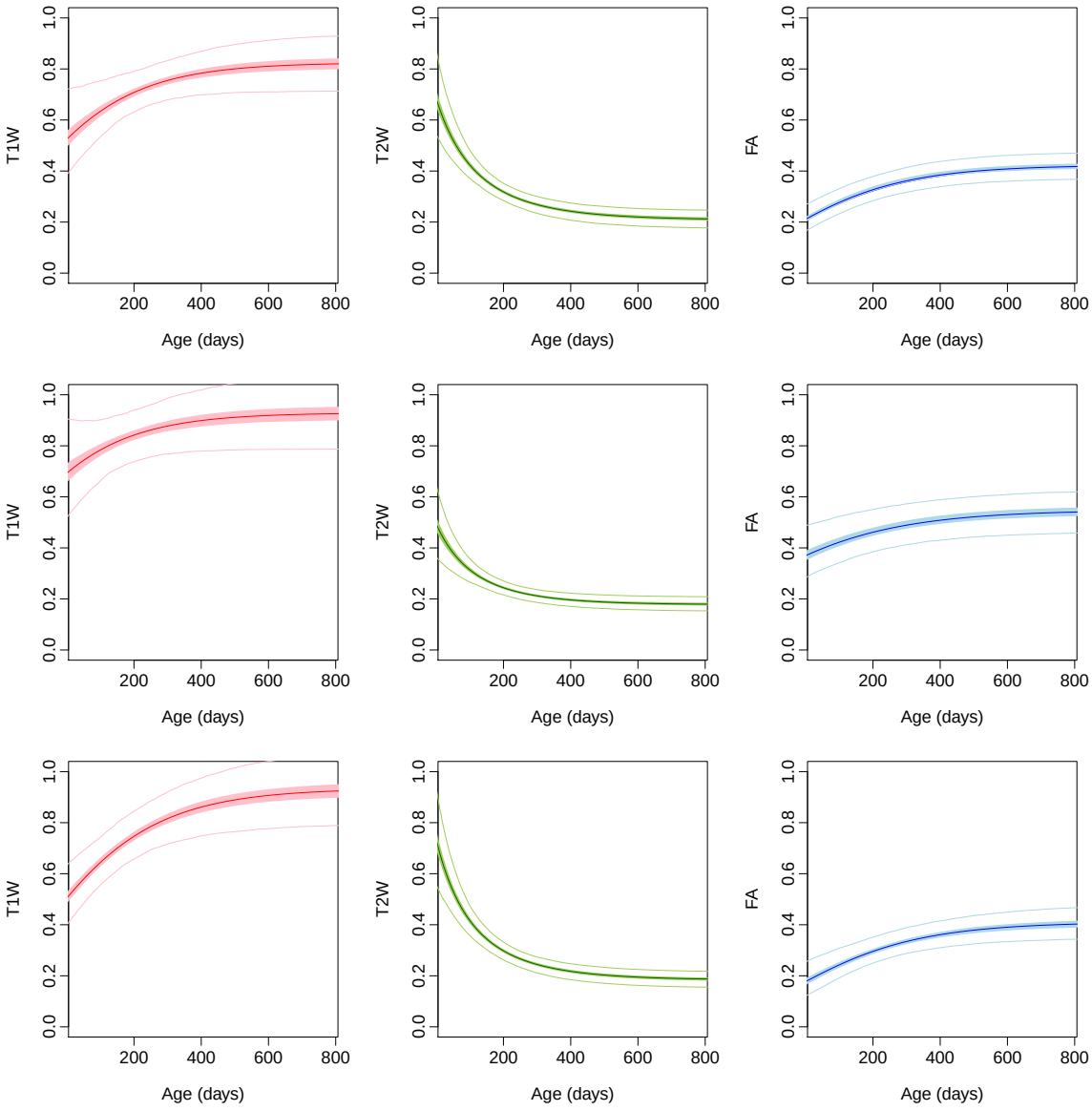

Figure 6.4: Population growth trajectories (bold) and confidence intervals (light). From top to bottom: body of corpus callosum (BCC), posterior limb of internal capsule (PLIC), and superior longitudinal fasciculus (SLF). Bold curves are the average growth trajectories for normalized T1W (red), T2W (green), and FA (blue), while the 95% confidence interval of the curves is shown as shaded regions. Light color curves show the 95% predicted intervals for each region.

fasciculus (SLF). The body of corpus callosum is known to have a very limited myelination at birth, whereas the PLIC is known to be one of the regions that shows early myelination. This pattern is evident as PLIC has higher FA and T1W values, with lower T2W values compared to BCC and the SLF. However, BCC and SLF show a quick maturation during the first year, especially in T2W.

We also analyze growth trajectories in gray matter, even though DTI analysis has been typically performed only in white matter. We observe small changes in FA values as gray matter matures; however, the changes of T1W and T2W are larger, as expected. Fig. 6.5 shows the changes of white and gray matter of the prefrontal lobe. T1W and FA increase with age and T2W intensities decrease with age.

Intensity changes are higher for white matter compared to gray matter as shown in the right part of Fig. 6.5. Higher FA values are observed in white matter compared to gray matter due to the fiber structure in white matter. We also observe high variability of FA and T2W at birth for white matter, whereas T1W has high variability throughout early brain development.

6.4 Conclusion

Chapter 6 extended the nonlinear mixed effect modeling of Chapter 2 to multivariate data. By imposing a joint multivariate distribution on the random effects, we were able to capture the correlation among different types of scans (T1W, T2W, and FA) and account for the correlations that exist among these modalities. We showed a good match between the raw data and the estimated population trajectories. Further validation is needed to compare the multivariate growth trajectories versus multiple univariate model fitting. The work presented in this chapter indicates that the nonlinear mixed effects modeling can be extended to multimodal data. However, as the dimensionality of the data increases, the estimation of the covariance of random effects can become problematic. Methods utilizing pseudolikelihood estimation might prove to be useful in these cases.

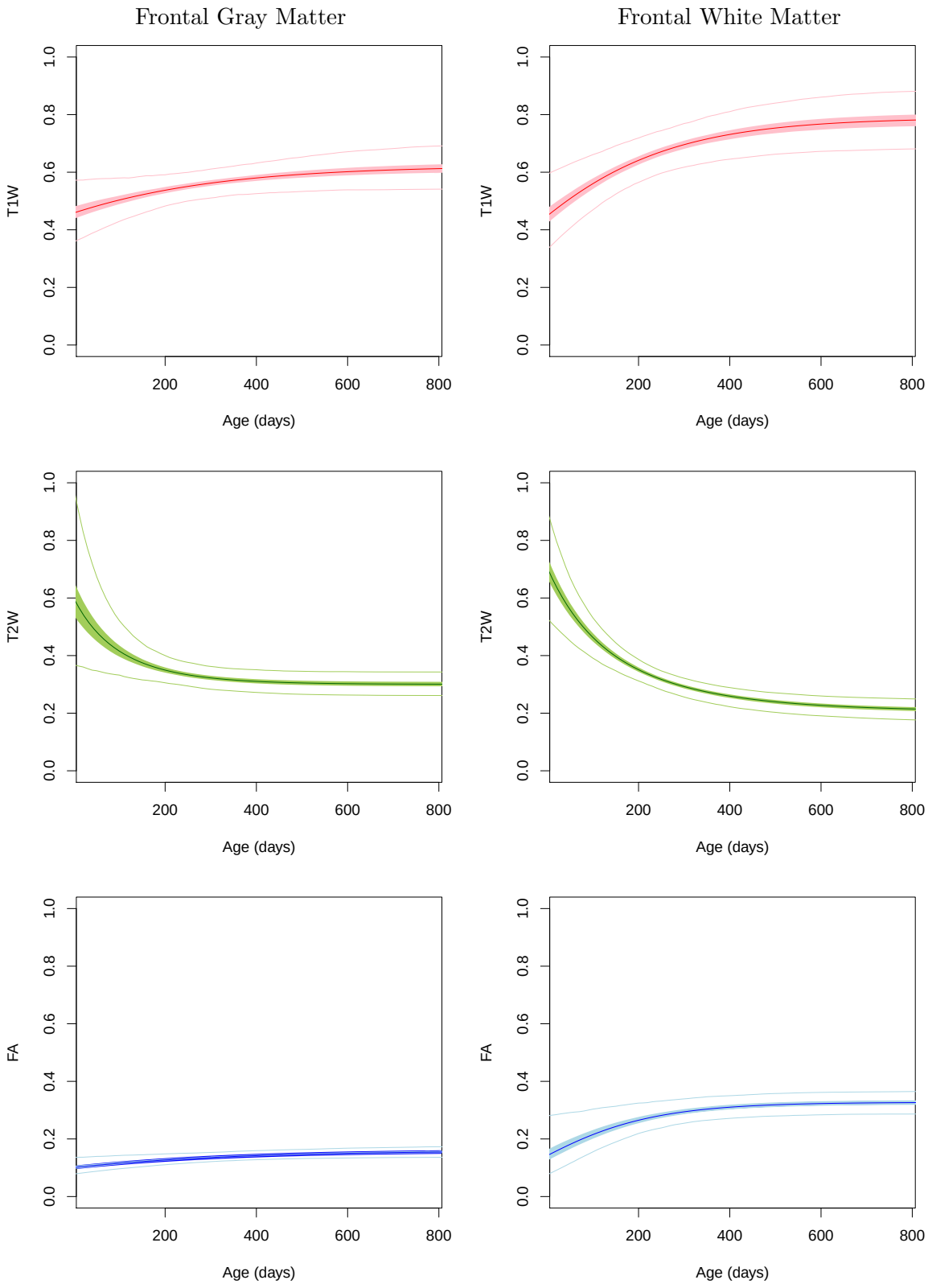

Figure 6.5: Plots of T1W, T2W, and FA of the prefrontal lobe during early years of life. Bold curves are the average growth trajectories for normalized T1W (red), T2W (green), and FA (blue), while the 95% confidence interval of the curves is shown as shaded regions. Light color curves show the 95% predicted intervals for each region.

CHAPTER 7

SUBJECT-SPECIFIC ANALYSIS

Chapters 3, 4, 5, and 6 addressed two major motivations of longitudinal data analysis, which are characterization of normal brain development (Chapters 3 and 6) and comparison of group trajectories (Chapters 4 and 5). Another equally important aspect of our method is the prediction of individual trajectories. Longitudinal population analysis is important in understanding normal brain development or pathophysiology of disease (i.e., different regions in the normative model, or comparison of typical development versus atypical development), but individuals will likely benefit from subject-specific assessments and personalized continuous trajectories. For example, in the study of growth, one might be interested in obtaining the subject-specific growth profile. In this chapter, two methods are proposed to address subject-specific analysis: comparison of an individual scan to the normative model and prediction of an individual trajectory based on one or more new scans.

First, we discuss the calculation of the prediction interval, which will serve as a reference range for future observations. Later, we discuss the subject-specific assessments utilizing this prediction interval.

7.1 Prediction Interval

Monte Carlo simulation is employed to estimate the prediction intervals. Prediction intervals provide a range of values and a probability that a future observation will fall within the range. The maximum likelihood estimates of fixed effects, $\hat{\beta}$, covariance of random effects, $\hat{\Psi}$, and noise, $\hat{\sigma}$ are used to estimate the prediction interval. One thousand samples of $\beta \sim \mathcal{N}\left(\hat{\beta}, \left[\sum_{i=1}^{M} \hat{X}_i^T \hat{V}_i^{-1} \hat{X}_i\right]^{-1}\right)$, $b \sim \mathcal{N}(0, \hat{\Psi})$, and $e \sim \mathcal{N}(0, \hat{\sigma})$ were generated from their respective distributions. Subsequently, 1000 trajectories were constructed by the NLME model:

$$y = f(\phi, t) + e \tag{7.1}$$

where $\phi = A\beta + Bb$ and f is the Gompertz function. A is the identity matrix and B is $[1\ 0\ 0; 0\ 1\ 0; 0\ 0\ 0]$. The approximate $100(1-\alpha)\%$ prediction interval was calculated

point-wise at each t_j, where $j = 1, \cdots, 800$ days, and $\alpha = .05$. At each t_j, $\alpha/2$ and $1 - \alpha/2$ percentiles were calculated as the lower and upper limit of the interval. Fig. 7.1 shows the calculated 95% prediction interval for FA values of posterior thalamic radiation. The prediction interval can serve as a reference range; upon availability of a new scan, the diffusivity measures or intensity of structural MRI can be compared to the normative model for a region of interest to indicate whether the scan is within the normal range or outside. Percentiles also can be calculated for the individual. Here, an arbitrary $\alpha = .05$ was selected corresponding to the 95% predictive interval. This parameter can be adjusted based on the needs of clinicians.

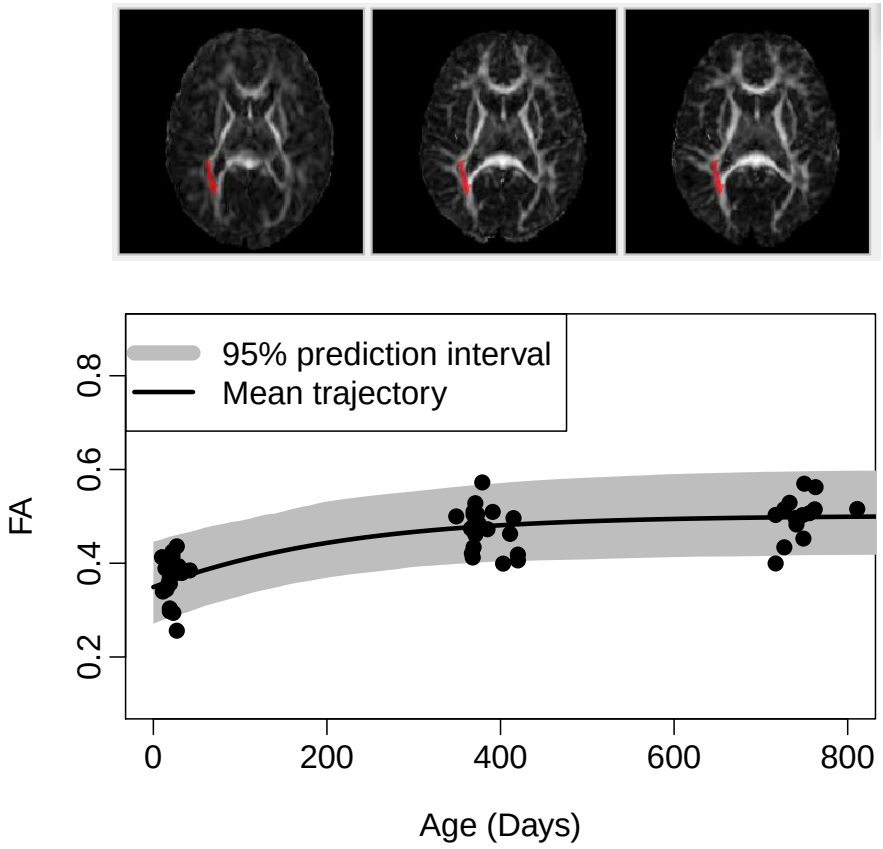

Figure 7.1: Prediction interval for posterior thalamic radiation (PTR). Top: PTR is shown as the red label on the longitudinal FA images of one subject. Bottom: The mean trajectory along with the 95% prediction interval (shaded area) is shown for PTR. Black circles indicate mean FA value of PTR for a scan of an individual.

7.2 Evaluation of Individual Scan

This section describes the necessary steps to compare an individual scan to the normative model. Upon availability of an individual scan, we can compare the intensity values of T1W, T2W, or diffusion parameters of DTI by first registering the scan(s) to the template of the normative model. The tensors are estimated using weighted least squares tensor estimation [54]. If only DTI data are available, the tensors are registered to the template using transformations obtained by registering the DTI baseline (B0) images to the template. Tensors are resampled using finite strain reorientation and Riemannian interpolation [35, 36, 37].

Once the scan is in the same space as the template, intensity values or diffusion parameters of regions of interest are extracted. Here the Mori *et al.* white matter label map [39] is used as this label map is already in the atlas space (as described in Chapter 2). The intensity and diffusion parameters of region of interest can be compared to the predictive interval to indicate whether the scan is within the normal range or outside. Fig. 7.2 shows two cases compared to the normative model. Both of these cases are healthy subjects randomly selected from the normative population. For each scenario, the prediction interval has been estimated from the approximate maximum likelihood estimates of nonlinear mixed effects model parameters without including the subject in the model estimation. As is shown in Fig. 7.2, both of these subjects' scans fall within the normal range.

7.3 Prediction of Individual Trajectory

Longitudinal data analysis can provide further insight into growth by analyzing the growth trajectories themselves rather than a snapshot through time. In this setting, in-

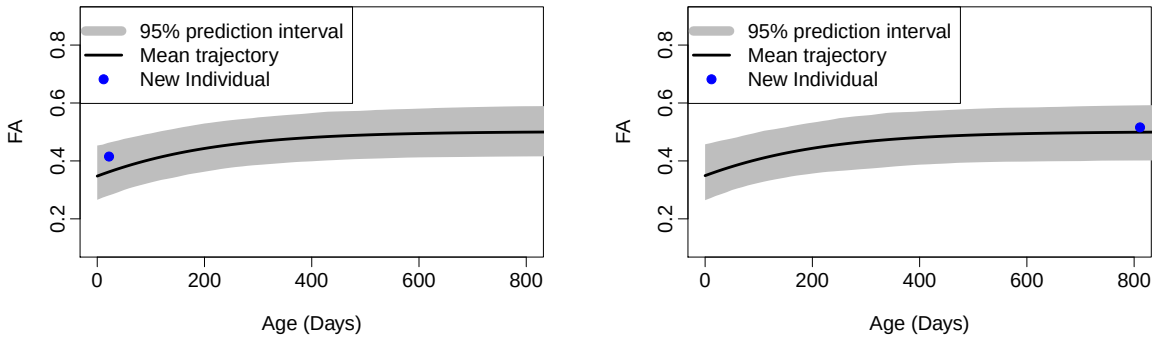

Figure 7.2: Demonstration of automated abnormality detection using the predicted interval. Scans of new subjects (blue dots) are shown in comparison to the predicted interval. Both of these individuals have values that fall within the normal range.

dividual subjects' trajectories can be compared to the normative model. The timing of deviation from typical trajectories can be identified and interventions can be targeted toward a specific developmental period. Because each trajectory is parameterized in terms of intuitive Gompertz parameters, it is possible to determine the effect of developmental differences for future time points. The patients can receive personalized treatment based on their developmental trajectory, and the effectiveness of the therapy (e.g., speech, visual, drug) can be assessed by monitoring the changes of the patients' trajectories.

In the mixed effects model, we can predict the individual growth trajectory over time as these models distinguish between fixed effects (population) and random effects (subject-specific). To be more specific, we can obtain predictions of subject-specific effects b_i and subject-specific growth trajectory $X_i\beta + Z_i b_i$ if the growth is modeled via linear mixed effects or $f(\phi_i, t_i)$ for nonlinear mixed effects where $\phi_i = A_i\beta + B_i b_i$. In order to compute b_i, we need to predict the conditional mean of b_i given the responses y_i, $E(b_i|y_i)$. In the case of LME and when all the covariance parameters of random effects are known, this prediction is well known: $b_i = \Psi Z_i^T V_i^{-1}(y_i - X_i\beta)$ where $V_i = Z_i \Psi Z_i^T + I\sigma^2$ [62]. However, in general the covariance parameters are unknown and the maximum likelihood estimates of the covariance parameters are used in place of the unknown true covariance parameters. The resulting predictor is

$$\hat{b}_i = \hat{\Psi} Z_i^T \hat{V}_i^{-1}(y_i - X_i\hat{\beta}). \tag{7.2}$$

Replacing $\hat{b}_i$ and $\hat{\beta}$ in the LME model, the $X_i\beta + Z_i b_i$, growth profile of the ith subject is as follows:

$$E\left[\hat{y}_i|b_i\right] = x_i\hat{\beta} + z_i\hat{b}_i \tag{7.3}$$

where x_i represents a vector of fixed effects covariates and z_i represents a vector of covariates corresponding to random effects.

In the nonlinear mixed effects model, the prediction of b_i is not a simple closed form solution; however, it can be calculated from the posterior distribution of $p(b_i|y_i)$ using Baye's rule:

$$p(b_i|y_i, \beta, \Psi, \sigma^2) = \frac{p(y_i|\beta, b_i, \Psi, \sigma^2)p(b_i|\Psi)}{p(y_i|\beta, \Psi, \sigma^2)}. \tag{7.4}$$

By maximizing the log of the posterior density of b_i, we obtain the following objective function:

$$l(b_i) = -\frac{1}{\sigma^2}(y_i - f(\beta, b_i))^T(y_i - f(\beta, b_i)) - b_i^T\Psi^{-1}b_i. \tag{7.5}$$

Once $\hat{b}_i$ is estimated, we can construct continuous growth trajectories of the ith subject. The ith subject prediction for the corresponding responses y_i is:

$$E\left[\hat{y}_i|b_i\right] = f(x_i^T\hat{\beta} + z_i^T\hat{b}_i, t). \tag{7.6}$$

Fig. 7.3 shows the predicted individual trajectories for the posterior thalamic radiation region. All the individuals show a rapid increase in FA value during the first year with continued growth but at a slower rate in the second year.

7.4 Subject-Specific Prediction Interval

In section 7.2, we showed how prediction intervals can be used as a reference range for future observations. These intervals can indicate whether an individual scan is within the normal range. An alternative and perhaps a more useful approach would be to predict the individual's trajectory upon availability of any new observations. We first predict individual random effects, b_i, and use these values to estimate the subject's individual trajectory and subject-specific prediction interval. In the linear mixed effects model and when Ψ and σ are known, b_i is the empirical Bayes estimator with the following posterior distribution:

$$b_i|y_i, \beta, \Psi, \sigma \sim \mathcal{N}(\hat{b}_i, \hat{W}_i), \tag{7.7}$$

where $\hat{b}_i = \Psi Z_i^T V_i^{-1}(y_i - X_i\hat{\beta})$ and $W_i = \Psi - \Psi Z_i^T V_i^{-1} Z_i \Psi$ [63]. When β, Ψ, and σ are unknown, they are replaced by their corresponding estimates. For the nonlinear mixed effects model, we follow the Lindstrom and Bates [20] approximation by taking the first-order expansion of $f(\phi_i, t_i)$ around $b_i = \hat{b}_i$. Note that $\phi_i = A_i\beta + B_i b_i$. Using this approximation, the posterior mean and variance of $b_i|\beta, \Psi, \sigma$ are as follows:

$$E[b_i|y_i, \beta, \sigma] = \Psi\hat{Z}_i^T V_i^{-1}(y_i - f(A_i\beta + B_i\hat{b}_i, t_i) + \hat{Z}_i\hat{b}_i), \tag{7.8}$$

$$Var[b_i|y_i, \beta, \sigma] = W = \Psi - \Psi\hat{Z}_i^T V_i^{-1}\hat{Z}_i\Psi, \tag{7.9}$$

where $\hat{Z}_i = \frac{\partial f_i}{\partial b_i^T}|_{\hat{\beta},\hat{b}_i}$ and $\hat{X}_i = \frac{\partial f_i}{\partial \beta^T}|_{\hat{\beta},\hat{b}_i}$. We substitute $\hat{\beta}$, $\hat{\Psi}$, and $\hat{\sigma}$ of the reference population for the unknown parameters to predict an approximate empirical Bayes estimate of b_i:

$$\hat{b}_i \simeq \hat{\Psi}\hat{Z}_i^T\hat{V}_i^{-1}(y_i - f(A_i\hat{\beta} + B_i\hat{b}_i, t_i) + \hat{Z}_i\hat{b}_i) \tag{7.10}$$

By knowing the sampling distribution $b_i \sim \mathcal{N}(\hat{b}_i, \hat{W})$, we can employ a Monte Carlo simulation similar to section 7.1 to approximate the subject-specific prediction interval. One thousand samples of $\beta \sim \mathcal{N}\left(\hat{\beta}, \left[\sum_{i=1}^{M}\hat{X}_i^T\hat{V}_i^{-1}\hat{X}_i\right]^{-1}\right)$, $b \sim \mathcal{N}(\hat{b}_i, \hat{\Psi} - \hat{\Psi}\hat{Z}_i^T V_i^{-1}\hat{Z}_i\hat{\Psi})$, and $e \sim \mathcal{N}(0, \hat{\sigma})$ were generated from their respective distributions. Subsequently, 1000 trajectories were constructed by the NLME model of (7.1). The prediction interval for the "new" subject can be calculated by constructing $1 - \alpha$ range of values for a given time

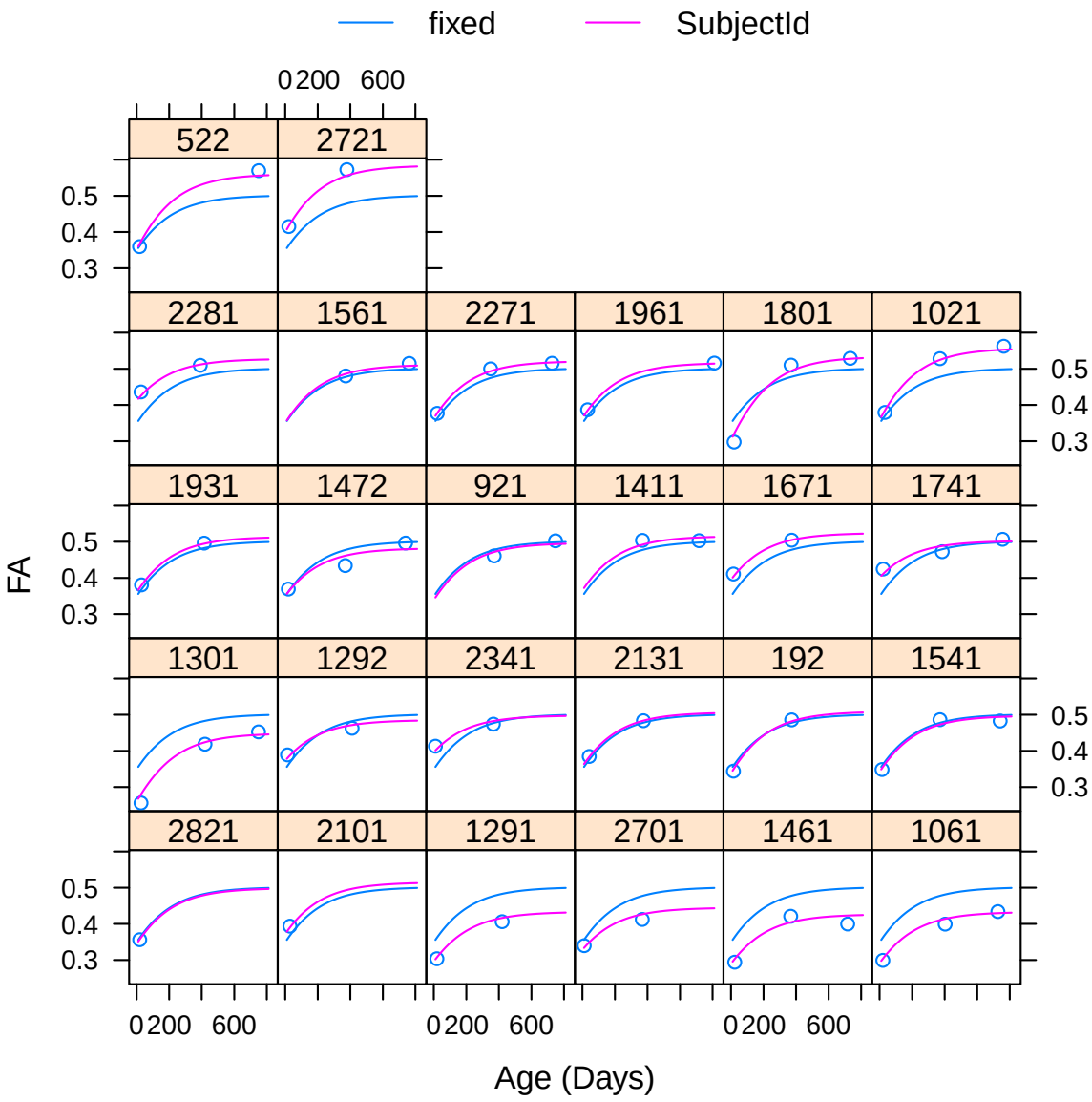

Figure 7.3: The fitted curves from the Gompertz model to the FA values of posterior thalamic radiation of 26 individuals. Blue curves show the estimated population trajectory (fixed) whereas purple curves show the individual trajectories (subject). The blue circles are the observed FA values.

point, t_{ij}. At each t_{ij}, $\alpha/2$ and $1-\alpha/2$ percentiles were calculated as the lower and upper limit of the subject-specific interval.

Fig. 7.4 shows the approximate subject growth trajectory along with the subject-specific prediction interval for FA values of one subject. With availability of only one scan, the growth trajectory of the individual is predicted using the estimated population parameters of the normative model $\hat{\beta}$ and variance and covariance parameters, $\hat{\sigma}$ and $\hat{\Psi}$, of the reference population. The reference population for this analysis is all the subjects excluding the one used for testing. The model parameters estimated by fitting the nonlinear mixed effects model to all the available data excluding the test subject are used in place of β, σ, and Ψ.

Fig. 7.5 shows the growth trajectory for radial diffusivity of one individual. The predicted growth trajectory is in agreement with the left out time points. Upon availability of more time points, future time points are predicted with increased precision as is shown in Fig. 7.4 and 7.5.

Since the prediction intervals are based on a continuous growth trajectory, we can also predict earlier growth characteristics. We used the available scans at 1 year and 2 years to predict diffusion values for an individual at 2 weeks. Fig. 7.6 shows the predicted RD values for two individuals. In one case, two scans were available and used (1 year and 2 years) to predict diffusivity values at neonate, whereas the other individual did not have a scan at 2 years, so only the scan at 1 year was used for prediction. In both cases, the predicted RD values at 2 weeks fall within the individual's approximate predicted interval.

In total, we had 26 subjects available in this study from the normative study of Chapter 3. The distribution of the data is shown in Table 3.1. Nine of the subjects had the data available for all the time points (2 weeks, 1 year, and 2 year). In the first experiment, we used the population parameters and individual's scans at 2 weeks and 1 year to predict the FA and RD values at 2 years. Tables 7.1 and 7.2 show the resulting prediction of FA for the posterior thalamic radiation (PTR) and the posterior limb of the internal capsule (PLIC). The predicted FA values are in a close approximation of the actual observed FA for these regions with a root mean squared prediction error (RMSPE) of .02718 for PTR and .02669 for PLIC. Tables 7.3 and 7.4 show the prediction for RD values of the same regions. Again, the predicted values show a close approximation of the actual observed RD values for these regions with RMSPE of 2.437×10^{-5} for PTR and RMSPE of 2.060×10^{-5} for PLIC.

In the second experiment, we used only the neonate scan (about 2 weeks) along with the estimated population parameters to predict the FA and RD values for future time points (i.e., 1 year and 2 years). Overall, 20 subjects had scans available at 2 weeks and either 1

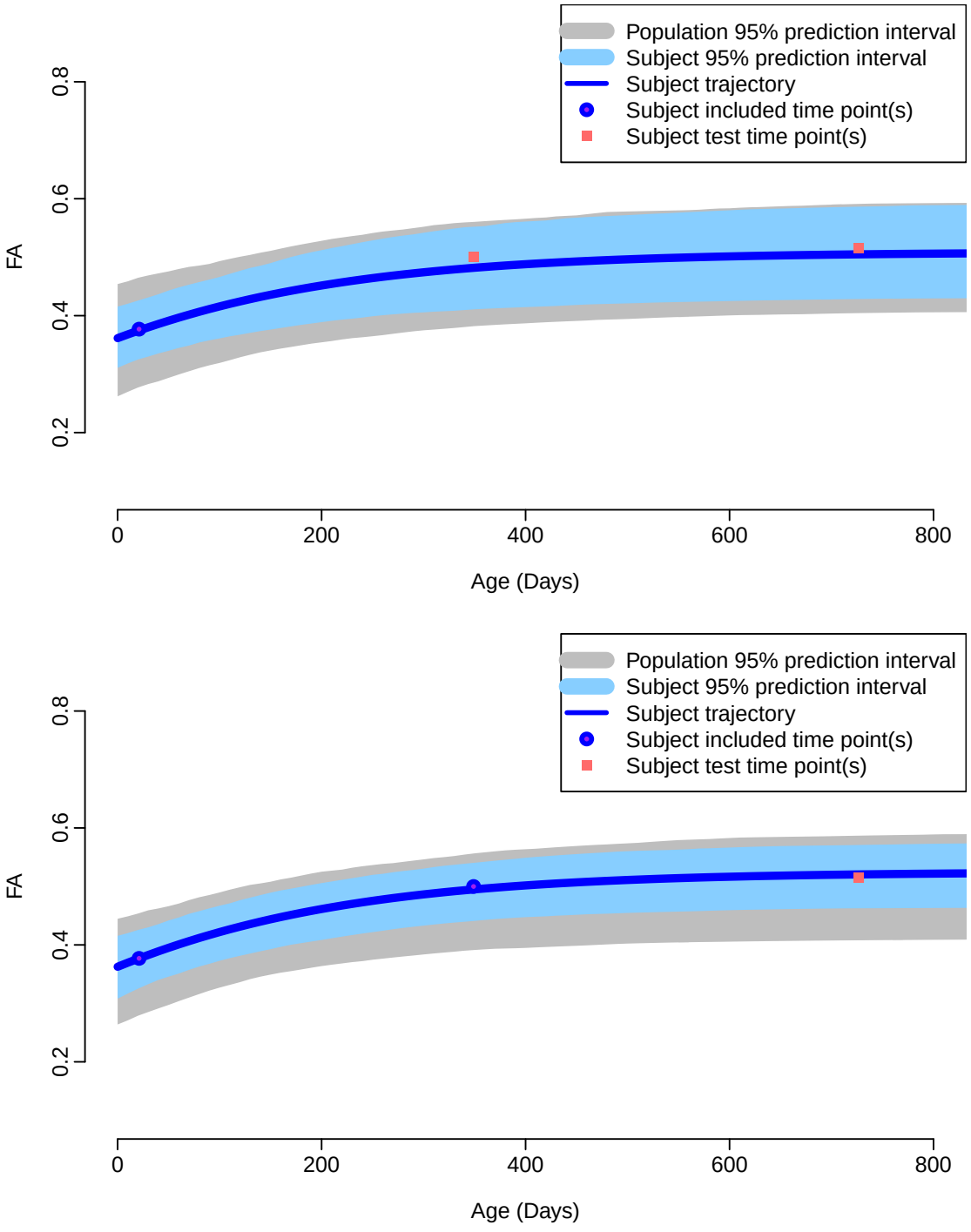

Figure 7.4: Subject prediction interval compared to the overall prediction for FA of posterior thalamic radiation. Top: subject-specific interval calculated based on only one time point (neonate). Bottom: subject-specific interval calculated based on scans at neonate and 1 year.

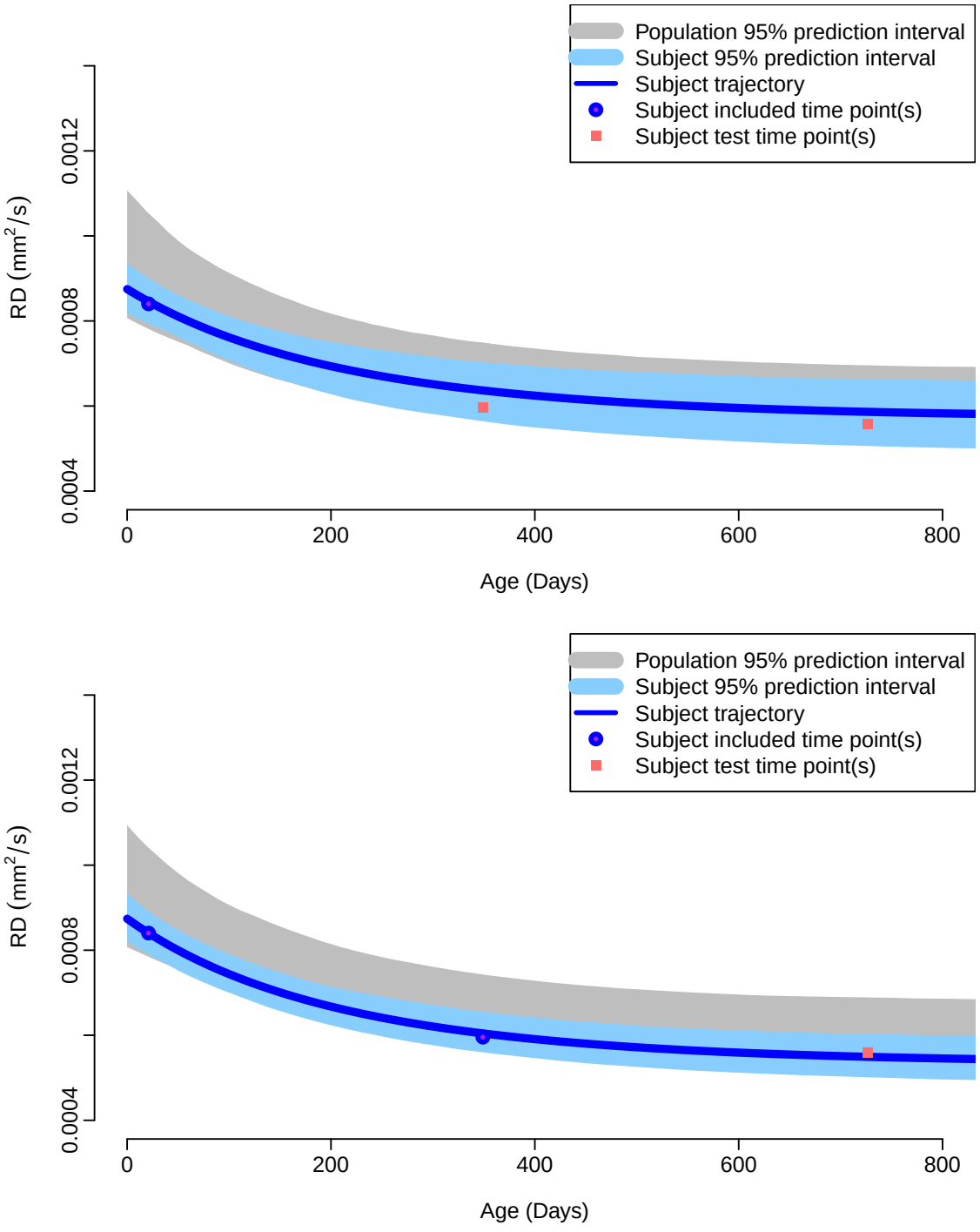

Figure 7.5: Subject prediction interval compared to the overall prediction for RD of posterior thalamic radiation. Top: subject-specific interval calculated based on only one time point (neonate). Bottom: subject-specific interval calculated based on scans at neonate and 1 year.

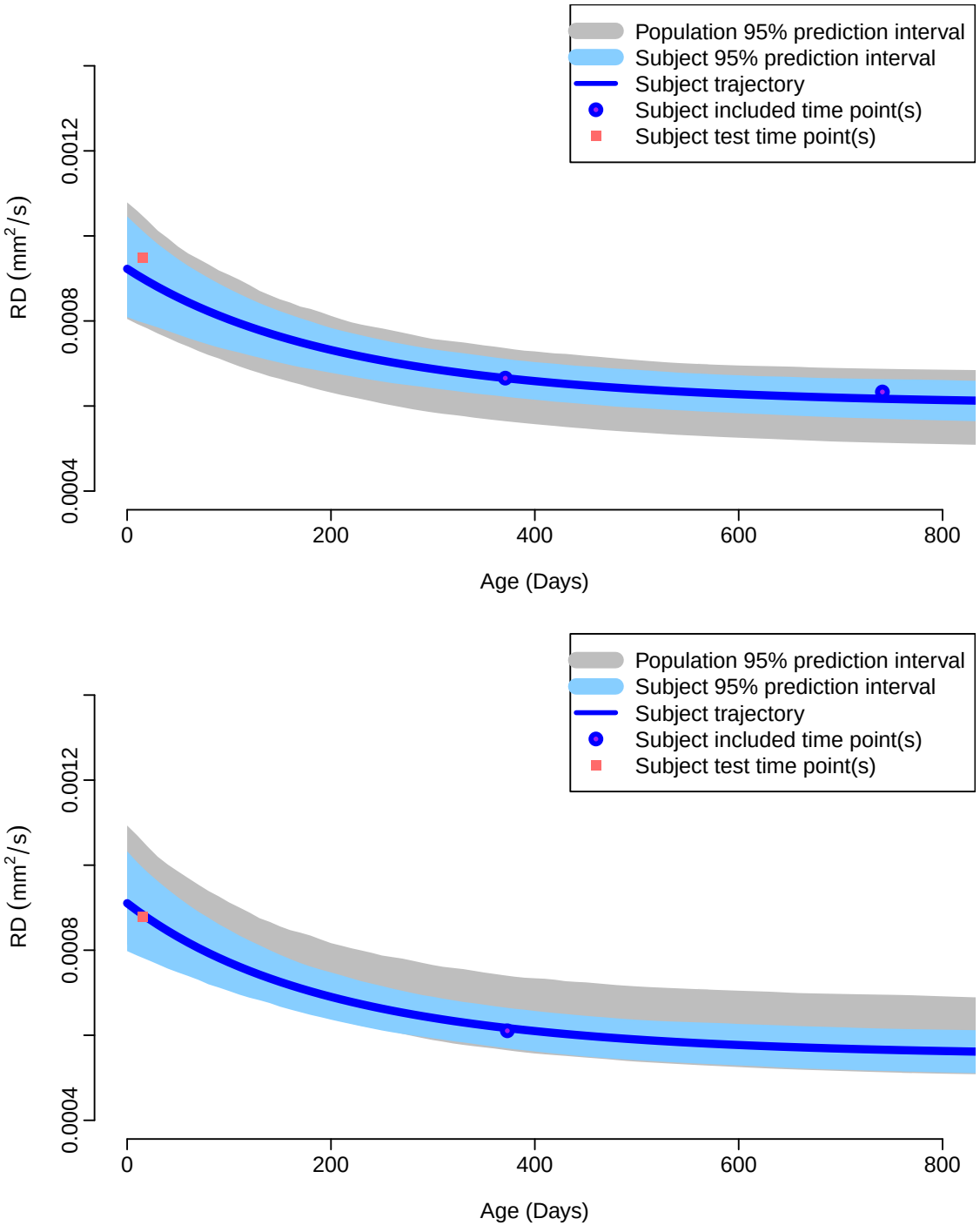

Figure 7.6: Subject prediction interval compared to the overall prediction for RD of posterior thalamic radiation. Top: subject-specific interval calculated based on only one time point (neonate). Bottom: subject-specific interval calculated based on neonate and 1 year time points.

Table 7.1: Predicted and Observed Values of FA for Posterior Thalamic Radiation. Neonate and 1 Year Scans Were Used to Predict Values of FA at About 2 Years.

	SubjectId	Age(Days)	Observed FA	Predicted FA	% of Observed FA
1	1021	763	0.562	0.538	95.7
2	1061	727	0.434	0.426	98.2
3	1301	749	0.453	0.435	96.2
4	1461	717	0.400	0.446	111.6
5	1472	740	0.497	0.455	91.7
6	1541	741	0.483	0.510	105.7
7	1741	756	0.507	0.482	95.2
8	1801	733	0.529	0.551	104.1
9	2271	727	0.515	0.521	101.0

*Percentage of observed FA is calculated based on ((predicted FA)/(observed FA)) *100

Table 7.2: Predicted and Observed Values of FA for Posterior Limb of Internal Capsule. Neonate and 1 Year Scans Were Used to Predict Values of FA at About 2 Years.

	SubjectId	Age(Days)	Observed FA	Predicted FA	% of Observed FA
1	1021	763	0.636	0.601	94.5
2	1061	727	0.595	0.574	96.5
3	1301	749	0.591	0.562	95.1
4	1461	717	0.552	0.557	100.9
5	1472	740	0.584	0.543	92.9
6	1541	741	0.491	0.472	96.2
7	1741	756	0.572	0.544	95.2
8	1801	733	0.433	0.465	107.4
9	2271	727	0.627	0.622	99.2

*Percentage of observed FA is calculated based on ((predicted FA)/(observed FA)) *100

Table 7.3: Predicted and Observed Values of RD for Posterior Thalamic Radiation. Neonate and 1 Year Scans Were Used to Predict Values of RD at About 2 Years.

	SubjectId	Age(Days)	Observed RD	Predicted RD	% of Observed RD
1	1021	763	0.000542	0.000551	101.6
2	1061	727	0.000653	0.000655	100.3
3	1301	749	0.000644	0.000665	103.2
4	1461	717	0.000646	0.000604	93.5
5	1472	740	0.000629	0.000665	105.7
6	1541	741	0.000633	0.000609	96.2
7	1741	756	0.000622	0.000611	98.2
8	1801	733	0.000583	0.000551	94.6
9	2271	727	0.000559	0.000549	98.3

*Percentage of observed RD is calculated based on ((predicted RD)/(observed RD)) *100

Table 7.4: Predicted and Observed Values of RD for Posterior Limb of Internal Capsule. Neonate and 1 Year Scans Were Used to Predict Values of RD at About 2 Years.

	SubjectId	Age(Days)	Observed RD	Predicted RD	% of Observed RD
1	1021	763	0.000424	0.000442	104.1
2	1061	727	0.000467	0.000482	103.2
3	1301	749	0.000464	0.000480	103.5
4	1461	717	0.000487	0.000483	99.3
5	1472	740	0.000470	0.000493	104.9
6	1541	741	0.000537	0.000541	100.7
7	1741	756	0.000475	0.000485	102.2
8	1801	733	0.000601	0.000554	92.2
9	2271	727	0.000434	0.000420	96.9

*Percentage of observed RD is calculated based on ((predicted RD)/(observed RD)) *100

year or 2 year scans, which were used for testing. Tables 7.5 and 7.6 show the prediction results of RD and FA of posterior thalamic radiation for 30 scans. There is an increased level of error in the estimation by using only one scan as shown in Table 7.7; however, the results indicate that even by using one scan, we are able to approximate the future value. This result is potentially of utmost interest for imaging subjects at risk and for the infant autism study discussed previously. The main goal of the National Institutes of Health (NIH) funded study is to determine if image-derived phenotypes at a very early age may predict expected values much later, and thus also if these values may match the estimation intervals for high-risk subjects diagnosed or not diagnosed for ASD.

7.5 Conclusion

In this chapter, we have provided two methods for subject-specific analysis. The first approach utilized the available population parameters to provide a prediction interval for new scans. Once an individual scan is available, it can be compared to the normative range. However, once an individual subject's observations are available, we can predict a subject-specific prediction interval that not only takes into account the population estimated parameters, but also considers the new individual's available data. The subject-specific prediction interval yields a more precise interval that is specific to an individual. Here we are making the assumption that an individual will have a timewise trajectory similar to that of the reference population. This allows transfer of information from the estimated population model to the prediction of a new individual trajectory.

Prediction of growth characteristics can have significant clinical implications. It can be used to detect early signs of abnormalities. Taking the heterogeneity of individuals into account, this method provides an individualized type of assessment where an individual is compared to its own subject-specific growth trajectory. This could help clinicians develop individualized treatment and monitor progress over time.

Table 7.5: Observed and Predicted Values for RD of Posterior Thalamic Radiation. Neonate Scan Was Used to Predict Values of RD at About 1 Year and 2 Years.

	SubjectId	Age(Days)	Observed RD	Predicted RD	% of Observed RD*
1	192	373	0.000660	0.000641	97.1
2	522	750	0.000545	0.000618	113.3
3	1021	371	0.000594	0.000650	109.4
4	1021	763	0.000542	0.000598	110.3
5	1061	403	0.000709	0.000662	93.5
6	1061	727	0.000653	0.000615	94.2
7	1291	420	0.000694	0.000665	95.8
8	1292	411	0.000684	0.000635	92.8
9	1301	420	0.000714	0.000692	96.9
10	1301	749	0.000644	0.000641	99.5
11	1461	367	0.000675	0.000700	103.6
12	1461	717	0.000646	0.000632	97.8
13	1472	369	0.000714	0.000647	90.6
14	1472	740	0.000629	0.000599	95.3
15	1541	371	0.000666	0.000664	99.7
16	1541	741	0.000633	0.000607	95.9
17	1671	373	0.000611	0.000641	105.0
18	1741	385	0.000653	0.000630	96.4
19	1741	756	0.000622	0.000585	94.0
20	1801	369	0.000600	0.000650	108.4
21	1801	733	0.000583	0.000598	102.7
22	1931	415	0.000621	0.000599	96.4
23	1961	811	0.000582	0.000587	100.7
24	2131	375	0.000618	0.000633	102.5
25	2271	349	0.000596	0.000637	106.9
26	2271	727	0.000559	0.000586	105.0
27	2281	391	0.000631	0.000622	98.5
28	2341	366	0.000701	0.000624	89.0
29	2701	368	0.000698	0.000653	93.6
30	2721	379	0.000547	0.000641	117.2

*Percentage of observed RD is calculated based on ((predicted RD)/(observed RD)) *100

Table 7.6: Observed and Predicted Values for FA of Posterior Thalamic Radiation. Neonate Scan Was Used to Predict Values of FA at About 1 Year and 2 Years.

	SubjectId	Age(Days)	Observed FA	Predicted FA	% of Observed FA
1	192	373	0.486	0.468	96.4
2	522	750	0.570	0.494	86.7
3	1021	371	0.528	0.481	91.0
4	1021	763	0.562	0.500	89.0
5	1061	403	0.399	0.449	112.4
6	1061	727	0.434	0.468	107.8
7	1291	420	0.406	0.454	111.7
8	1292	411	0.463	0.501	108.2
9	1301	420	0.418	0.405	96.7
10	1301	749	0.453	0.420	92.8
11	1461	367	0.421	0.437	103.8
12	1461	717	0.400	0.466	116.5
13	1472	369	0.434	0.484	111.5
14	1472	740	0.497	0.502	101.1
15	1541	371	0.486	0.471	96.8
16	1541	741	0.483	0.494	102.3
17	1671	373	0.504	0.506	100.3
18	1741	385	0.473	0.517	109.3
19	1741	756	0.507	0.532	105.0
20	1801	369	0.510	0.427	83.6
21	1801	733	0.529	0.452	85.5
22	1931	415	0.496	0.489	98.6
23	1961	811	0.516	0.508	98.5
24	2131	375	0.483	0.484	100.0
25	2271	349	0.500	0.482	96.4
26	2271	727	0.515	0.505	98.0
27	2281	391	0.510	0.520	102.0
28	2341	366	0.474	0.511	107.8
29	2701	368	0.412	0.471	114.1
30	2721	379	0.572	0.501	87.5

*Percentage of observed FA is calculated based on ((predicted FA)/(observed FA)) *100

Table 7.7: Summary of Prediction Results for FA and RD of Posterior Thalamic Radiation.

	FA		RD	
Input Time Points	neo	neo + year 1	neo	neo + year 1
Predict Time Points	year 1, 2, or both	year 2	year 1, 2, or both	year 2
Total Number of Predictions	30	9	30	9
Mean Observed Value	0.4814008	0.4865759	0.0006341	0.0006123
RMSPE	0.0425242	0.0271860	0.0000416	0.0000244
RMSPE Normalized to the Mean	0.0883343	0.0558721	0.0655904	0.0398097
Average (Predicted/Observed)	100.38%	99.93%	100.07%	99.07%
Standard Deviation (Predicted/Observed)	8.99%	6.26%	6.92%	4.02%

CHAPTER 8

DISCUSSION

8.1 Summary of Contributions

In summary, this dissertation provides a new methodological framework to model change trajectories from time-discrete image data. This framework includes statistical tests between populations and the testing of subject-specific individual profiles in the context of normative models. The proposed modeling framework has been rigorously tested with synthetic simulation data in order to determine its feasibility and statistical properties. We applied this novel methodology to several longitudinal clinical neuroimaging studies of the early developing brain. Our results have increased our understanding of early brain development by providing: 1) a statistical framework to model growth trajectories of early brain development as represented in structural and diffusion MRI, 2) characterization of longitudinal changes of MRI parameters in multiple clinical studies, and 3) prediction of subject-specific growth trajectories.

To our knowledge, this is the first presentation of a comprehensive multimodal NLME-based parametric growth curve modeling to study temporal changes in neuroimaging data. The processing system integrates registration of multiple modalities and time points into a population-specific unbiased template, selection of regions of interest that are consistent over all time points, and parametric modeling and NLME analysis in an analysis package that is generic with respect to any type of clinical applications using longitudinal imaging.

The methodologies presented in this dissertation enable characterization of a normative model to better understand typical brain development, to model growth trajectories for groups at risk of mental disorders and for individuals who do get diagnosed with a disorder to gain a better understanding of the pathology of the disease and enable subject-specific analysis to better help individuals.

8.1.1 Statistical Framework

In Chapter 2, we presented multiple growth functions that could be used to model appearance and diffusion changes of MRI during early brain development. We favored parametric over nonparameteric methods as the former can capture the growth trajectories in relatively few parameters. Among parametric curves considered (polynomials, exponential, monomolecular, logistic, and Gompetz), we recommended the use of the Gompertz function, which has asymptotic properties and can capture the observed signal and intensity changes of MRI. The Gompertz model with asymptote and delay as random effects in general had the lowest AIC for the majority of regions analyzed. The Gompertz function provides an intuitive parameterization of growth trajectory in terms of asymptote, delay, and speed. The Gompertz model provides a description of longitudinal changes with the potential for detecting deviations from a typical growth trajectory sensitive to multiple neurodevelopmental phenomena.

In contrast to previous studies, we used nonlinear mixed effects modeling that can capture the nonlinear changes as observed in MRI via the Gompertz growth curve. Such modeling takes into account the correlation among repeated scans of individuals, handles unbalanced data (i.e., variable timing, missing time points), and can also incorporate subjects with only one or two time points, thus accounting for missing data. Growth modeling from longitudinal data via NLME jointly estimates individual and population trajectories, results in significantly improved models of growth and growth variability, and can differentiate between cohort and age effects [19].

This longitudinal data analysis can be done voxel-wise or based on regions of interest (ROI). In the voxel-based approach, images are all aligned to a template, and growth model trajectories are estimated for each voxel. Voxel-based analysis assumes that the normalization procedure (aligning all the images to the template) is accurate. An alternative approach pursued in this work is to group voxels into regions and to model growth trajectories for each region. Defining ROI can be a time consuming and user dependent task. To overcome these shortcomings, we registered all the images to the template atlas built from the population of images and used an expert defined white matter label map [39] to automatically group voxels into regions via registration of this label map to the template atlas. The labeling of regions in the atlas space allowed automatic partitioning of each subject's scans into the different anatomical regions.

Once all the subjects' scans and label maps are in the atlas space, we can estimate growth trajectories for ROIs using the NLME model. Hypothesis testing can be performed

to determine modes of longitudinal changes in terms of Gompertz growth parameters. A simulation study indicated that the methodology presented in Chapter 2 can capture the underlying differences as presented in the synthetic data.

8.1.2 Characterization of Longitudinal Changes of MRI Parameters in Multiple Clinical Studies

The framework developed in Chapter 2 was applied to multiple clinical studies as described in Chapters 3, 4, 5, and 6 to capture longitudinal changes of early brain development. In Chapter 3, the framework was applied to characterize the heterogeneous pattern of maturation in normal brain development to establish a normative reference model. We presented a method for making inferences about regional differences in diffusion properties known to vary by microstructural properties and developmental course [64, 65, 66, 67].

Assessment of brain growth patterns in these regions revealed a nonlinear pattern of maturation with considerable regional variation as also shown in previous studies [57, 68, 69]. In agreement with previous studies, increased FA and decreased MD, AD, and RD were observed within all the white matter regions during this period [68, 69, 70, 71]. This longitudinal pediatric study supports a rapid change during the first 12 months followed by slower maturation during the second year similar to previous studies [56, 57]. Our study, in addition to supporting earlier cross-sectional reports on negative correlation between age and diffusion parameters, provides greater statistical power to examine nonlinear patterns of maturation in various white matter regions. In addition to regional differences, our methodology revealed the type, timing, and nature of differences. Moreover, the normative growth trajectories provide a normative spatiotemporal model of tissue appearance changes of early brain development that can be used as a reference for testing individual subjects.

In Chapter 4, the methodology was applied to a pediatric autism study. In this study, children at high risk of autism (by virtue of having a sibling diagnosed with autism) were recruited. The analysis was performed between high risk infants who were eventually diagnosed with autism versus the ones who did not develop the disorder. This study presented some unique challenges as the DTI data were extremely noisy due to the choice of a special short imaging protocol. Many regions of the brain and many individuals exhibited trajectories that are not expected for this age range. For example, FA values in many regions showed an increasing trend followed by a decreasing trend at year 1. This trend was also apparent for individuals who did not get diagnosed with autism. We speculate this pattern is due to noise in acquired diffusion weighted images rather than the underlying biology. Nonetheless we performed tests for group differences among different fiber tracts. We found

asymptote and speed parameters to be significantly different in the radial diffusivity of the right inferior longitudinal fasciculus. Wolff *et al.* [29] also found differences in slope in this tract, but they used a linear growth model. For many regions, due to high levels of noise, we were not able to estimate model parameters. We also considered changes of T1W images. We found a surprising result: the individuals who did get diagnosed with autism had higher signal intensities in T1W scans. Further research needs to be done to validate the findings as these changes could be due to the intensity normalization of these images, a topic under current investigation by developing a new tissue contrast model [72].

We compared growth trajectories of twins and singletons in Chapter 5. First, we considered growth trajectories of monozygotic and dizgyotic twins; however, we found no effect of zygocity on the developmental trajectories. As a result, we combined MZ and DZ twins into one group and compared them against singletons. We found no significant differences in FA and RD values for regions that we analyzed; however, we found significant differences in the delay parameter of AD for the anterior limb of the internal capsule and the anterior region of the corona radiata.

In Chapter 6, we extended the univariate modeling of longitudinal trajectories to multivariate modeling where multiple growth curves are modeled simultaneously. The multivariate approach imposes a joint distribution on random effects of all the modalities. As a result, the correlations among modalities are taken into account. We used a trivariate nonlinear mixed effects model to estimate growth trajectories of T1W, T2W, and FA simultaneously. Further research will be necessary to compare the result of multiple univariate models versus one multivariate model. Overall, T1W and FA showed an increasing pattern during early brain development, whereas T2W showed a decreasing pattern over the 2 years after birth. The rate of change for all the modalities was higher in the white matter regions than in the gray matter regions. T1W and T2W showed a very rapid change during the first year, followed by slower maturation during the second year.

8.1.3 Subject-Specific Analysis

By utilizing nonlinear mixed effects modeling, we jointly estimate the population trajectory along with individual trajectories. This allows for a better modeling of longitudinal changes as the group trend reflects how individuals progress on average. As a by product of the application of NLME, each individual's growth trajectory is also estimated. This property will be crucial for efforts to improve prediction and diagnosis for individuals.

In Chapter 7, we presented methods for subject-specific analysis. We showed how prediction intervals can be estimated via a Monte Carlo simulation. Once the prediction

intervals are estimated for the normative models, new scans of individuals can be compared to this normative model to indicate whether subjects' observed MRI values are within the normal range for their age. As discussed with our clinical colleagues, there is significant potential use of such normative models of brain development for diagnosis in pediatrics.

We also provided methodology for the prediction of subject-specific growth trajectories based on limited MRI data. By using the normative model as a reference population, we took advantage of already estimated population parameters and intersubject variability to predict posterior modes of random effects and subject-specific growth trajectories. Using posterior distribution of random effects, prediction intervals are estimated via a Monte Carlo simulation. Predictions for past and future observations can be made. This could have significant clinical implications by improving early recognition of growth abnormalities, a concept that is also highlighted in our laboratory's collaborative publication with the autism consortium [29].

Overall the methodology and analysis presented in this dissertation have been developed with the strong motivation that by better understanding the typical trajectory and more precisely determining when deviations occur, we can preempt mental illness or at least improve the quality of life by choosing type and optimal timing of therapeutic intervention. This study might be a small step, but we hope that it will get us closer to identifying differences early on when therapy or drug treatment can be most effective.

8.2 Limitations

8.2.1 Registration

One of the key assumptions in this work is that all the subjects' scans can be registered to a common template. Misregistration in the atlas building procedure and subsequent mapping of all the individuals' scans to the common template can confound the statistical results. However, in this study, subjects with significant medical conditions that would affect brain development were excluded. Also, all the analyses were done on regions of interest that we expect to be more robust if compared to voxel-based analysis. Nonetheless, improved spatial registration will potentially improve the accuracy of the model as brain development is characterized by a rapid change of contrast and size, which makes registration a challenging task.

8.2.2 Approximation of Nonlinear Mixed Effects Model

As discussed in section 2.3.1.1, there is no closed form solution to the maximum likelihood of marginal density of y given in (2.15). Different approximations have been proposed

for estimating the log likelihood of y in the nonlinear mixed effects model. In this dissertation, we have considered the approximation by taking the first order Taylor expansion of the model function f around the conditional modes of random effects [20]. Others have proposed alternating methods such as Laplacian approximation [73] and Gaussian quadrature [74]. Both Laplacian approximation and Gaussian quadrature have increasing levels of accuracy and complexity. Pinheiro provides a comprehensive comparison of approximation methods in his dissertation [75]. He concludes that the alternating method of [20] provides an accurate and reliable estimation of the likelihood function. We have adopted this approximation in this work [75]; however, in the future other approximation methods that provide higher levels of accuracy can be utilized.

8.2.3 Intensity Normalization

T1W and T2W scans have mostly been used for qualitative assessment by radiologists and have been qualitatively explored. They also have been used for volumetric studies [2, 3, 5, 26]. However, the appearance of signal intensity of these images has been quantitatively explored in only a few studies [13, 58]. The lack of research in quantitative analysis of T1W and T2W images could be that the scans acquired at different times with different scanners can have arbitrary intensity profiles as these measures can vary due to a number of factors, such as pulse sequence, hardware calibration, and coil loading, to name a few. Some of these variations can be removed by intensity normalization. In this study, T1-weighted images were normalized using the high intensity value of fatty tissue between the skull and skin. For T2-weighted images, the high intensity CSF region of ventricles was used for normalization. The normalization presented here relies heavily on accurate registration of all the subjects' scans to the atlas. An alternative to T1W and T2W is to acquire spatial maps of T1 and T2 that measure the underlying tissue's T1 and T2 relaxation times [76, 77, 78]; however, these methods increase the acquisition time. Better normalization techniques are needed to improve the results of quantitative analysis of T1W and T2W.

8.2.4 Combining Multimodal MRI Data into Physical Meaning

The methodologies presented in this dissertation have been used to analyze changes in RD, AD, MD, FA, T1W, and T2W. Each measure can provide complementary information in regard to the underlying physiology. For example, T1 and T2 have been shown to be influenced by myelin concentration, whereas high anisotropy (FA) could be observed in unmyelinated regions, indicating that the axon is an important factor for the anisotropy [10,

79]. We also showed in Chapter 3 that regions with varying AD and RD can show similar FA profiles and that AD and RD can provide additional information to better explain changes observed in MD and FA. Song *et al.* [80] have shown evidence that demyelination often leads to increased RD and axonal injury reduces AD. Recent methods for more directly measuring the number of axons and axon radius [81] are needed to better explain the observed changes in DTI, T1W, and T2W.

8.3 Future Work

8.3.1 Longitudinal Tract-Based Analysis

In this work, modeling changes of signal intensity and diffusion parameters for specific regions of interest have been considered. Mean values of parameters of interest for a given region (i.e., mean FA for the anterior limb of the internal capsule) were calculated and statistical modeling was performed based on the average values. In the future, we can consider tract-based analysis where changes are modeled both across the tract and along time. Functional data analysis and functional mixed effects can be utilized to model changes along the tract [82, 83, 84]. This type of analysis will provide more detailed information about changes within an anatomical region of interest, and it will also take correlations along the tract into account [85, 86]. Tract-based statistics is an active area of research [85], and modeling these tract changes over time has been proposed [86]. However, these methods cannot include subjects with only one or two scans [86]. Extension of mixed effects modeling along tract and time can overcome some of the limitations of these methods, but these methods are not yet available.

8.3.2 Incorporating Covariates

In the current study, we have considered only age as a covaraite, but in a scenario of a clinical study, we will also need to control for other covariates such as gender or patient scores. The mixed effects model can easily be extended to include additional covaraite such as gender or clinical scores.

8.3.3 Multivariate Mixed Effects Modeling

This work has been based mainly on the univariate analysis of the signal intensities and the diffusion parameters of DTI. In Chapter 2, we provided the methodology to extend univariate mixed effects models to multivariate mixed effects. These univariate mixed effects models can be tied together into multivariate mixed effects by specifying a joint distribution for the random effects. However, increases in the number of random effects

can create computational problems. In the future, a pairwise modeling approach similar to [87] where all possible bivariates mixed effects models are fit can be used to avoid the dimensional limitation of multivariate mixed effects. Pairwise modeling can circumvent the dimensionality limitation of multivariate mixed effects models.

8.3.4 Twin Study

In Chapter 7, we presented a twin study in which we compared developmental trajectories of singletons to twins. We also compared the developmental trajectories of monozygotic versus dizygotic twins and found no differences in the developmental trajectories based on zygocity. We can extend our study by evaluating the contributions of environment and genetics on brain development by measuring these variations over time. Previous neuroimaging studies have enabled creation of a genetic map of the brain [88]. Infant longitudinal twin studies provide a unique opportunity to extend previous research by providing continuous maps of the effects of genes and the environment on the development of brain structure.

REFERENCES

[1] A. Pfefferbaum, D. Mathalon, E. Sullivan, J. Rawles, R. Zipursky, and K. Lim, "A quantitative magnetic resonance imaging study of changes in brain morphology from infancy to late adulthood," *Arch. Neurol.*, vol. 51, no. 9, pp. 874–887, 1994.

[2] R. Knickmeyer, S. Gouttard, C. Kang, D. Evans, K. Wilber, J. Smith, R. Hamer, W. Lin, G. Gerig, and J. Gilmore, "A structural MRI study of human brain development from birth to 2 years," *J. Neurosci.*, vol. 28, pp. 12 176–12 182, Nov. 2008.

[3] P. Hüppi, "Neuroimaging of brain development-discovering the origins of neuropsychiatric disorders?" *Pediatr. Res.*, vol. 64, p. 325, Oct. 2008.

[4] M. Murgasova, L. Dyet, D. Edwards, M. Rutherford, J. Hajnal, and D. Rueckert, "Segmentation of brain MRI in young children," *Acad. Radiol.*, vol. 14, pp. 1350–1366, 2007.

[5] H. Xue, L. Srinivasan, S. Jiang, M. Rutherford, A. D. Edwards, D. Rueckert, and J. V. Hajnal, "Automatic cortical segmentation in the developing brain," *Inf. Process Med. Imaging*, vol. 20, pp. 257–269, 2007.

[6] P. Yakovlev and A. Lecours, "The myelogenetic cycles of regional maturation of the brain," in *Regional Development of the Brain in Early Life*, A. Minkowski, Ed. Oxford, UK: Blackwell Scientific, 1967, pp. 3–70.

[7] M. Rutherford, Ed., *MRI of the Neonatal Brain.* Philadelphia: WB Saunders, 2002.

[8] M. Weinstein, L. Ben-Sira, Y. Levy, D. A. Zachor, E. Ben Itzhak, M. Artzi, R. Tarrasch, P. M. Eksteine, T. Hendler, and D. Ben Bashat, "Abnormal white matter integrity in young children with autism," *Hum. Brain Mapp.*, vol. 32, no. 4, pp. 534–543, 2011. [Online]. Available: http://www.ncbi.nlm.nih.gov/pubmed/21391246

[9] P. J. Basser, J. Mattiello, and D. LeBihan, "MR diffusion tensor spectroscopy and imaging," *Biophys. J.*, vol. 66, no. 1, pp. 259–267, 1994.

[10] S. Mori and J. Zhang, "Principles of diffusion tensor imaging and its applications to basic neuroscience research," *Neuron*, vol. 51, no. 5, pp. 527–539, 2006.

[11] C. Pierpaoli and P. J. Basser, "Toward a quantitative assessment of diffusion anisotropy," *Magnet. Reson. Med.*, vol. 36, no. 6, pp. 893–906, 1996.

[12] P. van Gelderen, M. H. de Vleeschouwer, D. DesPres, J. Pekar, P. van Zijl, and C. T. Moonen, "Water diffusion and acute stroke," *Magnet. Reson. Med.*, vol. 31, no. 2, pp. 154–163, 1994.

[13] N. Sadeghi, M. Prastawa, J. Gilmore, W. Lin, and G. Gerig, "Spatio-temporal analysis of early brain development," in *Proceedings IEEE Asilomar Conference on Signals, Systems and Computers–ASILOMAR*, 2010, pp. 777–781.

[14] A. L. Alexander, J. E. Lee, M. Lazar, R. Boudos, M. B. DuBray, T. R. Oakes, J. N. Miller, J. Lu, E.-K. Jeong, W. M. McMahon, E. D. Bigler, and J. E. Lainhart, "Diffusion tensor imaging of the corpus callosum in autism," *NeuroImage*, vol. 34, no. 1, pp. 61–73, 2007.

[15] J. Gilmore, W. Lin, I. Corouge, Y. Vetsa, J. K. Smith, C. Kang, H. Gu, R. Hamer, J. Lieberman, and G. Gerig, "Early postnatal development of corpus callosum and corticospinal white matter assessed with quantitative tractography," *Am. J. Neuroradiol.*, vol. 28, no. 9, pp. 1789–1795, 2007.

[16] C. J. Cascio, G. Gerig, and J. Piven, "Diffusion tensor imaging: Application to the study of the developing brain," *J Am Acad Child Psy*, vol. 46, no. 2, pp. 213–223, 2007.

[17] S. Pajevic and C. Pierpaoli, "Color schemes to represent the orientation of anisotropic tissues from diffusion tensor data: Application to white matter fiber tract mapping in the human brain," *Magnet. Reson. Med.*, vol. 42, no. 3, pp. 526–540, 1999.

[18] G. Fitzmaurice, N. Laird, and J. Ware, *Applied Longitudinal Analysis*, 2nd ed. Hoboken: John Wiley & Sons, 2011.

[19] P. Diggle, P. Heagerty, K. Liang, and S. Zeger, *Analysis of Longitudinal Data*, 2nd ed. New York: Oxford University Press, 2002.

[20] M. Lindstrom and D. Bates, "Nonlinear mixed effects models for repeated measures data," *Biometrics*, vol. 46, pp. 673–687, Sept. 1990.

[21] A. Karkach, "Trajectories and models of individual growth," *Demographic Res.*, vol. 15, no. 12, pp. 347–400, 2006. [Online]. Available: http://www.demographic-research.org/volumes/vol15/12/

[22] L. von Bertalanffy, "Untersuchungen über die gesetzlichkeit des wachstums. VII. Stoffwechseltypen und wachstumtypen," *Biologisches Zentralblatt*, vol. 61, pp. 510–532, 1941.

[23] A. P. Dempster, N. M. Laird, and D. B. Rubin, "Maximum likelihood from incomplete data via the EM algorithm," *J. Roy. Stat. Soc. B*, vol. 39, pp. 1–38, 1977. [Online]. Available: http://web.mit.edu/6.435/www/Dempster77.pdf

[24] N. M. Laird and J. H. Ware, "Random-effects models for longitudinal data." *Biometrics*, vol. 38, no. 4, pp. 963–974, 1982. [Online]. Available: http://view.ncbi.nlm.nih.gov/pubmed/7168798

[25] M. Lindstrom and D. Bates, "Newton-raphson and em algorithms for linear mixed effects models for repeated measures data," *J. Am. Stat. Assoc.*, vol. 83, pp. 1014–1022, 1988.

[26] S. Xu, M. Styner, J. Gilmore, J. Piven, and G. Gerig, "Multivariate nonlinear mixed model to analyze longitudinal image data: MRI study of early brain development," in *Computer Vision and Pattern Recognition Workshops–CVPRW*. IEEE Computer Society, 2008, pp. 1–8.

[27] M. D. Kogan, S. J. Blumberg, L. A. Schieve, C. A. Boyle, J. M. Perrin, R. M. Ghandour, G. K. Singh, B. B. Strickland, E. Trevathan, and P. C. van Dyck, "Prevalence of parent-reported diagnosis of autism spectrum disorder among children in the US, 2007," *Pediatrics*, vol. 124, no. 5, pp. 1395–1403, Nov. 2009.

[28] S. Ozonoff, G. S. Young, A. Carter, D. Messinger, N. Yirmiya, L. Zwaigenbaum, S. Bryson, L. J. Carver, J. N. Constantino, K. Dobkins, T. Hutman, J. M. Iverson, R. Landa, S. J. Rogers, M. Sigman, and W. L. Stone, "Recurrence risk for autism spectrum disorders: A baby siblings research consortium study," *Pediatrics*, vol. 128, no. 3, pp. e488–495, Sept. 2011.

[29] J. Wolff, H. Gu, G. Gerig, J. Elison, M. Styner, S. Gouttard, K. Botteron, S. Dager, G. Dawson, A. Estes, A. Evans, H. Hazlett, P. Kostopoulos, R. C. McKinstry, S. Paterson, R. Schultz, L. Zwaigenbaum, and J. Piven, "Differences in white matter fiber tract development present from 6 to 24 months in infants with autism," *Am. J. Psychiatry*, vol. 169, no. 6, pp. 589–600, Feb. 2012.

[30] C. Lord, M. Rutter, P. DiLavore, and S. Risi, *Autism Diagnostic Observation Schedule.* Los Angeles: Western Psychological Services, 2000.

[31] Z. Liu, Y. Wang, G. Gerig, S. Gouttard, R. Tao, T. Fletcher, and M. Styner, "Quality control of diffusion weighted images," in *SPIE Medical Imaging.* International Society for Optics and Photonics, 2010, pp. 76 280J–76 280J–9.

[32] D. Rueckert, L. Sonoda, C. Hayes, D. Hill, M. Leach, and D. Hawkes, "Nonrigid registration using free-form deformations: Application to breast MR images," *IEEE Trans. Med. Imaging*, vol. 18, no. 8, pp. 712–721, Aug. 1999.

[33] S. Joshi, B. Davis, M. Jomier, and G. Gerig, "Unbiased diffeomorphic atlas construction for computational anatomy," *NeuroImage*, vol. 23, pp. S151–160, 2004.

[34] M. Miller, A. Trouve, and L. Younes, "On the metrics and euler-lagrange equations of computational anatomy," *Annu. Rev. Biomed. Eng.*, vol. 4, pp. 375–405, 2002.

[35] D. Alexander, C. Pierpaoli, P. Basser, and J. Gee, "Spatial transformations of diffusion tensor magnetic resonance images," *IEEE Trans. Med. Imaging*, vol. 20, no. 11, pp. 1131–1139, Nov. 2001.

[36] P. Fletcher and S. Joshi, "Riemannian geometry for the statistical analysis of diffusion tensor data," *Signal Process.*, vol. 87(2), pp. 250–262, 2007.

[37] X. Pennec, P. Fillard, and N. Ayache, "A Riemannian framework for tensor computing," *Int. J. Comput. Vis.*, vol. 66(1), pp. 41–66, Jan. 2006.

[38] V. Arsigny, O. Commowick, X. Pennec, and N. Ayache, "A log-Euclidean framework for statistics on diffeomorphisms," in *Medical Image Computing and Computer Assisted Intervention–MICCAI.* Springer, 2006, pp. 924–931.

[39] S. Mori, K. Oishi, H. Jiang, L. Jiang, X. Li, K. Akhter, K. Hua, A. Faria, A. Mahmood, R. Woods, A. Toga, G. Pike, P. Neto, A. Evans, J. Zhang, H. Huang, M. Miller, P. van Zijl, and J. Mazziotta, "Stereotaxic white matter atlas based on diffusion tensor imaging in an ICBM template," *NeuroImage*, vol. 40, pp. 570–582, Apr. 2008.

[40] N. Sadeghi, M. Prastawa, P. T. Fletcher, J. Wolff, J. H. Gilmore, and G. Gerig, "Regional characterization of longitudinal DT-MRI to study white matter maturation of the early developing brain," *NeuroImage*, vol. 68, pp. 236–247, 2013.

[41] D. Gallichan, J. Scholz, A. Bartsch, T. E. Behrens, M. D. Robson, and K. L. Miller, "Addressing a systematic vibration artifact in diffusion-weighted MRI," *Hum. Brain Mapp.*, vol. 31, no. 2, pp. 193–202, 2010.

[42] J. G. Sled, A. P. Zijdenbos, and A. C. Evans, "A nonparametric method for automatic correction of intensity nonuniformity in MRI data," *IEEE T. Med. Imaging*, vol. 17, no. 1, pp. 87–97, 1998.

[43] H. C. Hazlett, M. Poe, G. Gerig, R. G. Smith, J. Provenzale, A. Ross, J. Gilmore, and J. Piven, "Magnetic resonance imaging and head circumference study of brain size in autism: Birth through age 2 years," *Arch. Gen. Psychiat.*, vol. 62, no. 12, p. 1366, 2005.

[44] Y. Benjamini and Y. Hochberg, "Controlling the false discovery rate: A practical and powerful approach to multiple testing," *J. Roy. Stat. Soc. B*, pp. 289–300, 1995.

[45] D. Yekutieli and Y. Benjamini, "Resampling-based false discovery rate controlling multiple test procedures for correlated test statistics," *J. Stat. Plan. Infer.*, vol. 82, no. 1, pp. 171–196, 1999.

[46] D. Ben Bashat, V. Kronfeld-Duenias, D. A. Zachor, P. M. Ekstein, T. Hendler, R. Tarrasch, A. Even, Y. Levy, and L. Ben Sira, "Accelerated maturation of white matter in young children with autism: A high b value dwi study," *NeuroImage*, vol. 37, no. 1, pp. 40–47, 2007.

[47] K. S. Kendler, "Twin studies of psychiatric illness: An update," *Arch. Gen. Psychiatry*, vol. 58, no. 11, pp. 1005–1014, Nov. 2001.

[48] R. K. Lenroot and J. N. Giedd, "The changing impact of genes and environment on brain development during childhood and adolescence: Initial findings from a neuroimaging study of pediatric twins," *Dev. Psychopathol.*, vol. 20, no. 4, pp. 1161–1175, 2008.

[49] R. C. Knickmeyer, C. Kang, S. Woolson, J. K. Smith, R. M. Hamer, W. Lin, G. Gerig, M. Styner, and J. H. Gilmore, "Twin-singleton differences in neonatal brain structure," *Twin Res. Hum. Genet.*, vol. 14, no. 3, pp. 268–276, June 2011.

[50] H. E. Hulshoff Pol, D. Posthuma, W. F. Baare, E. J. De Geus, H. G. Schnack, N. E. van Haren, C. J. van Oel, R. S. Kahn, and D. I. Boomsma, "Twin-singleton differences in brain structure using structural equation modelling," *Brain*, vol. 125, no. 2, pp. 384–390, Feb. 2002.

[51] D. A. Hay and P. J. O'Brien, "The La Trobe Twin Study: A genetic approach to the structure and development of cognition in twin children," *Child Dev.*, vol. 54, no. 2, pp. 317–330, Apr. 1983.

[52] M. Nathan and R. Guttman, "Similarities in test scores and profiles of kibbutz twins and singletons," *Acta Genet. Med. Gemellol. (Roma)*, vol. 33, no. 2, pp. 213–218, 1984.

[53] D. Posthuma, E. J. De Geus, N. Bleichrodt, and D. I. Boomsma, "Twin-singleton differences in intelligence?" *Twin Res.*, vol. 3, no. 2, pp. 83–87, June 2000.

[54] R. Salvador, A. Pena, D. Menon, T. Carpenter, J. Pickard, and E. Bullmore, "Formal characterization and extension of the linearized diffusion tensor model," *Hum. Brain Mapp.*, vol. 24, no. 2, pp. 144–155, Feb. 2005.

[55] S. M. Smith, "Fast robust automated brain extraction," *Hum. Brain Mapp.*, vol. 17, no. 3, pp. 143–155, Nov. 2002.

[56] X. Geng, S. Gouttard, A. Sharma, H. Gu, M. Styner, W. Lin, G. Gerig, and J. H. Gilmore, "Quantitative tract-based white matter development from birth to age 2 years," *NeuroImage*, vol. 61, pp. 542–557, Jul. 2012.

[57] L. Hermoye, C. Saint-Martin, G. Cosnard, S. K. Lee, J. Kim, M. C. Nassogne, R. Menten, P. Clapuyt, P. K. Donohue, K. Hua, S. Wakana, H. Jiang, P. C. van Zijl, and S. Mori, "Pediatric diffusion tensor imaging: Normal database and observation of the white matter maturation in early childhood," *NeuroImage*, vol. 29, no. 2, pp. 493–504, Jan. 2006.

[58] A. Serag, P. Aljabar, S. Counsell, J. Boardman, J. V. Hajnal, and D. Rueckert, "Tracking developmental changes in subcortical structures of the preterm brain using multi-modal MRI," in *IEEE Int. Symp. Biomed. Imag. (ISBI): From Nano to Macro*, 2011, pp. 349–352.

[59] R. S. Desikan, F. Ségonne, B. Fischl, B. T. Quinn, B. C. Dickerson, D. Blacker, R. L. Buckner, A. M. Dale, R. P. Maguire, B. T. Hyman *et al.*, "An automated labeling system for subdividing the human cerebral cortex on MRI scans into gyral based regions of interest," *NeuroImage*, vol. 31, no. 3, pp. 968–980, 2006.

[60] M. Prastawa, J. H. Gilmore, W. Lin, and G. Gerig, "Automatic segmentation of MR images of the developing newborn brain," *Med. Image Anal.*, vol. 9, no. 5, pp. 457–466, 2005.

[61] B. A. Brody, H. C. Kinney, A. S. Kloman, and F. H. Gilles, "Sequence of central nervous system myelination in human infancy. I. An autopsy study of myelination," *J. Neuropathol. Exp. Neurol.*, vol. 46, no. 3, pp. 283–301, May 1987.

[62] C. R. Henderson, "Selection index and expected genetic advance," *Statistical Genetics and Plant Breeding*, vol. 982, pp. 141–163, 1963.

[63] E. F. Vonesh and V. M. Chinchilli, *Linear and Nonlinear Models for the Analysis of Repeated Measurements*. New York: Marcel Dekker, Inc., 1997.

[64] J. Dubois, G. Dehaene-Lambertz, M. Perrin, J. Mangin, Y. Cointepas, E. Duchesnay, D. Le Bihan, and L. Hertz-Pannier, "Asynchrony of the early maturation of white matter bundles in healthy infants: Quantitative landmarks revealed noninvasively by diffusion tensor imaging," *Hum. Brain Mapp.*, vol. 29, pp. 14–27, Jan. 2008.

[65] H. Kinney, B. Brody, A. Kloman, and F. Gilles, "Sequence of central nervous system myelination in human infancy. II. Patterns of myelination in autopsied infants," *J. Neuropathol. Exp. Neurol.*, vol. 47, no. 3, pp. 217–234, May 1988.

[66] A. LaMantia and P. Rakic, "Axon overproduction and elimination in the corpus callosum of the developing rhesus monkey," *J. Neurosci.*, vol. 10, no. 7, pp. 2156–2175, Jul. 1990.

[67] C. Lebel and C. Beaulieu, "Longitudinal development of human brain wiring continues from childhood into adulthood," *J. Neurosci.*, vol. 31, no. 30, pp. 10 937–10 947, Jul. 2011.

[68] P. Mukherjee, J. Miller, J. Shimony, T. Conturo, B. Lee, C. Almli, and R. McKinstry, "Normal brain maturation during childhood: Developmental trends characterized with diffusion-tensor MR imaging," *Radiology*, vol. 221, no. 2, pp. 349–358, Nov. 2001.

[69] J. F. Schneider, K. A. Il'yasov, J. Hennig, and E. Martin, "Fast quantitative diffusion-tensor imaging of cerebral white matter from the neonatal period to adolescence," *Neuroradiology*, vol. 46, no. 4, pp. 258–266, Apr. 2004.

[70] K. P. Forbes, J. G. Pipe, and C. R. Bird, "Changes in brain water diffusion during the 1st year of life," *Radiology*, vol. 222, no. 2, pp. 405–409, Feb. 2002.

[71] L. Zhang, K. M. Thomas, M. C. Davidson, B. J. Casey, L. A. Heier, and A. M. Uluğ, "MR quantitation of volume and diffusion changes in the developing brain," *AJNR Am. J. Neuroradiol.*, vol. 26, no. 1, pp. 45–49, Jan. 2005.

[72] A. Vardhan, M. Prastawa, A. Sharma, J. Piven, and G. Gerig, "Modeling longitudinal MRI changes in populations using a localized, information-theoretic measure of contrast," in *IEEE Int. Symp. Biomed. Imag. (ISBI): From Nano to Macro*, 2013, pp. 1396–1399.

[73] L. Tierney and J. B. Kadane, "Accurate approximations for posterior moments and marginal densities," *J. Am. Stat. Assoc.*, vol. 81, no. 393, pp. 82–86, 1986.

[74] M. Davidian and A. R. Gallant, "Smooth nonparametric maximum likelihood estimation for population pharmacokinetics, with application to quinidine," *J. Pharmacokinet. Biop.*, vol. 20, no. 5, pp. 529–556, 1992.

[75] J. C. Pinheiro, "Topics in mixed effects models," PhD Dissertation, Dept. Stat., Univ. Wisconsin - Madison, Madison, 1994.

[76] S. Blüml, L. R. Schad, B. Stepanow, and W. J. Lorenz, "Spin-lattice relaxation time measurement by means of a turboflash technique," *Magnet. Reson. Med.*, vol. 30, no. 3, pp. 289–295, 1993.

[77] C. A. McKenzie, Z. Chen, D. J. Drost, and F. S. Prato, "Fast acquisition of quantitative t2 maps," *Magnet. Reson. Med.*, vol. 41, no. 1, pp. 208–212, 1999.

[78] S. C. Deoni, "High-resolution t1 mapping of the brain at 3t with driven equilibrium single pulse observation of t1 with high-speed incorporation of rf field inhomogeneities (despot1-hifi)," *J. Magn. Reson. Im.*, vol. 26, no. 4, pp. 1106–1111, 2007.

[79] C. Beaulieu and P. S. Allen, "Determinants of anisotropic water diffusion in nerves," *Magnet. Reson. Med.*, vol. 31, no. 4, pp. 394–400, 1994.

[80] S. Song, S. Sun, M. Ramsbottom, C. Chang, J. Russell, and A. Cross, "Dysmyelination revealed through MRI as increased radial (but unchanged axial) diffusion of water," *NeuroImage*, vol. 17, no. 3, pp. 1429–1436, Nov. 2002.

[81] D. C. Alexander, "A general framework for experiment design in diffusion MRI and its application in measuring direct tissue-microstructure features," *Magnet. Reson. Med.*, vol. 60, no. 2, pp. 439–448, 2008.

[82] W. Guo, "Functional mixed effects models," *Biometrics*, vol. 58, no. 1, pp. 121–128, 2002.

[83] Z. Liu and W. Guo, "Functional mixed effects models," *Wiley Interdiscip. Rev. Comput. Stat.*, vol. 4, no. 6, pp. 527–534, 2012.

[84] J. O. Ramsay and B. W. Silverman, *Functional Data Analysis*, 2nd ed. New York: Springer, 2006.

[85] C. Goodlett, P. Fletcher, J. Gilmore, and G. Gerig, "Group analysis of DTI fiber tract statistics with application to neurodevelopment," *NeuroImage*, vol. 45, no. 1 (suppl 1), pp. S133–S142, 2009.

[86] A. Sharma, S. Durrleman, J. H. Gilmore, and G. Gerig, "Longitudinal growth modeling of discrete-time functions with application to DTI tract evolution in early neurodevelopment," in *IEEE Int. Symp. Biomed. Imag. (ISBI): From Nano to Macro*, 2012, pp. 1397–1400.

[87] S. Fieuws, G. Verbeke, and G. Molenberghs, "Random-effects models for multivariate repeated measures," *Stat. Methods Med. Res.*, vol. 16, no. 5, pp. 387–397, 2007.

[88] P. M. Thompson, T. D. Cannon, K. L. Narr, T. Van Erp, V.-P. Poutanen, M. Huttunen, J. Lönnqvist, C.-G. Standertskjöld-Nordenstam, J. Kaprio, M. Khaledy, D. Rajneesh, C. I. Zoumalan, and A. Toga, "Genetic influences on brain structure," *Nature Neuroscience*, vol. 4, no. 12, pp. 1253–1258, 2001.